Exploring the Near Field Coupling and Ultrafast Switching in Terahertz Metamaterials

A thesis submitted
in Partial Fulfillment of the Requirements
for the Degree of
DOCTOR OF PHILOSOPHY.

by

S. Jagan Mohan Rao

Department of Physics
Indian Institute of Technology Guwahati
Guwahati 781039, India.

March 2019

Exploring the Near Field Coupling and Ultrafast Switching in Terahertz Metamaterials

A thesis submitted
in Partial Fulfillment of the Requirements
for the Degree of

DOCTOR OF PHILOSOPHY.

by

S. Jagan Mohan Rao
Roll No. 146121032

Supervisors
Dr. Gagan Kumar
Dr. Dibakar Roy Chowdhury

Department of Physics
Indian Institute of Technology Guwahati
Guwahati 781039, India.

March 2019

STATEMENT

The present thesis entitled, " *Exploring the Near Field Coupling and Ultrafast Switching in Terahertz Metamaterials*" has been carried out by me under the supervision of Dr. Gagan Kumar and Dr. Dibakar Roy Chowdhury. This work has not been submitted elsewhere for the award of any degree.

S Jagan Mohan Rao,
Department of Physics, IIT Guwahati,
Guwahati-781039, Assam, India.
DATE: .....

CERTIFICATE

It is certified that the work contained in the thesis entitled " *Exploring the Near Field Coupling and Ultrafast Switching in Terahertz Metamaterials*" by Mr. S. Jagan Mohan Rao, a student of the Department of Physics, IIT Guwahati was carried out under my supervision and has not been submitted elsewhere for award of any degree.

Dr. Gagan Kumar,
Department of Physics, IIT Guwahati,
Guwahati-781039, Assam, India.
DATE: .....

Dr. Dibakar Roy Chowdhury,
School of Engineering Sciences, MEC Hyderabad,
Hyderabad-500043, Telangana, India.
DATE: .....

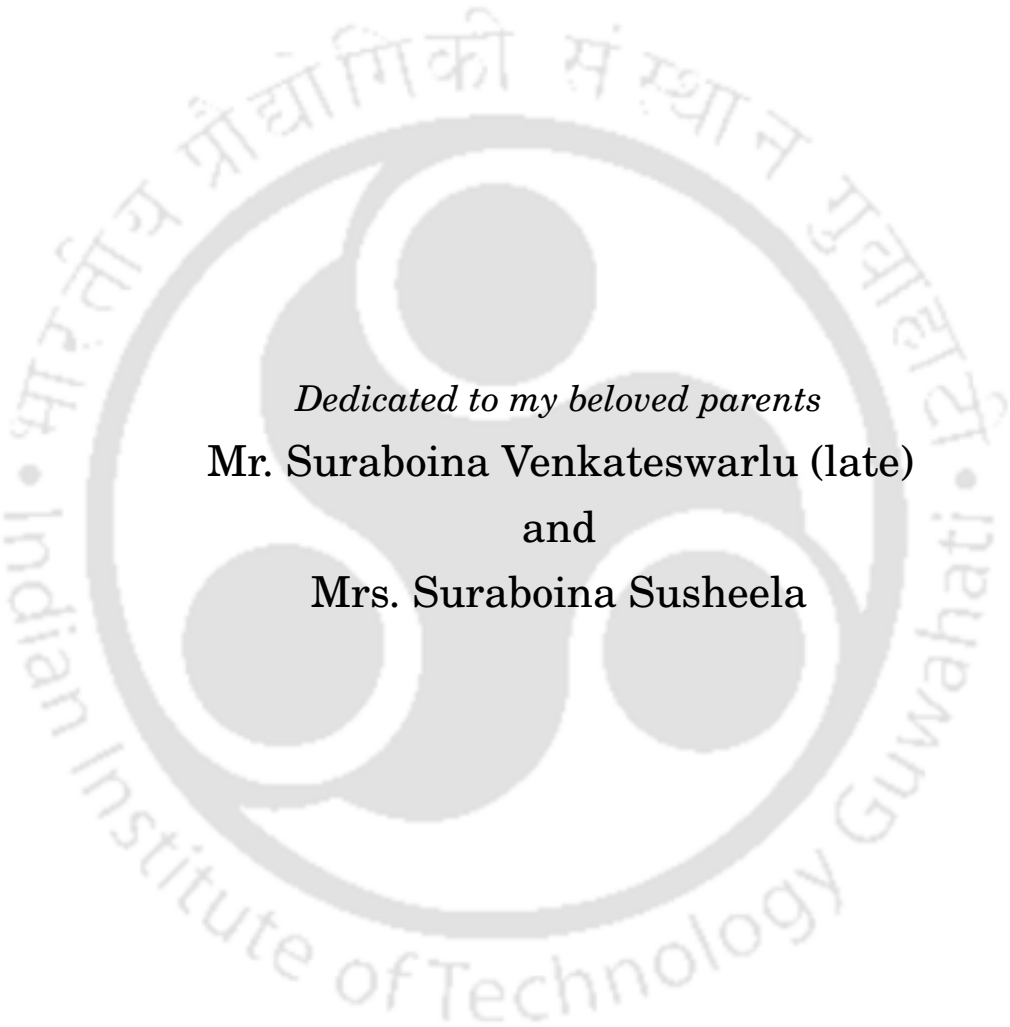

Dedicated to my beloved parents

Mr. Suraboina Venkateswarlu (late)

and

Mrs. Suraboina Susheela

ACKNOWLEDGMENTS

First and foremost, I would like to express my sincere gratitude towards my Ph.D. advisors, Dr. Gagan Kumar, and Dr. Dibakar Roy Chowdhury for letting me conduct my research in the interesting field of terahertz metamaterials. I am grateful to them for their consistent guidance, motivation, patience and kindness over these years. Their enthusiasm and never-say-die attitude towards research and life as well, has always inspired me to work hard.

I would like to thank my doctoral committee members, Dr. Ashwini Kumar Sharma, Dr. Subhash Thota, and Dr. Nitin Chaudhary, for their encouragement and insightful comments which have helped me to understand many things better. My sincere gratitude also goes to the current and the former Heads of the department of Physics, Prof. Subhradip Ghosh, Prof. P. Poulose and Prof. Saurabh Basu, for providing all the resources needed for my research, and also all other faculty members of the department, the technical staff and office members, who provided me help whenever I needed. Without their support it would not have been possible to conduct my research.

I would like to thank Dr. Abul K Azad for his experimental help and I would also like to thank Mr. Yogesh Kumar Srivastava for characterizing my samples. I thank my group-mates Maidul, Monika, Rakesh, Dhriti and Angana for stimulating discussions and for all the fun we have had in these years. I would also like to thank all my batch mates, seniors and juniors in the department for their company and help in direct or indirect ways. I would like to thank my friends of IIT Guwahati from the bottom of my heart, especially the 2014 batch.

The financial support provided through a research fellowship by the Ministry of Human Resource and Development (MHRD) of India is gratefully acknowledged.

My special gratitude goes to my family for their role in my life. My mother Susheela and sisters Bhadramma and Nagamani have always been an inspiration to me. Their unconditional love, support and trust on me are the most precious gifts that I have. My

late father, Mr. Suraboina Venkateswarlu was the most influencing person in my life. I have always felt the blessings of my father from the unseen world. I remember and thank Prasad bavagaru (late). I remember and thank Chennaiah Mavayya. I remember and thank my brother in-law Mr. Narasimharao and nephews Mr. Lokesh and Mr. Venkatesh, for their tremendous love, affection, moral support and help.

I would like to thank my school teachers for drawing my interest towards pursuing science as a career. I thank all the people who have been in direct or indirect association with me for my research work and have helped me in even the slightest possible manner.

ABSTRACT

During the last two decades terahertz (THz) metamaterials have emerged as one of the most fascinating areas in photonics research because of their significance in developing devices for THz gap. In this thesis work, the focus has been made in investigating the potential of planar two dimensional metamaterial structures which can be helpful in the design and construction of THz devices, such as switches, modulators, frequency tunable devices, antennas, etc. Near field resonator coupling along with ultrafast resonance switching in THz metamaterials are studied experimentally, numerically and theoretically, depending upon the research problem. Generally, at THz frequencies, sub-wavelength scale split ring resonator (SRR) is used as the unit cell to build metamaterial geometry. At the resonance frequency of metamaterials, a strong localization of electromagnetic energy takes place inside the gap of the resonator. This localization of electromagnetic energy significantly enhances the localized energy amplitude, which could be utilized for metamaterial to serve as a versatile platform for sensing related applications. Furthermore, circular currents can be induced in split ring resonators giving rise to inductive properties of the SRRs. The combination of capacitive and inductive nature of the SRRs lead to strong inductive capacitive resonance. When two such resonators are brought sufficiently close to each other, they can couple through magnetic and electric field lines giving rise to many interesting phenomena including mode hybridization effect, broadband modulation, terahertz wave modulation, etc. If two SRRs in a unit cell of metamaterial couples through the magnetic induction, in such system near field inductive coupling dominates. When two SRRs in a unit cell of metamaterial couples through the split gaps of SRRs, then near field capacitive coupling dominates.

In this thesis work, we have demonstrated a planar edge coupled metamaterial structure to study the near field inductive coupling in THz metamaterials. In this work, we report the tuning of electromagnetically coupled resonances in planar THz meta-

materials by employing near field interactions via shifting the position of a resonator with respect to the other within the unit cell of metamaterial. In addition, to study the near field inductive coupling in bilayer THz metamaterials, we also demonstrated a broadside coupled THz metamaterial structure. This structure contains two orthogonally placed SRRs separated by a thin micron-scale polyimide layer. In this case, we studied the THz transmission by displacing the top resonator w.r.t. the bottom resonator both in the horizontal and vertical directions. The THz transmissions through the proposed configurations result in the resonance mode hybridization effect due to the coupling between two different resonance modes. We have shown that with the increasing displacement between the resonators, coupling reduces and finally two resonances merge into a single resonance. In order to develop further understanding and analyze the numerical observations in our studies, we have modeled metamaterial structures with a RLC circuit approach.

In addition, to improve the performance of the device in terms of Q-factor, we experimentally studied near field capacitive coupling in planar THz metamaterials. In this study, we designed and fabricated a capacitive coupled planar THz metamaterials. The unit cell of metamaterial comprises of two coupled SRRs with the split gaps facing each other. The coupling between two SRRs is examined by changing the gap of one resonator with respect to the other for various inter resonator separations. The measured THz transmission shows resonance mode hybridization and we calculated Q factor for both the resonance modes. Lower order resonance modes showed higher Q factor than the higher order resonance modes.

Further, to make active devices for THz gap, we demonstrated ultrafast switching in terahertz metamaterials by taking single SRR as a unit cell in a metamaterial and keeping the radiation damaged silicon island at the SRR gaps. Before optical excitation, because of dielectric nature of the SRR gap, transmission through sample gives rise to strong fundamental LC resonance. After optical excitation, the SRR gap loses dielectric nature and starts to conduct because of the excitation of electron hole pairs. The change of fundamental resonance from ON-to-OFF state is observed on a time scale of 4 picoseconds and then fast retrieval of the fundamental resonance to the ON-state within next 20 ps. In order to understand the relaxation process of carriers in radiation damaged silicon, we have used tri exponential theoretical model. This model reveals the dominance of three lifetimes occurring in the carrier relaxation process.

Journal Publications

1. **S. Jagan Mohan Rao**, Deepak Kumar, Gagan Kumar and Dibakar Roy Chowdhury, "Modulating the Near Field Coupling through Resonator Displacement in Planar Terahertz Metamaterials." **Journal of Infrared, Millimeter, and Terahertz Waves**, January 2017, Volume 38, Issue 1, pp 124–134. (DOI: 10.1007/s10762-016-0324-3).

2. **S. Jagan Mohan Rao**, Deepak Kumar, Gagan Kumar and Dibakar Roy Chowdhury, "Probing the Near-Field Inductive Coupling in Broadside Coupled Terahertz Metamaterials." **IEEE Journal of Selected Topics in Quantum Electronics** (Volume: 23, Issue: 4, July-Aug. 2017). (DOI: 10.1109/JSTQE.2016.2635020).

3. **S. Jagan Mohan Rao**, Yogesh Kumar Srivastava, Gagan Kumar and Dibakar Roy Chowdhury, "Modulating fundamental resonance modes in capacitive coupled asymmetric split gap ring resonator based Terahertz Metamaterials" **Scientific Reports** volume 8, Article number: 16773 (2018). (DOI: 10.1038/s41598-018-34942-2).

4. **S. Jagan Mohan Rao**, Gagan Kumar, Abul K. Azad, and Dibakar Roy Chowdhury, "Ultrafast Relaxation of Charge Carriers Induced Switching in Terahertz Metamaterials" **Journal of Infrared, Millimeter, and Terahertz Waves** ,December 2018, Volume 39, Issue 12, pp 1211–1220. (DOI: 10.1007/s10762-018-0547-6).

5. **S. Jagan Mohan Rao**, R Sarkar, Gagan Kumar, and Dibakar Roy Chowdhury, "Gradual Cross Polarization Conversion of Transmitted Waves in Near Field Coupled Planar Terahertz Metamaterials" **OSA Continuum** vol. 2, Issue 3, pp. 603-614 (2019). (DOI: 10.1364/OSAC.2.000603).

6. Maidul Islam, **S. Jagan Mohan Rao**, Gagan Kumar, B. P. Pal and Dibakar Roy Chowdhury "Role of Resonance modes on Terahertz Metamaterials based thin film sensors" **Scientific reports** 7 (1), 7355 (2017)(DOI:10.1038/s41598-017-07720-9).

7. Prashant K Sarswat, Nipon Deka, **S. Jagan Mohan Rao**, Michael L Free, Gagan Kumar, "Surface Texture-Induced Enhancement of Optical and Photoelectrochemical Activity of Cu_2ZnSnS_4 Photocathodes." **Journal of Electronic Materials**, pp 1–11. (2017). (DOI: 10.1007/s11664-017-5531-8).

Conference Publications

1. **S. Jagan Mohan Rao**, Maidul Islam, Gagan Kumar, B. P. Pal and Dibakar Roy Chowdhury, "Single split gap resonator based terahertz metamaterials for refractive index sensing" Proceedings Volume 10531, Terahertz, RF, Millimeter, and Submillimeter-Wave Technology and Applications XI; 105311K (2018) **https://doi.org/10.1117/12.2287320. Event: SPIE OPTO, 2018, San Francisco, California, United States.**

2. **S. Jagan Mohan Rao**, Rakesh Sarkar, D Khandelwal, G Kumar, D Roy Chowdhury, "Studying the near field capacitive coupling in planar terahertz metamaterial" 2017 **IEEE Workshop on Recent Advances in Photonics (WRAP), 1-3. DOI: 10.1109/WRAP.2017.8468590.**

3. Deepak Kumar, **S. Jagan Mohan Rao**, Gagan Kumar, Dibakar Roy Chowdhury," Near Field Coupling in THz Metamaterials." International Conference on Fiber Optics and **Photonics 2016, OSA, doi.org/10.1364/PHOTONICS.2016.W4A.1.**

List of Figures

- **Figure 2.4:** (a) Schematic of the terahertz time domain spectroscopy setup. Photoconductive antennas are used as the terahertz source and detector. (b) & (c) A schematic of the photoconductive antenna comprising two transmission lines with two poles separated by a distance 'g'. The LT-GaAs is used as the substrate for fabricating antenna.

- **Figure 2.5:** Time domain signal converted to frequency domain by using Fourier transformation. (a) Transmission signal in time domain. (b). Transmission in frequency domain.

- **Figure 2.6:** Schematic of the optical pump terahertz probe technique (OPTP) setup. Photoconductive antennas are used as the terahertz source and detector.

- **Figure 2.7:** Schematic of split ring resonator and equalnet RLC circuit. (a) Split ring resonator, yellow region represents metallic area and blue region represents substrate. (b) Equivalent RLC circuit.

- **Figure 2.8:** Schematic of coupled SRRs (unit cell) and corresponding RLC circuit. (a) Two coupled SRRs, yellow region represents metallic area and blue region represents substrate.(b) Equivalent RLC circuit for coupled SRRs.

- **Figure 3.1:** (a) Numerically calculated terahertz transmission through a metamaterial geometry having single SRR as a unit cell. (b) Schematic of 2D metamaterial having single resonator as a unit cell.

- **Figure 3.2:** (a) Numerically calculated terahertz transmission through a metamaterial geometry having two coupled SRRs as a unit cell. (b) Schematic of 2D metamaterial having two coupled SRRs as a unit cell.

- **Figure 3.3:** Schematic of a unit cell comprising of two SRRs in a coupled THz metamaterials. The gray regions indicate substrate while the yellow regions represent metallic areas. Each of the SRRs has an outer dimension of 40 μm $\times$40 μm and gap of 2 μm as depicted in the schematic. Δx represents a shift in the position of second resonator with respect to the first in x- direction. The figures (a), (c) and (e) depicts a shift of Δx = 0, 50,100% , when split gap is on the left hand side, while (d), (e) and (f) represents the same shift with gap on right side.

- **Figure 3.4:** Numerically calculated terahertz transmission through a coupled metamaterial geometry. A THz transmission through a coupled MM sample when split gap is on the left side and close to the first resonator. Various curves correspond to different displacements of the second resonator with respect to the first i.e. Δx = 0, 25, 50, 75,100%. The results of THz transmission for various positions of the second resonator with split gap on the right side are shown in (b).

- **Figure 3.5:** Variation of THz frequency with displacement, Δx in the position of 2nd resonator. (a) The change in frequencies of first and second resonances are plotted with displacements, with split gap of the 2nd resonator facing left side close

to first resonator. (b) Plot indicates the variation of frequencies with displacements for the same parameters as in (a) however split gap position of the Meta resonator is facing right side in this case.

- **Figure 3.6:** Simulated surface current distributions at different resonant frequencies of the coupled resonator when split gap of the 2nd resonator is facing on the left side. The red curves indicate the trend of surface currents through resonators. Figures (a), (c) and (e) correspond to the displacements, Δx = 0, 50, 100% respectively and depicts current distributions for the first resonances in each case. The current distributions for the 2nd resonances (or higher order split resonances) are shown in figures (b) and (d) corresponding to the displacements of Δx = 0, 50%. For Δx = 100 %, the coupling is negligibly small.

- **Figure 3.7:** Simulated surface current distributions at different resonant frequencies when split gap of 2nd resonator is facing on the right side. Figures (a), (c) and (e) correspond to the displacements of Δx = 0, 50,100% respectively and depicts current distributions for the first resonances. The current distributions for the 2nd resonances corresponding to the displacements of Δx = 0, 50% are shown in figures (b) and (d).The trends of the currents are shown through red curves.

- **Figure 3.8:** Schematic of the transmission-line, RLC (TL-RLC) circuit model. Components R_1,L_1,C_1 represent the resistance, inductance and capacitance describing the LC resonance of the first resonator and R_2, L_2, C_2 describe the 2nd resonator. The parameter M represents the coupling between the resonators. The intrinsic impendences of the transmission lines are depicted by Z_0 and Z_g.

- **Figure 3.9:** Terahertz transmission through the coupled resonators obtained using transmission line RLC circuit model. The results are obtained for various displacements of 2nd resonator w.r.t. 1st resonator. The results predict numerical observations. Figure (a) corresponds to the situation when 2nd resonator of the unit cell is facing left side while in (b) it is on the right side.

- **Figure 4.1:** Schematic of a single unit cell consisting of two SRRs in the broadside coupled bilayer THz metamaterial. The yellow regions represent the metallic gold areas which are separated by a polyimide spacer shown by the transparent green color. Δx and Δy represent the displacements in x and y directions, respectively. The dotted SRR in figures b and c indicates the initial position of the resonator. Each of resonators has outer dimensions of l × l = 48 μm × 48 μm. The w and g in the schematic stand for the width and split gap of the resonators respectively. (a) Shows the bilayer metamaterials configuration without any displacement between the resonators. (b) The displacement of the top resonator in the horizontal direction w.r.t. to the bottom resonator while maintaining Δy = 0. The red arrow indicates the direction of displacement. (c) Vertically displaced top resonator w.r.t. the bottom resonator i.e. Δy is finite while Δx = 0. (d) Side view of the bilayer metamaterial with spacer thickness 'd' = 4 μm when top and bottom resonators are aligned. (e) Schematic of broadside coupled terahertz metamaterial.

- **Figure 4.2:** (a) Numerically calculated terahertz transmission through a metamaterial geometry having only bottom SRR as a unit cell. (b) Numerically calculated THz amplitude transmission through a metamaterial geometry having only top SRR as a unit cell.

- **Figure 4.3:** Numerically calculated terahertz transmission through the coupled metamolecule as studied in this work. (a) Terahertz transmission for various horizontal displacements i.e. Δx = 0, 25, 50, 75, 100% of the top resonator w.r.t. the bottom resonator. The results of the terahertz transmission for different vertical displacements i.e. Δy = 0, 25, 50, 75, 100% are shown in figure (b). The inset in both the plots represents a SRR unit cell along with the direction of displacements of the resonators.

- **Figure 4.4:** Variation of THz frequency corresponding to the first and second resonances exhibited by the bilayer metamaterial sample versus displacement between the resonators. (a) Shows the variation of first resonance (solid black traces) and second resonance (solid red traces) when the top resonator is horizontally displaced w.r.t. the bottom resonator. The variation of 1st and 2nd resonances w.r.t. the vertical displacement (Δy) is shown in Fig. 3 (b). The traces in violet and blue dots represent intrinsic resonances of the two uncoupled resonators i.e. SRR (top) and SRR (bottom), respectively.

- **Figure 4.5:** Simulated surface current distributions for different displacements between the resonators. (a) and (b) show current distributions for the 1st and 2nd resonances when Δx = Δy = 0%. (c) and (d) represent current distribution for Δx = 100%and Δy = 100% respectively at the 1st resonance frequency. The red arrows indicate the direction of currents in the resonators.

- **Figure 4.6:** Schematic of the transmission line RLC circuit model. The electrical components R_1,L_1,C_1 represent the resistance, inductance, capacitance describing the fundamental LC resonance of the top meta-resonator and R_2, L_2, C_2 describe the resonance for the second bottom resonator. Z_1 and Z_2 represent the LC impedance and second order resonance impedance respectively. The characteristic impedances of transmission lines are represented by Z_0 and Z_s. The parameter M is responsible for the coupling between the resonators.

- **Figure 4.7:** Terahertz transmission through the coupled resonators in bilayer THz metamaterials obtained from transmission line RLC circuit model for various displacements of top split ring resonator w.r.t. bottom SRR. The results affirm numerical observations. (a) Terahertz transmission for various displacements of the top resonator in the horizontal direction. For vertical shift of the top resonator w.r.t. the bottom, the transmission results are shown in (b).

- **Figure 5.1:** Schematic of a unit cell comprising of two SRRs in a coupled THz metamaterials. The blue regions indicate substrate while the yellow regions represent metallic areas. Each of the SRRs has an outer dimension of 36 μm × 36 μm and

gap (g_1) of bottom SRR is 2 μm, gap of top SRR is g2 (g2 = 2, 6, 10. . . .28 μm), width (w) of SRR is 4 μm. 'S' represents a separation between two SRRs in y-direction (S = 2, 6, 10 and 14 μm). (b) Optical microscope image of fabricated sample.

- **Figure 5.2:** Simulation results for single SRR as unit cell in THz MMs. (b) Simulation results for two symmetric coupled SRR as unit cell in THz MMs. (c) Schematic for capacitive coupled THz MMs.

- **Figure 5.3:** Experimental and numerically calculated amplitude spectra for 4 different separations. Dotted lines represent the experimental results and the thick line represents numerical simulation results.

- **Figure 5.4:** Contour plot of numerically simulated THz transmittance for four different separation between two SRRs. Color bar shows the magnitude of transmission intensity. (a) Represents contour plot for separation between two SRRs i.e. S = 2 μm case. (b), (c) and (d) represents contour plots for S = 6, 10, 14 μm respectively.

- **Figure 5.5:** (a), (b), (c) and (d) represents Q factor verses top resonator gap plots for S = 2, 6, 10 and 14 μm cases respectively.

- **Figure 5.6:** (a) & (b) Represent the surface current profile of S= 2 μm case for g_1 =2 μm, g_2 = 14 μm at f=0.419 THz and f=0.554 THz. (c) & (d) Represents the electric field profiles of S= 2 μm case for g_1 = 2 μm and g_2 = 14 μm at f=0.419 THz and f= 0.554 THz. In figures (c) and (d), arrows shows the direction of the electric field and the color and size of the arrows indicates field strength. The polarity of the induced electronic charges on the SRR arms is indicated in the figure.

- **Figure 5.7:** (a) & (b) Represent the surface current profile of S= 14 μm case for g_1 = 2 μm, g_2 = 14 μm at f=0.461 THz and f=0.534 THz. (c) & (d) Represents the electric field profiles of S= 14 μm case for g_1 = 2 μm and g_1 = 14 μm at f=0.461 THz and f= 0.534 THz. In figures (c) and (d), arrows shows the direction of the electric field and the color and size of the arrows indicates field strength. The polarity of the induced electronic charges on the SRR arms is indicated in the figure.

- **Figure 6.1:** (a) Schematic of the SRR array depicting the MM sample studied in this work. (b) Unit cell of MM sample. The geometrical dimensions of the SRR are indicated inside the figure. In the image, P_x and P_y are periodicities in the x and y directions, respectively and silicon is placed inside the split gap.

- **Figure 6.2:** (a) Transient change in the terahertz transmission peak due to the optical pump induced conductivity in RD-SOS. (b) Transmitted E-field amplitude through the metamaterial sample at various pump-probe delays. The incident electric field polarization was carefully aligned along the gap-bearing arm of the SRR.

- **Figure 6.3:** (a) Numerical simulations of electric field amplitudes transmitted through the MM sample for different silicon conductivities in the split gap. (b) Optical image of the unit cell of the fabricated MM sample.
- **Figure 6.4:** Simulated induced electric field at fundamental resonance frequency (1.08 THz) for different conductivities of silicon in the split gap resembling the situations with different pump-probe time delay. In all the sub-figures, the same scale is employed to represent the induced electric field strength.
- **Figure 6.5:** (a) Carrier lifetime dynamics of radiation-damaged silicon plots - theoretical and experimental. (b) Charge carriers can relax via three process: into the ion trap states (τ_1, τ_2) or radiative recombination from conduction band to valence band (τ_3).

LIST OF TABLES

TABLE OF CONTENTS

CHAPTER 1

INTRODUCTION

Terahertz (THz) radiations are electromagnetic radiations with frequencies ranging from 0.1 THz to 10 THz (3 mm - 30 μm). This region occupies a large portion of the electromagnetic spectrum between infrared and microwave frequency band (see Fig. 1.1). The radiation of 1 THz has a period of 1 ps, a wavelength of 300 μm, a wave number of 33 cm^{-1} and a photon energy of 4.1 meV [1–4]. THz radiations are also termed as T rays and their properties and behavior are governed by the Maxwell equations, just like other electromagnetic waves. Nowadays, terahertz science and technology has been gaining rapid growth because of its great significance in applications such as imaging, sensing, communications and many other areas. The technological developments in the areas of sensing, imaging and communication in terahertz band remained unexplored over the years compared to the relatively well-developed microwave and optical frequency regions. This is the reason, this band of frequencies has been termed as THz gap too. One of the biggest reasons for underdevelopment of this region has been the unavailability of the efficient methods for the generation and detection of terahertz frequencies and lack of devices in THz region. In the late 1980s, the use of photo-conductive antennas generated the first prototype of a pulsed THz wave emitter and detector. Since then several articles have been published on efficient terahertz generation and detection [5–7]. Various techniques for the generation of high power terahertz radiations with broad frequency bandwidth have also been devised. This include photo-carrier acceleration in PC antennas, second order nonlinear effects in electro-optic crystals, plasma oscillations

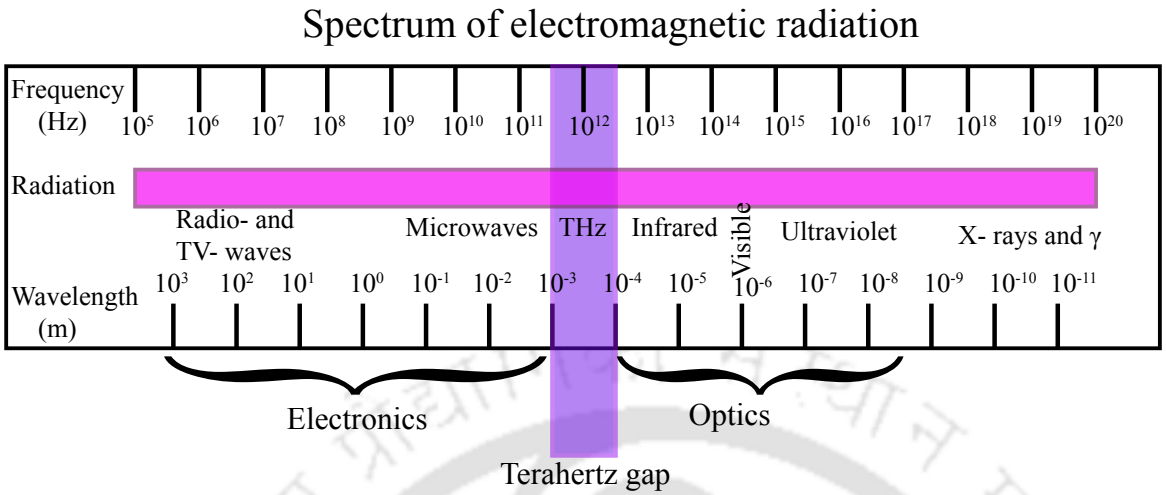

Figure 1.1: Schematic of the THz region in the electromagnetic spectrum. The light color represents the terahertz gap.

and electronic non-linear transmission lines. Photo-conduction and optical rectification are the two most common approaches for generating broadband THz beams. The actual conversion efficiency for these techniques is still not that high and average THz power is in the nW (Nano watt) or μW (micro-watt) range [8–11].

However, terahertz power generated from these two methods can be used to examine several terahertz related phenomenon and applications [1, 12–16]. With the advancements of ultrafast laser pulses and development of various sources and detectors for terahertz radiations, the significance of these radiations has increased [17]. Terahertz radiations can lead to unprecedented sensing applications [18] in many areas including biology, pharmacy, medical science, industrial non-destructive evaluation, material science, environment monitoring, security and astronomy. There are numerous examples of terahertz sensing in different fields such as in DNA chips, skin-cancer diagnosis [19], large scale integrated (LSI) circuit testing, explosives inspection etc. [2, 20]. One of the great advantage with THz waves is that they exhibit low photon energies and thus can't lead to the photo-ionization in biological tissues contrary to the X-rays. As a result, THz waves are considered safe for both the samples and the operator. Therefore, they have the potential to supplement X-rays in imaging applications. Due to extreme water absorption, THz waves can't penetrate into the human body like microwaves do [21]. Therefore, THz waves are considered very promising in nondestructive evaluation applications. The wavelength of the THz waves is sufficiently short to provide sub-millimeter level spatial resolution. If near field techniques are used, higher spatial resolution down to *nm*

could be achieved. At THz frequencies, many molecules exhibit strong absorption and dispersion due to rotational and vibrational transitions. These transitions are specific to the molecule and therefore enable spectroscopic finger-printing in the THz range [22, 23]. Combined with imaging technology, inspection using THz waves provides both profile and composition information of the target. Further, THz waves are transparent to most of the dielectric materials, such as cloth, paper, wood and plastic. Therefore, these waves can be significant in screening passengers at airports and prevention of criminal offences.

THz spectroscopy has the ability to characterize the electronic, vibrational and compositional properties of solids, liquids and gases. Many biological and chemical compounds have distinct signature responses to THz waves due to their unique molecular vibrational and rotational energy levels, implying that their chemical composition can be examined using THz beam. With the use of THz, it is also possible that plastic explosives could be distinguished from suitcase [24]. Furthermore, detecting the binding state of genetic materials (DNA and RNA) [19] by directly using THz waves, without requiring markers, allows for a label free method for genetic analysis for future biochip technologies. There are many new technologies which have been developed in this fast growing area of science and technology. Just like other spectroscopy techniques, we use a special tool called THz time-domain spectrometer (THz-TDS) for characterizing samples in the terahertz domain. The THz-TDS spectroscopy can provide ultra-broad bandwidth depending upon the type of emitter and detectors used. It provide both phase and amplitude information and hence significant in extracting both the absorption and dispersion properties. The technique of pulsed terahertz time domain spectroscopy was first invented more than 20 years ago. The details of this setup are discussed in chapter 2. For most of these applications, not only efficient terahertz sources are required but also very high-speed terahertz components and devices to control and manipulate the terahertz waves are needed. The development of terahertz sources, detector and reliable characterization techniques has led the scientists and engineers to focus on the development of terahertz devices that can lead to various applications outlined above. Metamaterials, in this context, have emerged as one of the potential candidate for manipulating electromagnetic waves and for the actualization of such devices.

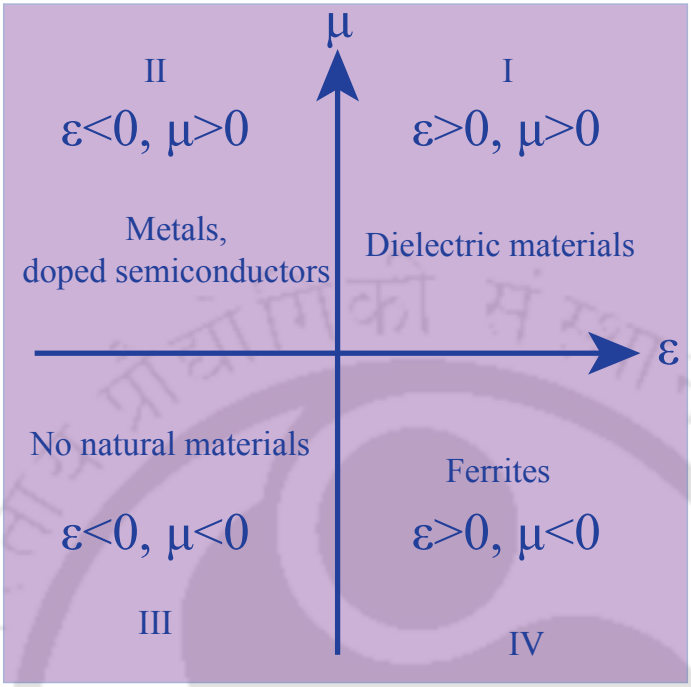

Figure 1.2: Classification of materials based on their effective permittivity and effective permeability.

1.1 Metamaterials

Metamaterial (MM) is a periodical arrangement of artificial structural elements (metamolecules) designed to achieve unusual electromagnetic (EM) properties [25–29]. Generally, split ring resonators (SRRs) are the basic building blocks of the metamaterials [30]. The optical and physical properties of the metamaterials can be controlled by changing the shape, orientation, size or geometry of the SRRs. In metamaterials, the unit cell dimensions are much smaller than the wavelength of incident radiation. For metamaterials, usually $p < \lambda_g/4$, where p is the structural average cell size and λ_g is the guided wavelength. Since p is smaller than wavelength, effective media properties beyond those available in nature can be achieved. The electromagnetic properties of any material are determined by its permeability (μ) and permittivity (ϵ) (Fig. 1.2). Generally all materials are categorized into four quadrants based on their μ and ϵ values. The four possible sign combinations in the pair (μ, ϵ) are (+, +), (+,-), (-,-), and (-, +), as shown in ϵ-μ diagram of Fig. 1.2. In the first quadrant, permittivity and permeability values are

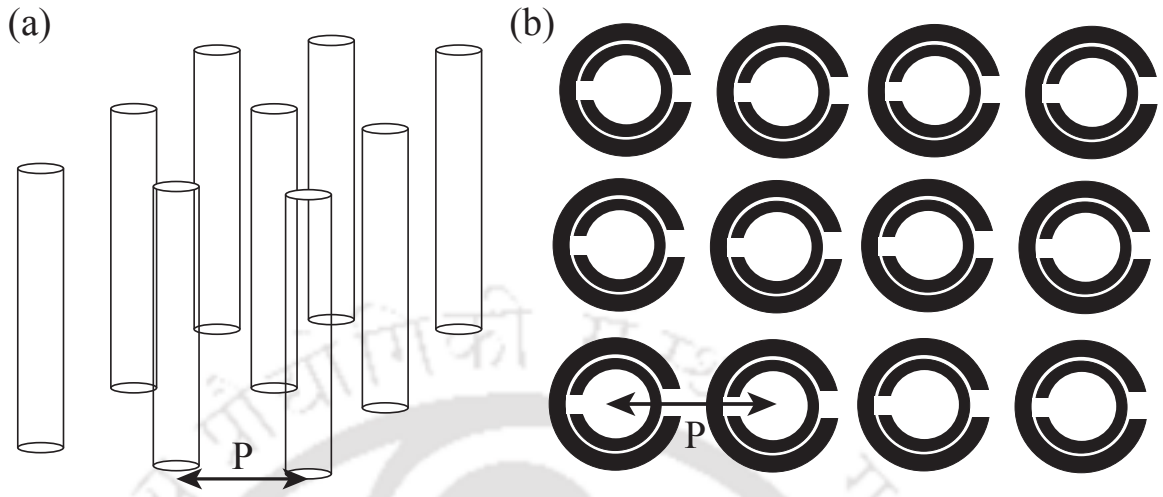

Figure 1.3: P represents periodicity. (a) Square array of metallic cylinders. (b) Plain view of a split ring resonators array. [30]

greater than zero ($\epsilon > 0$ $\mu > 0$), i.e. ϵ and μ both are positive. Most naturally occurring materials (e.g. dielectrics) fall in this quadrant (refractive index (n) is real and show forward wave propagation). In the second quadrant, permittivity value is less than zero ($\epsilon < 0$) and permeability value is greater than zero ($\mu > 0$). Most of the metals and doped semiconductors fall in this category (refractive index (n) is imaginary and show low transmission for thick samples). In third quadrant, permittivity and permeability values are less than zero ($\epsilon < 0$, $\mu < 0$). Some metamaterials or left handed materials fall in this category (refractive index (n) is imaginary and show backward wave propagation. In backward wave propagation, the wave propagation direction is anti-parallel to the Poynting vector. For a common material with positive μ and ϵ, one may deduce from Maxwell's 3rd and 4th equations i.e., $\bar{K} \times \bar{E} = \omega\mu\bar{H}$; $\bar{K} \times \bar{H} = -\omega\epsilon\bar{E}$, that the vectors E, H, and k form a right handed coordinate system and k is parallel to the Poynting vector $\bar{E} \times \bar{H}$, which indicates the direction of energy propagation. However, in a negative index material (NIM), where both μ and ϵ have negative values, the vectors E, H, and k form a left handed system. In such a system the wave vector k is anti-parallel to the Poynting vector). Finally, the last and fourth quadrant has permittivity value greater than zero ($\epsilon > 0$) and permeability value less than zero ($\mu < 0$), ferrite materials fall in this quadrant (refractive index (n) is imaginary and show low transmission for thick samples) [31].

1.1.1 The emergence of metamaterials

In 1968, Veselago predicted in his paper about existence of substances with simultaneously negative values of permittivity and permeability (third quadrant materials, Fig. 1.2). In the same paper, he also investigated different interesting optical properties of the negative refractive index materials. Veselago called these materials as left handed (LH) to show that they would permit the propagation of EM waves with electric filed, magnetic field, and the phase constant vectors follow a left hand rule (wave vector and Poynting vector are in opposite direction), compared to the conventional materials where this rule is known to be right hand (RH) (In the propagation of electromagnetic waves, the direction of energy flow is given by a right-hand rule, involving E, H, and S (S = E×H), where wave vector and Poynting vector are in same direction). In these materials, the phase velocity of an electromagnetic wave propagates in a direction opposite to the direction of flow of energy. These materials show reversal of Doppler Effect and Snell's law etc. [32]. In late 1990s, Pendry and co-workers proposed thin wire structure (Fig. 1.3 (a)) to get negative permittivity (-ϵ) and positive permeability (μ) [30]. The incident EM wave electric field is parallel to the axis of the wires, this field induces a current along the thin wires and produces an electric dipole moments. Plasmonic-type permittivity frequency exhibited by this metamaterial structure is

$$\epsilon_r(\omega) = 1 - \frac{\omega_{pe}^2}{\omega^2 + j\omega\zeta} \tag{1.1}$$

where

$$\omega_{pe} = \sqrt{\frac{2\pi c^2}{p^2 ln(\frac{p}{a})}}$$

$$\zeta = \frac{\epsilon_0(\frac{p\omega_{pe}}{a})^2}{\pi\sigma}$$

where ω_{pe} the tunable electric plasma frequency in the GHz range and ζ is the damping factor due to metal loss (c is the speed of light, a is the radius of the wires and σ is the conductivity of the metal). From the above dispersion relation we can conclude that

Re(ϵ_r) < 0, for $\omega^2 < \omega_{pe}^2$-ζ^2

and if ζ = 0, then ϵ_r < 0 for $\omega < \omega_{pe}$

In this thin wire structure, permeability is simply $\mu = \mu_0$, because no magnetic dipole is generated. In this structure, the thin wires are assumed to be much longer than the incident wavelength. To achieve negative permeability (-μ) and positive permittivity

(ϵ), Pendry introduced metal double split ring resonator structure (Fig. 1.3 (b)). The incident wave magnetic field H is perpendicular to the plane of the rings. This induces circular currents in the ring and generate equivalent magnetic dipole moments. This metamaterial structure exhibits a plasmonic-type permeability frequency as below

$$\mu_r(\omega) = 1 - \frac{F\omega^2}{\omega^2 - \omega_{0m}^2 + j\omega\zeta} \tag{1.2}$$

where

$$F = \pi(\frac{a}{p})^2$$

$$\omega_{0m} = c\sqrt{\frac{3p}{\pi l n(\frac{2wa^3}{\delta})}}$$

Here, F is the filling fraction of the SRR, ζ=$\frac{2PR'}{a\mu_0}$, is the damping factor due to metal loss (R' is the metal resistance per unit length, a is the inner radius of the smaller ring, w is the width of the rings and δ is the radial spacing between the rings). ω_{0m} is a magnetic resonance frequency, tunable in GHz range. The SRR structure was found to have magnetic response due to the presence of artificial magnetic dipole moments by the ring resonator. Eq. (1.2), reveals that a frequency range can exist in which Re (μ_r) < 0 in general . In the loss-less case, it appears that ($\zeta \neq 0$), it follows that

$\mu_r < 0$, for $\omega_{0m} < \omega < \frac{\omega_{0m}}{\sqrt{1-F}} = \omega_{pm}$.

In 2000, Smith and his colleagues experimentally proved the existence of left handed material. Smith *et al*. had inspired from J B Pendry's work and they had proposed and experimentally verified negative refractive index by combing the thin wire structure and circular split ring resonator structure in the microwave region (see Fig. 1.4 (a)) [33]. Subsequently, negative refractive index was also experimentally verified by using square SRRs in the microwave region [34] (see Fig. 1.4 (b)).

1.1.2 Applications of metamaterials

Today, electromagnetic metamaterials involve not only negative-index materials, but also other artificial materials, such as single negative materials (single negative metamaterials have either negative relative permittivity (ϵ_r) or negative relative permeability (μ_r).) [35], chiral metamaterials etc. [36, 37]. Metamaterials exhibit several fascinating features and applications including invisibility cloaking [38], perfect lens [39] to over-

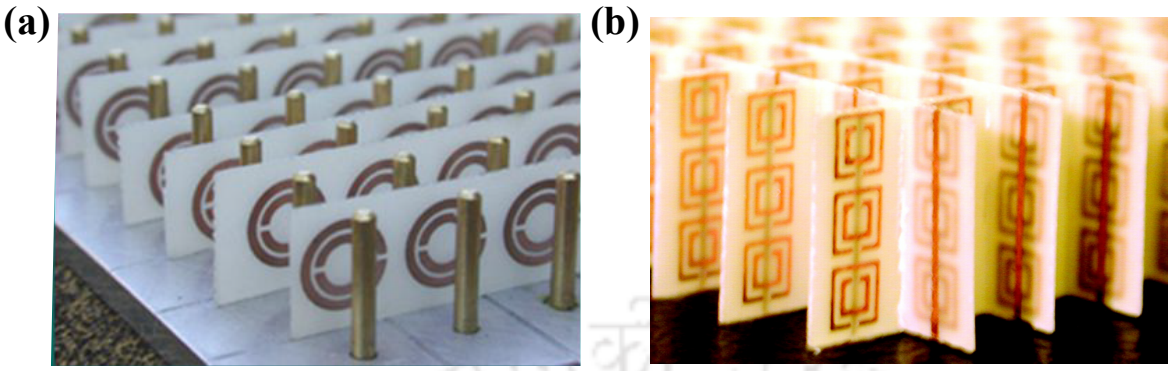

Figure 1.4: First experimental left handed structures to demonstrate negative index of refraction. (a) Metamaterial comprises of circular copper split ring resonators and continuous wires fabricated on a circuit board. [33] (b) Metamaterial comprises of square copper split ring resonators and continuous wires fabricated on a circuit board. [34]

come the diffraction limits, perfect absorbers to absorb the complete radiation, sensors, resonance modulation in the active and passive modes, antennas etc [40–45]. Using normal lenses in microscope, telescope, or camera we can't see images beyond diffraction limit. Image resolution is limited by diffraction limit of optical lenses. Diffraction limit is the ratio of wavelength of light (λ) being used and numerical aperture (NA) of optical lens, i.e. d = $\frac{\lambda}{NA}$. An optical microscope can't differentiate between two objects less than d. Using metamaterial lens also known as super lens, one can overcome the diffraction limit. Because of the Abbe diffraction limit, conventional lenses with curved surfaces based on positive - index materials can't solve objects smaller than about half of the illuminating wavelength, λ_0. The waves scattered by an object have all of the Fourier components in the propagating direction with the wave vector, $k_z = \sqrt{k_0^2 - k_x^2 - k_y^2}$ where k_0 is the free-space wave vector, and each pair of (k_x, k_y) corresponds to a Fourier component of the waves from the object. The total transverse wave vector is $k_t = \sqrt{k_x^2 + k_y^2}$. When k_t is smaller than k_0, k_z is a real number and the wave can propagate in any common material without significant power loss. When the value of k_t exceeds k_0 , k_z becomes an imaginary value and the wave decays exponentially in the propagation direction. Such waves, commonly referred to as "evanescent waves," are confined to the object's vicinity and have no contribution to the standard lens image. However, these evanescent waves carry the characteristics of an object's sub-wavelength, because it is necessary to probe the fine details, the transverse wavelength $\lambda_t = \frac{2\pi}{k_t}$, k_t is lower than the scale of the characteristics, otherwise the wave will overlook the fine details of the object.

Since the maximum possible value of k_t for wave propagation is the same as the free space wave vector k_0, the maximum resolution can be estimated as $\frac{2\pi}{k_{t,max}} = \lambda_t$. Therefore, conventional imaging system cannot provide sub wavelength resolution since they are unable to restore the evanescent waves. Researchers have been able to probe and collect the evanescent waves before they fade away in order to beat the diffraction limit and obtain images with sub-wavelength features. This is precisely the mechanism behind near - field scanning optical microscopy, where a probe is placed in the near - field to collect evanescent waves. There appeared to be no alternative to exploring evanescent modes for many years, except for using a tip or probe very close to a specimen's surface. However, in 2000, Pendry made a groundbreaking prediction, saying that due to its unique property of amplifying evanescent waves, a negative index material (NIM) slab is capable of producing perfect images [39, 46].

On the other hand, a metamaterial absorber can manipulate the loss components of metamaterials permittivity and magnetic permeability, to absorb enhanced amounts of electromagnetic radiation [47]. This is a useful feature for photo detection and solar photo-voltaic applications. Metamaterial antennas are a class of antennas that use metamaterials to improve performance. Few researchers showed that metamaterials could enhance the radiated power of an antenna. Materials that can attain negative permeability allow for properties such as small antenna size, high directivity and tunable frequency. Metamaterial opens a door for designing sensor with specified sensitivity. Particularly planar metamaterials form a unique platform for thin film sensing. Cleverly designed metamaterials can provide tools to significantly enhance the sensitivity and resolution of such sensors. Metamaterial sensors are used in agriculture, biomedical applications etc. [48–50].

1.2 Terahertz metamaterials

Terahertz metamaterial is a class of composite metamaterials intended to interact at the terahertz frequencies [51]. The terahertz frequency range used in materials research is generally defined as 0.1 THz to 10 THz. After the first experimental demonstration of metamaterials in the microwave region, it was soon extended to other regions of electromagnetic spectrum including terahertz regime. There are several potential applications of metamaterials in this terahertz regime, since the desired response from naturally occurring materials is rare. Using metamaterials, efficient terahertz devices

such as switches, modulators, frequency tunable devices etc. can be realized [52–59]. In terahertz regime, the metamaterials are mainly designed using the similar SRR as in case of microwave domain, however with structures on sub-wavelength scale. Firstly, in 2004, the classic SRR was scaled to give a magnetic response in the THz regime [60]. Yen *et al*. showed that magnetic response at terahertz frequencies can be achieved in a planar structure composed of nonmagnetic conductive resonant elements. The magnetic response can be realized over a large bandwidth and tuned throughout the terahertz frequency regime by scaling the dimensions of the structure. Metamaterials yield resonant electromagnetic behavior at a specific frequency depending upon the shape and size of the constituents and their permittivity.

At the resonance frequency of metamaterials, a strong localization of electromagnetic energy takes place inside the resonator which can significantly enhance electric and magnetic fields amplitude. This important feature of MMs can be used to realize many applications in terahertz regime. Additionally, circular currents can be induced in SRRs giving rise to inductive properties of the SRRs. The combination of capacitive and inductive nature of SRRs, can lead to strong inductive capacitive resonance, termed as the LC fundamental resonance [61] ($\omega = 1/\sqrt{LC}$). We have discussed the features of this resonance in length in chapter 2. Artificial magnetic structures, or hybrid structures that combine natural and artificial magnetic materials, can also play a key role in terahertz devices [62, 63]. For several applications, it would be desirable to create metamaterials that exhibit an externally controlled active, dynamical, and tunable response. In this context many researchers have done great works. Chen *et al*. demonstrated an electrically controlled planar hybrid metamaterial device that linearly controls the phase of terahertz radiation with constant insertion loss over a narrow frequency band. They claimed that their device may operate as a broadband terahertz modulator because of the causal relation between the amplitude modulation and phase shifting [64]. In another study, Chen *et al*. presented resonance properties in terahertz metamaterials consisting of a split-ring resonator array made from high-temperature superconducting films. By varying the temperature, they observed efficient metamaterial resonance switching and frequency tuning [65]. Li *et al*. studied a novel coupling scheme of planar terahertz metamaterial to tune the plasmon induced transparency peak by physically varying the distance between the super radiant and the sub radiant resonators. They showed the transparency peak begins to disappear as the coupled resonators are brought closer than a critical separation distance [66].

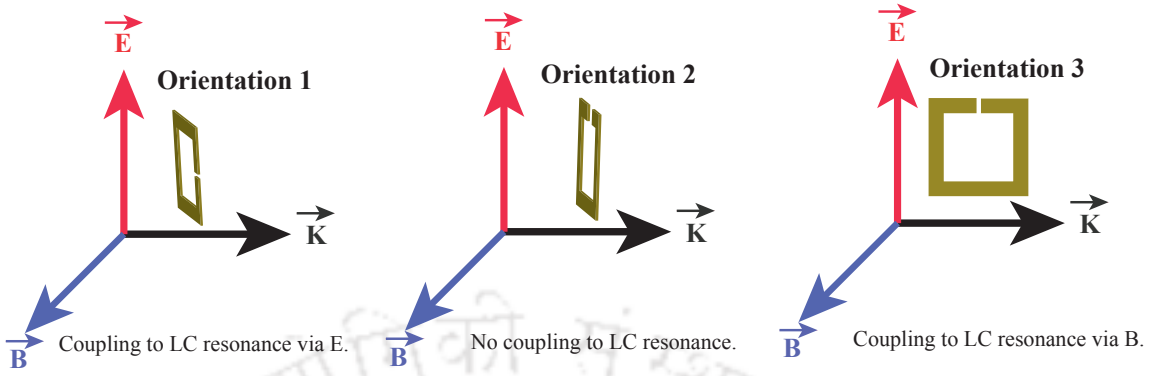

Figure 1.5: Different orientations of a SRR based on incident electric filed direction.

1.2.1 Polarization dependence of the SRRs

In order to obtain a magnetic response at higher frequencies, the orientation of SRRs in metamaterial plays very important role. The different orientations of SRRs with respect to the external electromagnetic field are shown in Fig. 1.5 [67]. The SRR act as an LC circuit in response to the external field. In the SRR, the split gap provides the capacitance and metal circumference act as an inductance. One can estimate the resonance frequency by carefully calculating the L and C values from SRR geometry ($\omega = 1/\sqrt{LC}$). For this LC oscillator, one can excite the fundamental LC resonance in two ways: either magnetic field vector must penetrate through the SRR loop (through inductor) [When a time changing magnetic field penetrates through the metallic rings, it induces an EMF by Faraday's law of electromagnetic induction which in turn produces a rotating current], or the projection of electric field should be normal to the capacitor plate (E field is parallel to the SRR gap)[51]. From Fig. 1.5, if the incident electric field direction is parallel to the SRR gap (Orientation 1 in Fig. 1.5), then transmission through the metamaterial sample shows odd order resonances. In this response, the first order mode is the fundamental LC resonance and remaining are the higher order resonance modes. In this orientation, magnetic dipole is possible due to the asymmetric mode of excited current in the SRR loop.

If the incident electric field direction is perpendicular to the SRR gap (Orientation 2 in Fig. 1.5), then the transmission through the metamaterial sample shows the even order resonance. In this response, the first resonance mode is the dipole resonance. In this orientation magnetic dipole is not possible because identical currents will be excited

in the two arms of SRR, and no loop-like current form in the SRR. In Fig. 1.5 (Orientation 3), if the incident electric field direction is parallel to arms of SRR, i.e. magnetic field vector penetrates through the SRR, then the transmission through the metamaterial sample shows LC resonance. In this orientation, magnetic dipole can be excited by the external magnetic field. In our entire study, we excited the fundamental LC resonance through Orientation 1 [46, 68].

One of the major application of terahertz metamaterials is the resonance modulation in the active and passive modes. It has been a challenge to realize frequency-tunable metamaterials in the terahertz domain. It may be noted that these designs only control the resonant properties of one or a handful of individual metamaterial elements. Thus, these techniques are not suitable at terahertz and higher frequencies. In this scenario, Padilla *et al*. utilize the terahertz time domain spectroscopy to characterize the electromagnetic response of a planar array of SRRs fabricated upon semi-insulating gallium arsenide. In addition to characterizing both the responses, they demonstrate for the first time the potential for creating dynamic SRR structures. This is accomplished through photo-excitation of free carriers in the GaAs substrate, which short out the SRR gap, thereby turning off the electric resonance and demonstrating the potential of SRR-based artificial materials as terahertz switches [69]. Singh *et al*. account an experimental observation of three distinct resonances in split ring resonators (SRRs) for both vertical and horizontal electric field polarizations at normal incidence by use of terahertz time domain spectroscopy. Breaking the symmetry in SRRs by gradually displacing the capacitive gap from the center towards the corner of the ring allows for an 85% modulation of the fundamental inductive-capacitive resonance [70].

1.2.2 Near-field coupling in terahertz metamaterials

Several studies have been reported on THz transmission in two dimensional MMs using single SRR as a unit cell [71, 72]. When two SRRs are brought sufficiently close to each other (Fig. 1.6 (b)), they can interact through magnetic and electric field lines, giving rise to novel phenomena and interesting applications that may not exist in conventional uncoupled metamaterials, such as mode hybridization effect, broadband modulation, wave modulation, polarization rotation, plasmon induced transparency (PIT), chirality [61, 73–75] etc. Generally, near-field coupling is important when the distance between the SRRs is much less than the excited wavelength (λ) and much smaller than the unit

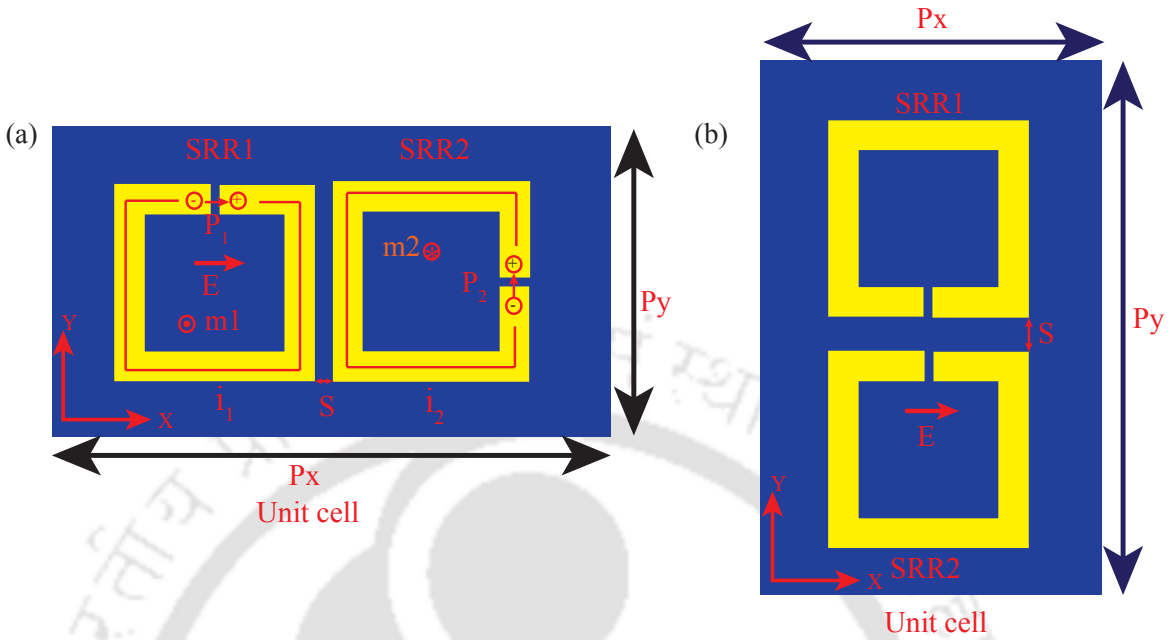

Figure 1.6: Schematic diagram of near field coupled SRRs in a unit cell. (a) Orthogonally twisted inductively coupled unit cell of planar terahertz metamaterial. (b) Capacitive coupled unit cell of planar terahertz metamaterial. P_x and P_y are the periodicities of x and y directions, respectively. S represents separation between two SRRs in a unit cell. Yellow color represents gold metal and blue color represents substrate.

cell dimensions. In order to modify the materials overall response, mutual coupling plays a significant role. In this context, broadly, two types of SRRs are investigated, they are broad side coupled SRRs (BC-SRRs) [76] and edge coupled SRRs (EC-SRRs) (Fig. 1.6 (a)) [73, 77, 78]. In the orthogonally twisted system, SRR pair consists of two identical SRRs (Fig 1.6 (a)). When the incident polarization of the electrical field is parallel to the split gap of SRR1 (x-direction) in Fig. 1.6 (a), the fundamental LC resonance is excited in SRR1. This circulating current, i_1 created in SRR1, creates an artificial magnetic dipole m_1 and the accumulated charges at the capacitive gap of SRR1 form an electric dipole, p_1 along the E field direction. Because of its orientation, the fundamental resonance mode of SRR2 cannot be directly excited with the same E field polarization.

The directly excited electrical dipole in such a configuration at the split gap of the SRR1 is located relatively far from the SRR2, and hence the electrical field coupling between the two SRRs is negligible, resulting in minimal electrical coupling to the SRR2. However, when two SRR gaps are arranged face-to-face, they result in strong capacitive coupling [79] (Fig. 1.6 (b)). The SRR pair, however, represents two inductively coupled

electrical loops, where the excited magnetic field of m_1 extends far beyond the SRR1, allowing sufficient near field coupling of the excitation to the SRR2. The coupling excites the fundamental resonance mode represented by the circulating current i_2, magnetic dipole m_2, and electric dipole p_2 in y direction in the SRR2 (see Fig 1.6 (a)). Upon incidence of a linearly polarized light, SRR1 is directly excited and it is termed as bright resonator, whereas the other resonator (SRR2) is excited indirectly through the bright resonator, hence called as dark resonator [73, 80, 81]. In case of MMs configuration, when both the SRR gaps are aligned parallel to incident electric field (see Fig 1.6 (b)), the fundamental modes are directly excited in both the resonators [79]. Recently, a lot of emphasis has been given to explore near field coupling in terahertz metamaterials owing to its significance in the construction of terahertz photonic components.

1.2.3 Ultrafast switching in terahertz metamaterials

For building devices and components in the terahertz domain, a strong resonant response and their ultrafast control in planar metamaterials is needed. Using metamaterials with an externally controllable agent active tunable response can be achieved. For example, the dielectric constant of substrate determines the frequency of metamaterial resonance together with the dimensions of the structure. On the other hand, the loss in metal and substrate sets the strength of the oscillator. This motivates many researchers to consider semiconductors as metamaterial substrates, where the conductivity (or loss) can be modified conveniently when an external stimulus such as temperature, voltage bias, or photo-excitation is applied. Due to the simplicity and ultrafast tuning capability, the optical approach received intensive attention in metamaterial researches. The switching of metamaterial resonances is mainly determined by the photo-excitation of free carriers in the substrate of the semiconductor, which could occur very quickly using femtosecond laser pulses. If the semiconductor is GaAs, the recovery of the switching may not be very fast, as the lifetime of the carrier can be as long as nanoseconds [82]. For many applications, ultrafast switching response is highly desirable. Radiation damaged silicon or GaAs grown at low temperature substrates can overcome this problem, where the lifetime of the free carrier can be at sub – picosecond [73, 83] time scale. The photo - induced free carriers increase the conductivity on the surface of the substrate, thereby shortening the split gaps in metamaterials when the incident electromagnetic fields excite them. This results in turning of the metamaterial resonance. Resonance mode

switching in ultrafast time scale has potential in making the ultrafast terahertz devices, such as switches and modulators [84]. In this context, Cong *et al*. have introduced an active hybrid metasurface integrated with patterned semiconductor for active control of terahertz waves. Ultrafast modulation of polarization states and the beam splitting ratio are experimentally demonstrated on a time scale of 667 ps. [85]. Lim *et al*. experimentally studied a germanium-thin-film-based flexible metaphotonic device for ultrafast optical switching of terahertz radiation. A resonant transmission modulation depth of 90% is achieved, with an ultrafast full recovery time of 17 ps [86]. Yogesh *et al*. has investigated the photo-active properties of MoS_2 to demonstrate an ultra-sensitive active switching and modulation of the sharp Fano resonances in MoS_2-coated metamaterials consisting of asymmetric split ring resonator arrays. The results show that optical switching and modulation of micrometer scale sub-wavelength Fano resonators can be achieved on a timescale of hundred picoseconds at moderate excitation pump fluences [87].

1.3 Motivation of the thesis

In my Ph.D. research work, my focus has been in studying the near field coupling and ultrafast switching of resonances in THz metamaterials. As we have discussed earlier that the metamaterials in near field coupled configuration consist of one or more than one SRR (meta-atoms) in a unit cell. The intelligent manipulation of near field coupling between these resonators, can have significant impact on the metamaterials responses. Therefore, controlling the near field coupling in metamaterials is extremely crucial in order to design and fabricate the terahertz photonic components viz. modulators, filters, polarization rotation etc. By nature, near field coupling in metamaterials could be resistive, capacitive or inductive. Several near field coupling mechanisms have been studied in recent past using different schemes, however these coupling mechanisms have been extensively electric and magnetic in nature [61, 73, 79]. Although, the investigations on near field coupling in terahertz metamaterials have led to many interesting physics and engineering, but actualization of terahertz devices using such near field coupled metamaterials require more rigorous study in terms of their control and manipulation both passively and actively. In my first three problems, we have mainly focused upon passive control of near field coupling in terahertz metamaterial structures. In my last problem, we have explored the possibility to tune resonances at ultrafast time scale by a material inside the SRR gap.

1.4 Plan of thesis

In this thesis work, we have investigated near field coupling and ultrafast switching in terahertz metamaterials by using split ring resonators as a unit cell. Using terahertz metamaterial structures, we have explored the possibility to tune the coupled resonances based on near field inductive coupling and near field capacitive coupling. In planar terahertz metamaterial structures by changing the inter cell distance between SRRs and by changing the gap size of SRRs we engineered the resonances. We have also investigated the potential of ultrafast switching in terahertz metamaterials with selective photo doping. The work proposed in this thesis has been divided into seven chapters, with the first chapter presenting an overview of the THz metamaterials research and recent developments. The technical details of the method adopted in carrying out the research work will be presented in the second chapter. The next four chapters will deal with the near field coupling and ultrafast switching in terahertz metamaterials as well as various interesting properties exhibited by them. In the last chapter, I will summarize the important findings and discuss the scope of future works based upon our findings. A chapter wise summary of the thesis is as follows:

Chapter 1: This chapter presents an overview of the field of terahertz and briefly discusses the properties and applications of terahertz frequencies. The discovery of metamaterials, near field coupling and ultrafast switching in terahertz metamaterials is introduced. The prospects of near field coupling and ultrafast switching in various applications is also be elaborated to illustrate the attractiveness of its features.

Chapter 2: This chapter explains the designing of terahertz metamaterials by using CST microwave studio, and procedure to fabricate samples which involves photo lithography, metal deposition, and lift off process. In addition we discuss, two main spectroscopy methods namely, terahertz time domain spectroscopy (THz TDS) and optical-pump terahertz-probe (OPTP) spectroscopy, that we employed for the measurement of THz metasurfaces samples. Further, RLC theoretical model is explained with a motive to understand theoretical aspects of the MMs.

Chapter 3: In this chapter, we studied the effect of vertical displacements between the resonators inside the unit cell of planar coupled metamaterials on their near field coupling and hence, on the terahertz (THz) wave modulation. The metamolecule design consists of two planar SRRs in a unit cell which are coupled through their near fields. The numerically simulated transmission spectrum is found to exhibit mode hybridization

effect due to the coupling between two resonance modes of coupled resonators. With the increase in displacement between the near fields coupled SRRs, this metamaterial system shows a transition from coupled to uncoupled state through merging of the two resonances to the single intrinsic resonance. We have used a semi-analytical model describing the effect of displacements between the resonators and determine that it can predict the numerically simulated results. The outcome could be useful in modulating the terahertz waves employing near field coupled metamaterials, hence can be useful in the development of terahertz modulators and frequency tunable devices in future.

Chapter 4: In this chapter, we discuss the near field coupling between the pair of SRRs in broadside coupled terahertz metamaterials and examine mode hybridization and tuning of resonances in such metamaterials system. The metamolecule design is comprised of two orthogonally twisted broadside coupled SRRs separated by a thin micro-scale polyimide layer. We analyze the interaction between the meta-layers numerically and analytically by displacing the top resonator w.r.t. the bottom resonator both in the horizontal and vertical directions. The terahertz transmission through proposed configuration results in the mode hybridization effect due to the coupling between two fundamental resonances of coupled resonators. In the case of successive horizontal displacements between the resonators, we observe a complete shift from the coupled to uncoupled state, however in vertical displacements, we notice the transition from coupled to uncoupled state at much larger displacement. We employ a semi-analytical transmission line model to understand and describe the coupling aspect between the bilayer resonators and found that it corroborates the numerical findings. The ability to tune resonance behavior that we have examined through this work, could be significant in the development of frequency tunable terahertz devices and build other promising applications such as terahertz modulators and antennas in near future.

Chapter 5: In this chapter, we experimentally investigate the near field capacitive coupling between a pair of single split gap ring resonators in a terahertz metamaterial. The unit cell of our design comprises of two coupled SRRs with the split gaps facing each other. The coupling between two SRRs is examined by changing the gap of one resonator with respect to the other for several inter resonator separations. When split gap size of one resonator is increased for a fixed inter-resonator distance, we observe a mode hybridization effect. This mode hybridization ultimately results in the excitation of narrow band low frequency resonance mode along with a higher frequency mode which gets blue shifted when the split gap increases. We attribute the mode hybridization to

the excitation of symmetric and asymmetric modes due to strong capacitive or electric interaction between the near field coupled resonators, however blue shift of the higher frequency mode occurs mainly due to the reduced capacitance. The ability of near field capacitive coupled terahertz metamaterials to excite split resonances could be significant in the construction of modulator and sensing devices beside other potential applications for terahertz domain.

Chapter 6: In this chapter, we experimentally demonstrate ultrafast switching of resonant mode in terahertz metamaterials through optical excitation of radiation damaged silicon placed in the gap of a SRR. Upon optical excitation, we observe the dynamic transition of the fundamental resonance from ON-to-OFF state in a time scale of 4 picoseconds (ps) and then fast recovery of the resonance to the ON-state within next 20 ps. Electric field distributions in the metamaterials unit cell derived through numerical simulations clearly support our experimental observations, showing that the high electric field at the resonator gaps, responsible for inductive-capacitive (LC) resonance, completely disappears and switches OFF the resonance after being optically excited. The ultrafast switching of the metamaterial resonance is attributed to the relaxation of the photo-carriers through the defect-states of radiation-damaged silicon layer. Such ultrafast materials based active control of metamaterials can lead to the realization of ultrafast terahertz metaphotonic devices.

Chapter 7: Finally, in chapter 7, we provide a conclusion of the thesis along with a summary of the major findings of the research work carried out. We also discuss the future scope of work based upon the works done in terahertz metamaterials in this thesis.

CHAPTER 2

METHODOLOGY

The methodology comprises of different steps that are followed for the execution of a research plan. For the research work proposed in this thesis, we have used following four steps:

- Design of terahertz metamaterials
- Sample preparation
- Characterization
- Theoretical study

Here is the detailed discussion to all the important steps.

2.1 Design of terahertz metamaterials

The design of terahertz metamaterial structures and their optimization is one of the important step before proceeding to the complex and expensive fabrication process. We designed THz metasurfaces using a commercially available numerical software, named Computer Simulation Technology Microwave Studio (CST MWS) [88]. It is one of the application module in CST studio suite (Fig. 2.1). Basically, it is an electromagnetic full wave numerical simulation software which relies on solving Maxwell's equations using

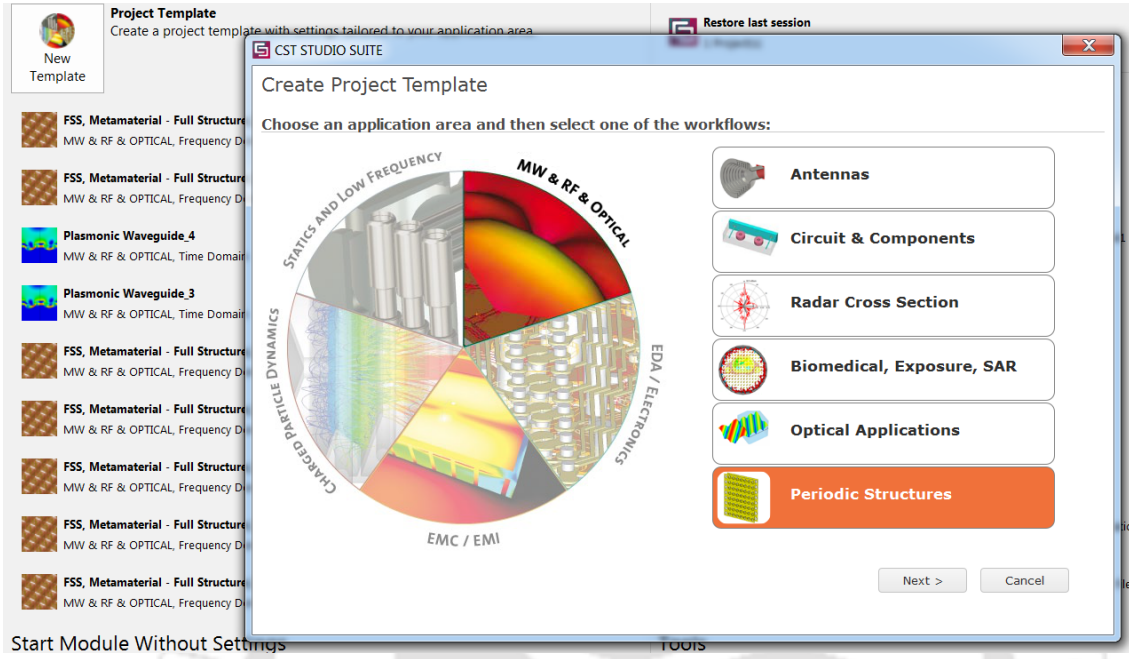

Figure 2.1: Starting page of CST micro wave studio simulation software.

the Finite Integration Algorithm. CST MWS gives ability to solve a given problem in several domains such as time domain, frequency domain and Eigen frequency mode, etc. In order to solve an electromagnetic problem in CST MWS, the simulation area is first divided into small cells (or meshes) and then Maxwell's equations are solved with suitable boundary conditions. The software gives several meshing options, the main ones being the hexahedral and the tetrahedral mesh. With the hexahedral mesh, the whole simulation area is divided into small uniform cubes of variable sizes, whereas in case of the tetrahedral mesh, only objects are divided in small tetrahedrons and the rest of the simulation area is left unmeshed. Due to the intrinsic features in each mesh type, there are some important differences. The mesh defines the accuracy and the speed of simulation. Small mesh cells usually lead to more accurate solutions, but at the cost of computation time. Generally hexahedral meshing takes less simulation time, in accuracy tetrahedral meshing is more reliable. One of the important feature offered by the simulation tool is time domain solvers, which gives the flexibility to simulate entire broadband frequency response in a single run. This solver is remarkably efficient for many high frequency applications such as connectors, transmission lines, waveguide components, antennas, etc. The time domain solver is less efficient for structures that

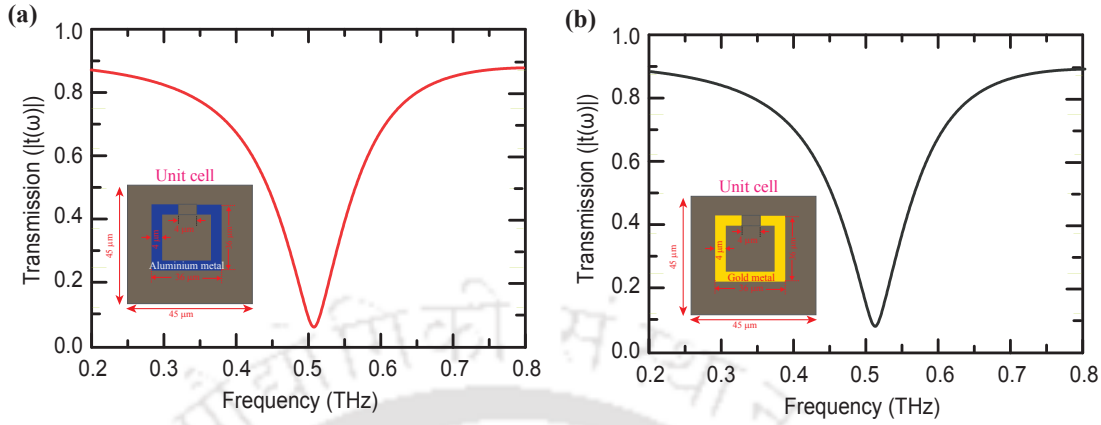

Figure 2.2: Simulation results (a) Transmission result for aluminum resonators as a unit cell. In the unit cell diagram, blue color represents aluminum metal and grey color represents silicon lossy free substrate. (b) Transmission result for gold resonators as a unit cell. In the unit cell diagram, yellow color represents gold metal and grey color represents silicon lossy free substrate.

are electrically much smaller than the shortest wavelength of interest. In such cases, it may be advantageous to solve a problem using a frequency domain solver. The frequency domain solver is ideally suited for periodic structures. The metamaterial structures under study are periodic in nature, and therefore, we have used frequency domain solver. In all the simulations, tetrahedral mesh is employed for better accuracy. We have used waveguide ports for the source and detector to resemble with plane wave excitation under the normal incidence. We have used periodic boundary conditions to simulate an infinite array of two-dimensional periodic structures. The transmission and reflection results are stored in the S-parameters. In the transmission verses frequency results, we have plotted S-parameter magnitude i.e. ($|S_{21}|$). In all transmission plots, we mentioned Transmission (|t(ω)|) in y-axis.

In order to simulate structures proposed through this thesis work, we have used gold (Au) and aluminum (Al) as the metals to design resonators. Electric conductivities of gold (Au) and aluminum (Al) are Au = 4.56×10^7 S/m and Al = 3.56×10^7 S/m, respectively. Since the conductivities are very close to each other, the MM response to incident terahertz is almost similar (see Fig. 2.2). For substrates, we have either used loss free silicon with dielectric constant, ϵ= 11.9 or Gallium Arsenide (GaAs) with dielectric constant, ϵ = 12.94, depending upon availability of the substrate for experimentation.

2.2 Sample preparation

The design of metamaterial structures with optimized parameters is followed by fabrication process which required several steps to be followed with utmost precision. For the fabrication of samples, we used conventional photo-lithography technique in the clean room environment. The samples were fabricated on a 500 μm thick high resistivity (> 5000 ohm-cm) silicon substrate. Followed by photo-lithography, a 200 *nm* thick aluminum layer was deposited by using a thermal evaporator, after which a lift-off process enabled the formation of the SRR array (Fig. 2.3). For a research project on ultrafast switching in THz metamaterial, the samples were fabricated using two-step photo-lithography. The first photo-lithography is performed to create patterns to form metal resonators. Followed by this step, 10 *nm* thick titanium and 200 *nm* thick gold layer is deposited by electron beam evaporation, which is then lifted-off to form the single gap SRR array. In the second step, photo-lithography is performed to cover the split gap of the SRR and to expose the remaining silicon layer across the entire sample area. With reactive ion etching, Silicon is removed from the entire sample except the gap regions of the SRR which are masked by the photo-resist.

The basic steps in photo lithography are

1. Step 1 (Cleaning wafer): As part of fabricating metamaterials samples, first we clean the wafer with acetone, ethanol, isopropanol, and deionized water followed by treating with dry air.

2. Step 2 (Spin coating a Photo resist (AZ 4533)): The fabrication process began with spin - coating a photo resist (AZ 4533) on silicon wafer. Photo resist is placed on the wafer and spin coated. We programmed two steps for spin coating. In step 1, we have taken rotation per minute (RPM) = 500, acceleration time = 10 sec, and rotation time = 10 sec. In step 2, RPM = 4000, acceleration time = 30 sec, and rotation time = 30sec. After spin coating, baking the substrate is very important. We baked at 90^0C for 60 seconds.

3. Step 3 (UV exposure on pattern): After photo resist coating, we made the desired pattern on the wafer by photo lithography. Using mask aligner we exposed UV light through photo mask on photo resist coated wafer (photo mask contains our desired structures). We have tried with three exposure times a). 2 seconds b). 2.5 seconds c). 3 seconds, finally we used 2.5 seconds exposure time. Photo lithography allowed

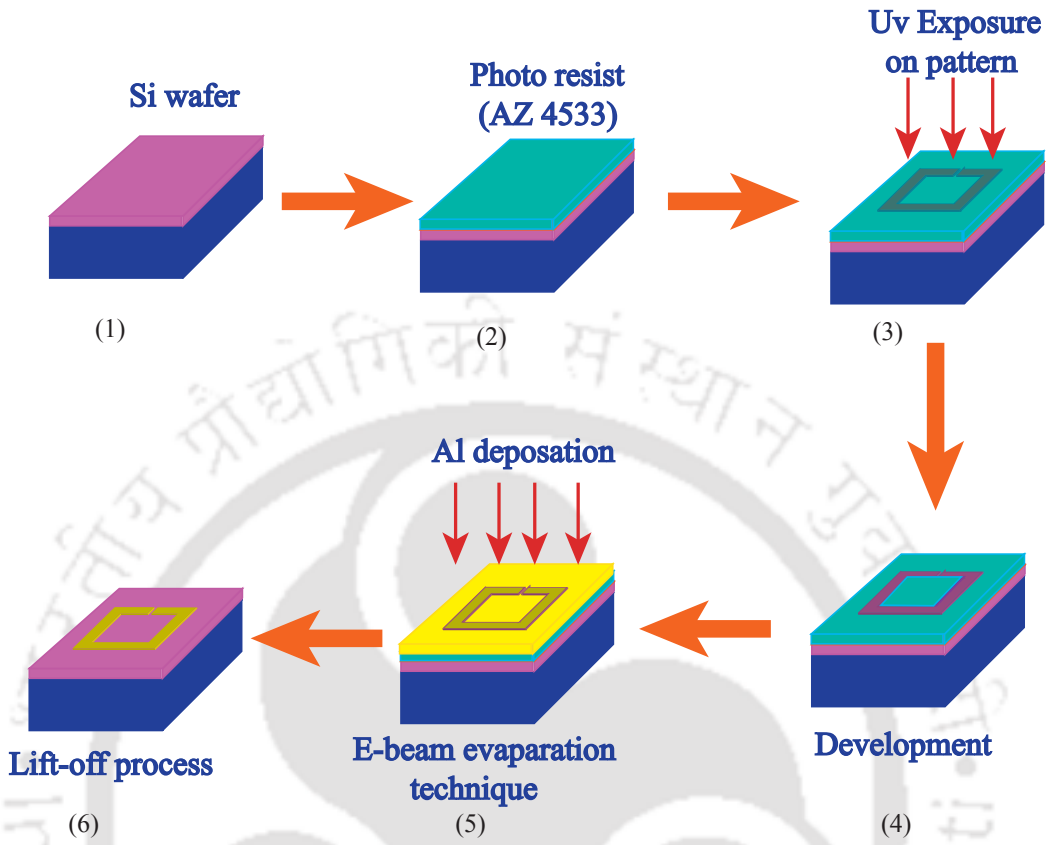

Figure 2.3: Schematic of the entire fabrication process starting from 1 to 6 in a clockwise fashion.

us to attain very small feature sizes (2 μm) with reasonably good resolution. This UV light changes the photo resist property at patterns.

4. Step 4 (Development, AZ 400 K Developer): After finishing pattern on wafer, we treated wafer with developer and deionized water in the ratio 1:3. When we put wafer in developer, where ever photo resist property changed that places photo resist will come out and remaining places photo resist stays as it is. For particular photo-resist (AZ 4533), we have to use particular developer (AZ 400 K). First we make developer solution using 50 ml developer and 150 ml deionized water and mix both and keep in a beaker. Keep wafer in developer liquid for 20 seconds, after that put wafer in deionized water for 30 seconds.

5. Step 5 (Metalization): After development, we have deposited 200 *nm* thickness aluminum metal on wafer by using standard E-beam evaporation technique.

6. Step 6 (Lift – off procedure): After metalization, the sample is placed in an acetone

container. The acetone will remove the photo resist. Wherever photo resist is not present on wafer, metal will stay. From the remaining places, metal comes out with the photo-resist.

2.3 THz characterization of the metamaterial structures

For characterization, we used Terahertz time domain spectroscopy (THz-TDS) technique [89] (Fig. 2.4). In this technique, a beam from a femtosecond (fs) laser system is divided into two beams using a beam-splitter, called as probe and pump beams. The pump beam is used to generate THz pulses, while the probe beam is used to sample and obtain the pulse profile. Detection of THz field is performed by modulating the probe pulse with the THz field or by accelerating free carriers induced by the probe pulse with the THz field. A mechanical delay stage is used to provide the required time delay between THz pulse and the probe pulse. THz waveform can be obtained by scanning this time delay. To increase the sensitivity, the pump beam is modulated by an optical chopper and the THz induced modulation on the probe beam is extracted by a lock-in amplifier. This pulse information acquired in the time domain is transformed to the frequency domain through Fast Fourier Transformation from which spectral information can be obtained (see Fig. 2.5). The normalized transmission (|t(ω)|) spectrum of the sample is determined by taking the ratio between Fourier transforms of the measured time-domain terahertz pulses of the sample (| $E_S(\omega)$ |) and reference (| E_R (ω) |).

Since the spectroscopic measurements through this technique are carried out by recording the THz waveform in the time domain, this technique is called THz-time-domain spectroscopy (THz-TDS). In a pulsed THz system, the probe pulse samples the THz pulse and records its electric field as a function of time. The THz field in the frequency domain is a complex value, which consists of amplitude and phase information. In our THz-TDS technique, we used photo-conductive antenna for generation and detection. The photo-conductive antenna (PCA) is one of the most widely used technique of generating and detecting THz.

It generates and detects THz pulses by transient photo carriers induced with ultrafast laser pulses. PCA consists of two metal electrodes that are coated on a Lt-GaAs substrate with a gap between these two electrodes. To generate THz pulses, voltage is applied

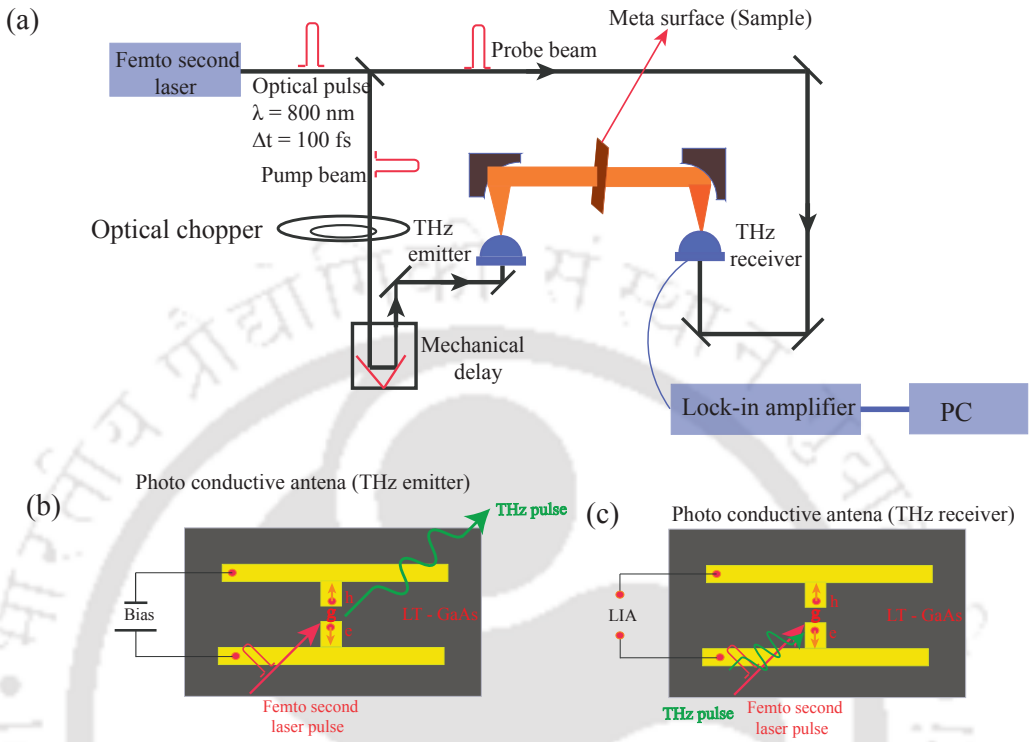

Figure 2.4: (a) Schematic of the terahertz time domain spectroscopy setup. Photoconductive antennas are used as the terahertz source and detector. (b) & (c) A schematic of the photoconductive antenna comprising two transmission lines with two poles separated by a distance 'g'. The LT-GaAs is used as the substrate for fabricating antenna.

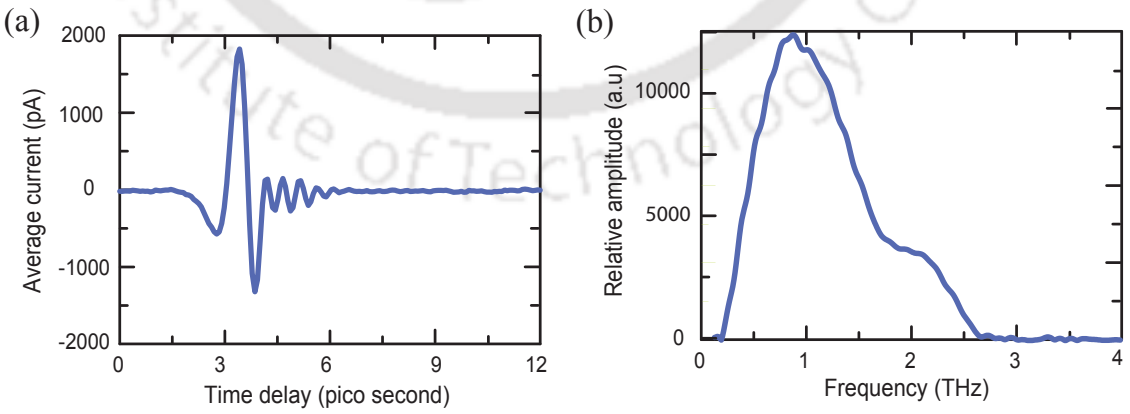

Figure 2.5: Time domain signal converted to frequency domain by using Fourier transformation. (a) Transmission signal in time domain. (b). Transmission in frequency domain. [89]

across the electrodes. Since the substrate is semi-insulating, electric energy is stored in the gap area. Ultrafast laser pulses act like transient switches to open this reservoir of electric energy and release it in the form THz pulses. Polarization of the THz wave radiated is parallel to the biased field which is perpendicular to the transmission lines as shown in Fig. 2. 4 (b) and (c). Polarization of THz wave can be altered by switching the polarization of bias voltage. By doing so, the laser pulses must have enough photon energy in order to generate photo induced free carriers in the substrate. Generally, the photon energy of the excitation pulse should be higher than the band gap of the substrate. Therefore, more the carriers are generated by the femtosecond pulse, stronger is the radiated terahertz field. It should be noted that other parameters such as bias voltage, materials properties as well as the areas between the transmission lines also plays an important role in defining the bandwidth as well as the radiated electromagnetic field. The measurements were carried out using a typical 4f confocal terahertz time-domain spectroscopy (THz-TDS) system consisting of a photo-conductive antenna transmitter and a receiver. The metallic antenna on GaAs chip is dc biased at 70 V and excited by 130 fs optical pulses with a wavelength of 800 nm and a repetition rate of 80 MHz from a Ti: sapphire oscillator laser system generating THz pulses with a bandwidth of 0.2 THz – 3 THz.

All the measurements were performed at room temperature and in a dry atmosphere in order to mitigate unwanted absorption introduced by the presence of water vapor in the ambient air. In one of the research project, active metamaterial samples were characterized by using the optical pump terahertz probe (OPTP) measurement technique (see Fig.2.6). A near-infrared femtosecond (fs) laser beam, with a pulse duration of 30 fs, energy of 3.2 mJ/pulse operating at 800 nm with a 1 kHz repetition rate, was employed for terahertz generation/detection and optically pumping the sample. The pump laser beam had a beam diameter of 1 cm, much larger than the focused THz spot diameter of 3 mm at the sample, providing uniform excitation over the metamaterial sample. The time delay between optical-pump and terahertz-probe pulses was precisely controlled using a linear translation stage to change the optical path length of the femtosecond optical pulses. For several pump-probe time delays, the THz signal was measured in the time domain after transmission through the metamaterial samples. The time domain signals were transformed to the frequency domain (see Fig. 2.5) and normalized using a bare sapphire substrate as the reference. In the experimental results, we have plotted the frequency (THz) verses transmission magnitude ($|t(\omega)|$).

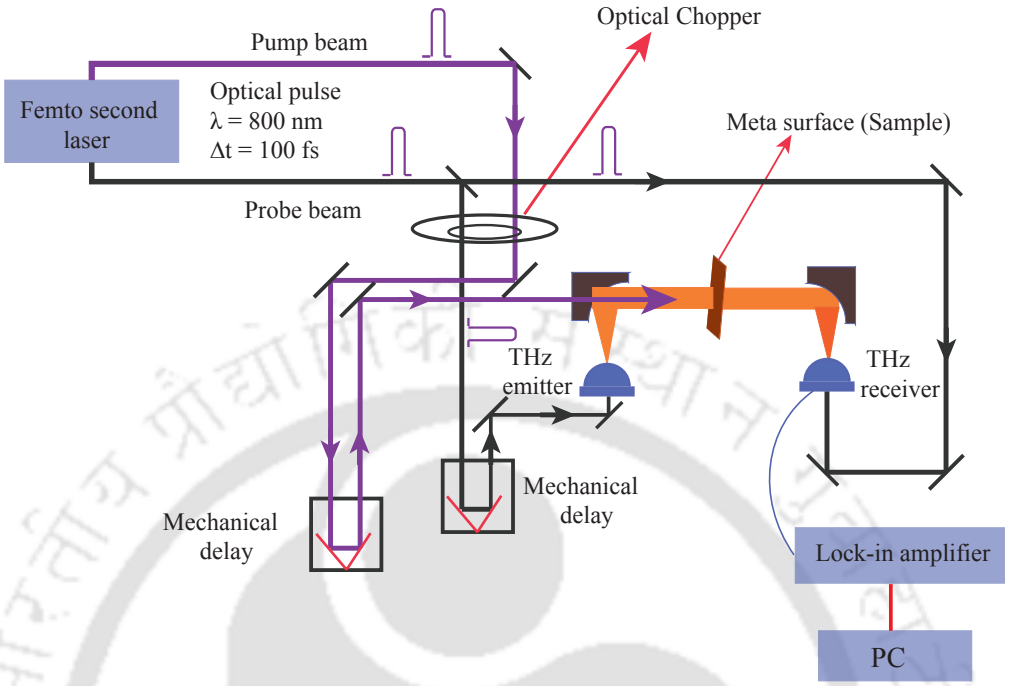

Figure 2.6: Schematic of the optical pump terahertz probe technique (OPTP) setup. Photoconductive antennas are used as the terahertz source and detector.

2.4 Theoretical model

In order to understand the resonant behavior of the transmission properties through coupled terahertz metamaterials and to explain the transitions between the coupled and uncoupled states of the resonances, we employed a semi-analytical RLC circuit model. This model has the ability to give us a flavor of the resonant transmission behavior through the proposed THz metamaterials system. The behavior of the main lorentzian resonance in SRRs is well known and follows the form of a series RLC circuit. In this semi-analytical approach, a single SRR is modeled with an equivalent RLC circuit which exhibits resonance at a specific frequency depending upon the shape and size of the split ring resonator (Fig. 2.7). In SRR, the gap acts like a capacitor of capacitance C. Capacitance is due to the charge accumulation at the gaps of SRR. The SRR loop behaves like an inductor of inductance, L. Inductance is due to current circulating around the SRR perimeter. The predominant contribution to resistance (R) of metallic SRR is radiation resistance. The inductance of the SRR is determined by geometric dimensions. From inductance value, we can estimate capacitence value at the resonance frequency by using $\omega = 1/\sqrt{LC}$. The resistance can be estimated from the quality factor (Q = $\frac{1}{R}\sqrt{\frac{L}{C}}$) of the

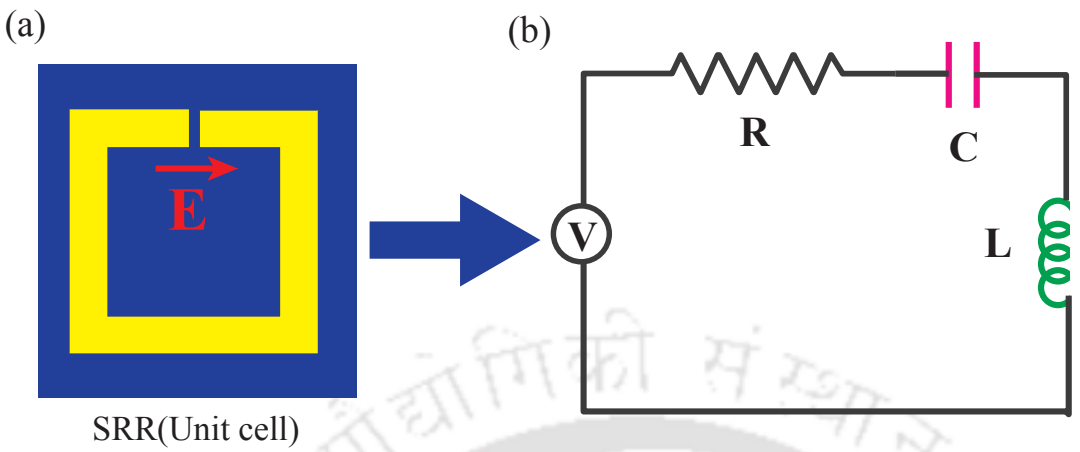

Figure 2.7: Schematic diagram of split ring resonator and equalnet RLC circuit. (a) Split ring resonator, yellow region represents metallic area and blue region represents substrate. (b) Equivalent RLC circuit.

resonance[81].

To calculate the transmission behavior through single SRR metamaterial, first we calculate the total impedance of the circuit and substitute this value into transmission formula and at particular R, L, and C values, it gives the transmission behavior through the sample [90].

$$Z_{tot} = R + j\omega L + \frac{1}{j\omega C} \tag{2.1}$$

$$t(\omega) = \frac{2Z_{tot}}{Z_{tot} + Z_0} \times \frac{Z_s + Z_0}{2Z_s} \tag{2.2}$$

where Z_s is the impedance of the substrate and Z_0 is the impedance of the free space. At particular R, L, and C values for the SRR, we calculate the terahertz transmission through the metamaterial sample and analyze them w.r.t. the corresponding to the measured values.

So far, we have discussed RLC circuit model for the metamaterial system comprising only a single SRR as its unit cell. In coupled metamaterial system, we have two split ring resonators placed in a near field regions and constitutes a unit cell. We shall now discuss RLC circuit model for a near field inductively coupled metamaterial system (Fig. 2.8) Suppose, two RLC circuits have resistances, inductances and capacitances as R_1, L_1, C_1 and R_2, L_2, C_2 corresponding to the left and right resonators, respectively and M is the coupling between two resonators. In this model we assumed one resonator is a

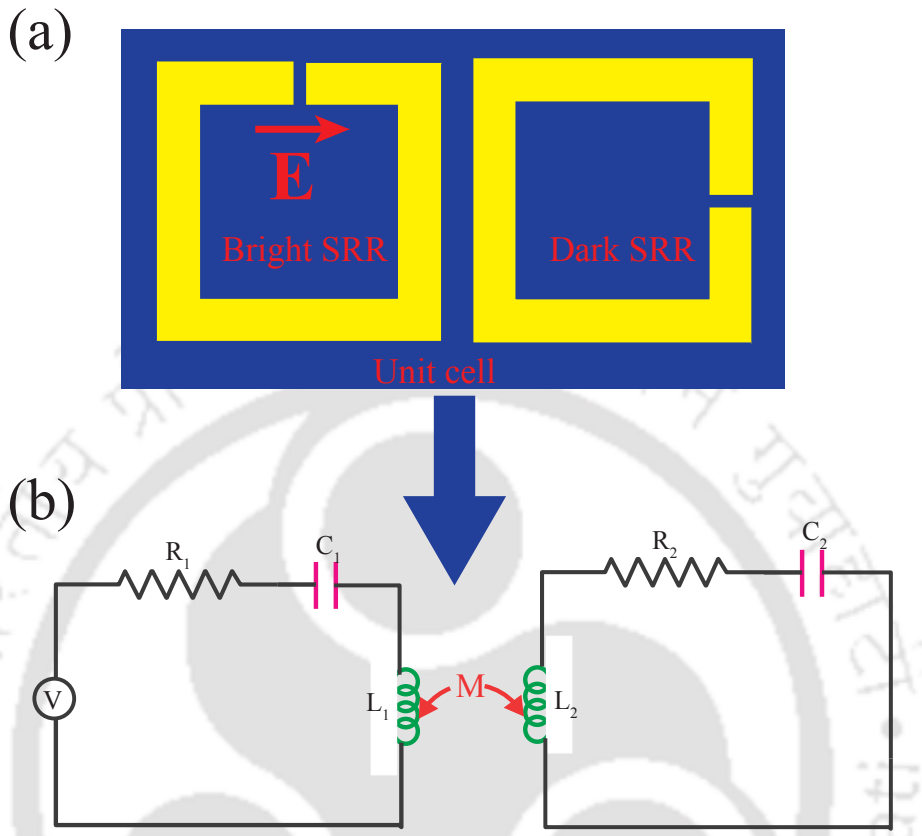

Figure 2.8: Schematic diagram of coupled SRRs (unit cell) and corresponding RLC circuit. (a) Two coupled SRRs, yellow region represents metallic area and blue region represents substrate. (b) Equivalent RLC circuit for coupled SRRs.

bright resonator (directly excited resonator) and another resonator as the dark resonator (indirectly excited resonator through bright resonator) [91]. By using circuit analysis, we calculate the total impedance of the circuit [92]. The total impedance of the circuit is given by

$$Z_{tot} = \frac{Z_1 Z_2 + \omega^2 M^2}{Z_1 + Z_2 - j\omega 2M} \tag{2.3}$$

where, 'M' = mutual inductance. The mutual inductance depends on the coupling strength and decreases when the separation between the two SRRs increases,

$$Z_1 = R_1 + j\omega L_1 + \frac{1}{j\omega C_1}$$

and

$$Z_2 = R_2 + j\omega L_2 + \frac{1}{j\omega C_2}.$$

The transmission formula is given by (transmission formula from TL-RLC model [91, 93]. In Chapter 3 and Chapter 4, we used this formula.)

$$t(\omega) = \frac{Z_{tot}(Z_s + Z_0)}{Z_s(Z_{tot} + Z_0) + (Z_{tot} \times Z_0)} \tag{2.4}$$

For particular R_1,L_1,C_1 and R_2, L_2, C_2 values for the two coupled SRR and specific mutual inductance value, we calculate terahertz transmission through the coupled metamaterial system and analyze the results.

It is important to mention that TL-RLC model (chapter 3 and chapter 4) has been previously employed to describe the coupling between two different modes of a single resonator[90–92]. We believe that this model is capable of describing the inter-resonator coupling too where two different resonances are arising. We believe that the resonances are arising from the oscillating currents in the resonators. We use the model to describe the coupling between two different resonators with electric or magnetic coupling present between them. Or in reality we are modeling two resonances coupled through electric or magnetic field lines. Simplistically, two resonators are represented by two RLC models, and the mutual inductance (M) between them which is responsible for magnetic coupling is considered in the model.

CHAPTER 3

STUDYING NEAR FIELD INDUCTIVE COUPLING IN PLANAR TERAHERTZ METAMATERIALS

The near field coupling in metamaterials happens via the electric and magnetic fields due to the close proximity of the nearest neighbor SRRs [94, 95]. Magnetic field coupling or near field inductive coupling mainly takes place through the circumference of the SRRs [80] and electric field coupling or near field capacitive coupling happens through the gaps of the SRRs [79]. In this chapter, we have focused on near field inductive coupling in edge side coupled planar terahertz metamaterials. To study the near field inductive coupling, we have taken two SRRs in a unit cell, these SRRs are placed orthogonal to each other and which minimize the effect of near field capacitive coupling since the gaps are distant to each other. In this configuration, the directly excited SRR is called the bright resonator and indirectly excited SRR is called as dark resonator (In Chapter 1, near field coupling terahertz metamaterial section, we have explained clearly about bright and dark resonators). In recent times, it has been established that the near field electromagnetic coupling among the SRRs within a meta-molecule can show attractive properties such as broadening of resonance, active chirality, electromagnetically induced transparency [96], polarization rotation [97, 98], etc. In this

An article based upon the work reported in this chapter is published in *Journal of Infrared, Millimeter, and Terahertz Waves*, vol. **38(1)**, year 2017, pages 124–134; title:"Modulating the near field coupling through resonator displacement in planar terahertz metamaterials"; authors SJM Rao, D Kumar, G Kumar, DR Chowdhury.

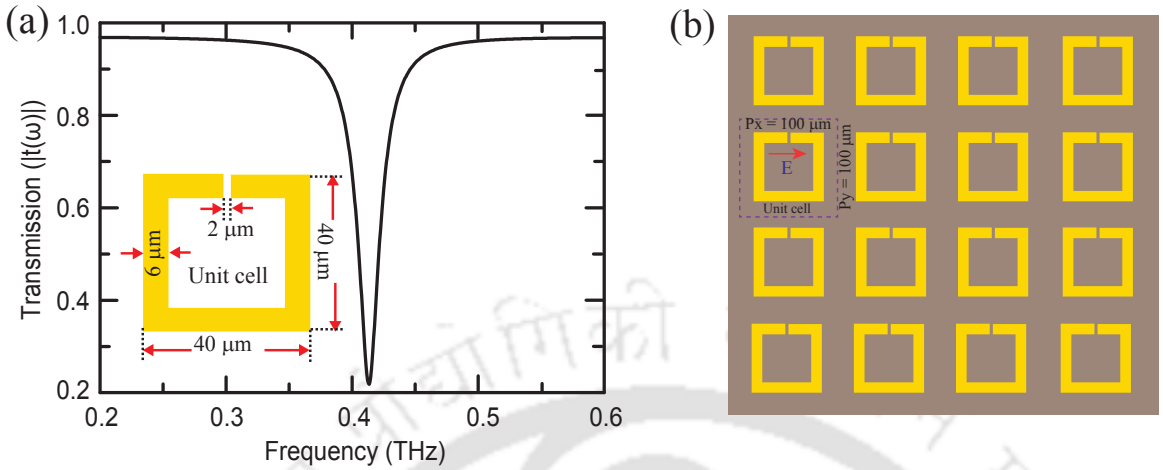

Figure 3.1: (a) Numerically calculated terahertz transmission through a metamaterial geometry having single SRR as a unit cell. (b) Schematic of 2D metamaterial having single resonator as a unit cell.

direction, Singh *et al*. studied near filed inductive coupling by using two orthogonally placed SRRs in a unit cell of planar terahertz metamaterial. In this study, they have taken two separations between SRRs in a unit cell and each separation they have varied the length of dark resonator. By using THz-TDS they have measured the transmission through the sample for each case and compared with simulation results [80]. In another study Singh *et al*. varied the separation between two identical SRRs in a unit cell of metamaterial and studied the terahertz transmission through metamaterial sample for each separation. They have confirmed that when the SRRs are close to each other (minimum separation between two resonators), both the resonators are strongly coupled through their magnetic field lines and SRRs are far away from each other (separations between two SRR is maximum), the near field coupling is absent [74].

Chowdhury *et al*. present the strongly coupled planar terahertz metamaterials in which the metamolecule design included two concentric SRRs with their split gaps oriented orthogonally in order to create strong near field coupling. When the incident terahertz radiation couples to the metamolecule system through the outer resonator, they observed strong split in the fundamental LC resonance. But, when the incident terahertz radiation couples to the metamolecule system through the inner resonator, they observed the strengths of split resonances are too weak [91]. Li *et al*. investigated the edge-coupling of orthogonally placed SRRs pairs in the terahertz frequency regime. They used two SRRs placed orthogonally in a unit cell of planar metamaterial and they

varied the separation between two SRRs. They studied the terahertz transmission and the transmission shows resonance splitting and cross-polarization conversions. They verified the resonance splitting as a function of the coupling strength given by the SRR separation [81]. Liu *et al*. studied the excitation and tuning of electromagnetically induced transparency (EIT) by the interference between different excitation pathways of the dark mode in a planar coupled terahertz metamaterial. In their study, the unit cell of metamaterial contains of a cut wire and a pair of split ring resonators, these pair of SRRs equally placed on the left and right side of a cut wire. The cut wire can be excited directly by the incident electric field, acting as the bright resonator, while the fundamental LC resonance in the SRRs cannot be excited by the incident E field because of wrong orientation, thus acting as the dark mode. It is the destructive interference between the bright and dark resonators that gives rise to a strong EIT effect. They have tuned the EIT resonance by translating the SRRs along the wire [99]. Cao *et al*. Studied EIT and slow-light behaviors via coupling of bright and dark sub-wavelength resonators. Here, they experimentally show a thermally active metal coupled resonator based hybrid terahertz metamaterial on a sapphire substrate that shows the tunable transparency and slow light behavior. In this metamaterial, the unit cell contains of a high-temperature superconductor close-ring resonator (CRR) that acts as a bright resonator and a metal split-ring resonator as a dark resonator [100]. So far many works are done to study near filed inductive coupling in terahertz metamaterials, but there are other challenges to be addressed in this direction.

In this chapter, we propose a scheme to tune metamaterials fundamental resonant response through manipulating the near field inductive coupling between the adjacent resonators inside a metamaterial unit cell. The proposed scheme can help to control the near field electromagnetic coupling which can be useful in implementing frequency tunable, polarization rotator metamaterials for terahertz frequencies. In our proposed planar metamaterials geometry, the unit cell comprises of two split ring resonators placed in planar configuration and terahertz transmission response is examined when one of the resonator is vertically displaced with respect to the other. We have discussed the effect of such displacement on the transmitted terahertz wave. In first section (3.1), we discuss the design of our geometry and study the effect of displacement of second resonator on the coupling of LC or first order resonances. Through terahertz transmission spectral response, we examine the effect of near field coupling between the resonators. In next section, we have studied the transmission response using a semi-analytical model specific

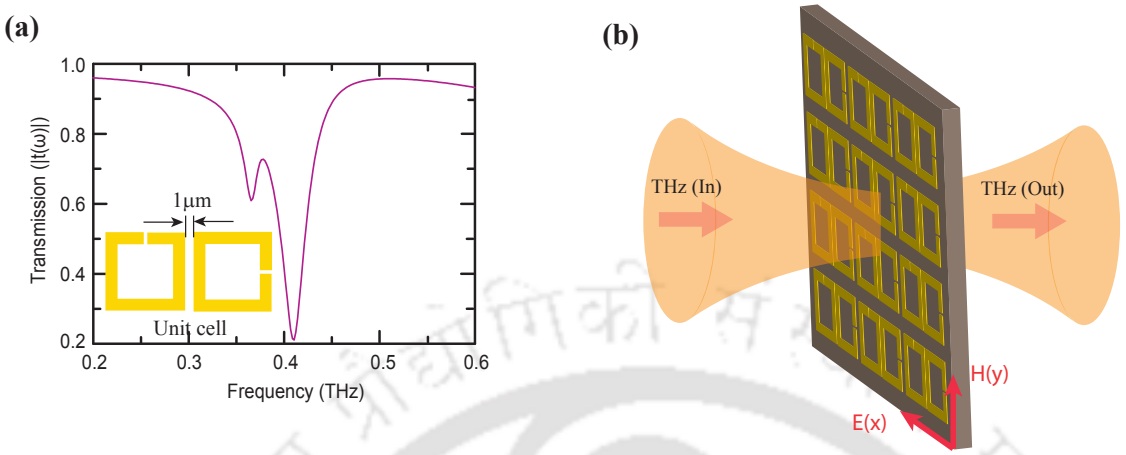

Figure 3.2: (a) Numerically calculated terahertz transmission through a metamaterial geometry having two coupled SRRs as a unit cell. (b) Schematic diagram of 2D metamaterial having two coupled SRRs as a unit cell.

to our configuration and compare results with the numerical observations. Finally the obtained results are summarized into the conclusion section.

3.1 Metamaterial design and simulations

The optimum design of THz metamaterials is very crucial in order to explore the modulations of the resonances. First we have taken single resonator as a unit cell (Fig 3.1 (b)) and studied the transmission through the metamaterial structure (Fig. 3.1 (b)), we observed the single resonance in transmission spectrum (Fig. 3.1 (a)). To study near field inductive coupling, we have taken two orthogonally twisted similar SRRs in a unit cell of metamaterial (Fig. 3.2) and studied terahertz transmission through the metamaterial, transmission shows mode hybridization (Fig. 3.2). Finally, our design comprises of metamaterial unit cell, also known as metamolecule, which consists of two sub-wavelength split ring resonators that interact through their near fields when placed in close proximity. The underlying physical mechanism responsible for frequency tuning in designed metamaterials is examined through the change in resonances under the electrical excitation. We have chosen a typical gallium arsenide (GaAs) substrate for designing the metamaterials which is coated with SRRs of gold metal. Each of the SRR is 40 μm × 40 μm in length and breadth as depicted in the Fig. 3.3 with a gold layer thickness of 200 nm and width 4 μm. The gray regions in the figure represent substrate

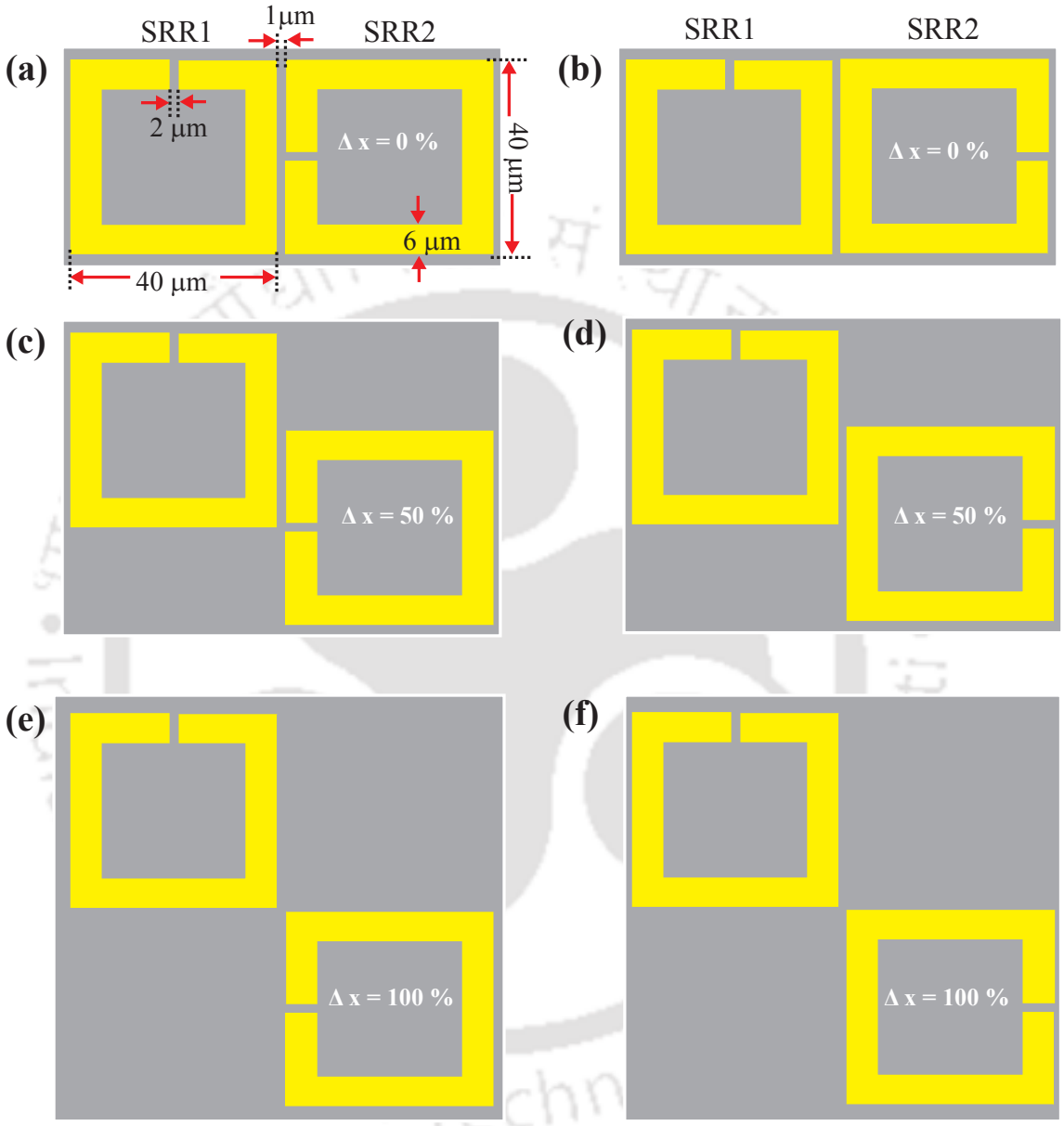

Figure 3.3: Schematic of a unit cell comprising of two SRRs in a coupled THz metamaterials. The gray regions indicate substrate while the yellow regions represent metallic areas. Each of the SRRs has an outer dimension of 40 μm × 40 μm and gap of 2 μm as depicted in the schematic. Δx represents a shift in the position of second resonator with respect to the first in x- direction. The figures (a), (c) and (e) depicts a shift of Δx = 0, 50,100% , when split gap is on the left hand side, while (d), (e) and (f) represents the same shift with gap on right side.

while the yellow regions correspond to the gold film. The split gap of the resonator is 2 μm which is assumed to be constant in our analysis. As mentioned above, in our unit cell we have another SRR of same parameters as the first one, placed at a horizontal separation of 1 μm (Fig. 3.3). In our study, we displace the second resonator w.r.t. the first one in a systematic manner. Δx represents the displacement of the second resonator in the x- direction. We examined the response of terahertz transmission through our metamaterial design for various displacements of Δx = 0, 25, 50, 75 and 100%. We have examined the response of designed metamaterials for the cases, first, when orientation of the split gap of second resonator is facing left side i.e. close to the first resonator, second when the split gap is oriented towards right. Figs. 3. 3 (a), (c), and (e) shows the schematic of the unit cell for first orientation, while Figs. 3.3 (b), (d), and (f) represents the second orientation for the displacements Δx = 0, 50 and 100 %. The terahertz transmission response of these designed metamaterials is examined through the commercially available numerical software, CST Microwave Studio. In the full wave numerical simulations, we used tetrahedral meshing in our geometry with periodic boundary conditions. We used waveguide ports for the source and detector. The results of the THz amplitude transmission for two orientations with different displacements are discussed in the next section. The L.H.S. resonator (SRR1) is directly excited by the incident electric field of linearly polarized terahertz radiation along its split gap in order to excite the fundamental LC resonance. The R.H.S. resonator (SRR2) is excited by the near field inductive coupling from the neighboring resonator. The terahertz transmission ($|t(\omega)|$) of metamaterial sample shows resonance mode hybridization effect due to coupling between fundamental resonances of both resonators with resonances at different frequencies as shown for both the mentioned cases in Figs. 3. 4 (a), (b).

3.2 Results and discussion

First, we examine terahertz transmission through the designed metamaterials for the case when orientation of split gap in second resonator (SRR2) is facing towards left w.r.t. the first resonator (SRR1) (see Fig. 3.3 (a), (c), and (e)). In Fig. 3.4 (a), the results of terahertz transmission ($|t(\omega)|$) for different values of displacements, Δx = 0, 25, 50, 75, 100% are shown. A plane polarized terahertz radiation is incident onto the metamaterials with electric field profile parallel to the split gap of the first SRR (SRR1). This leads to the excitation of the lower frequency LC resonance due to the first resonator and the

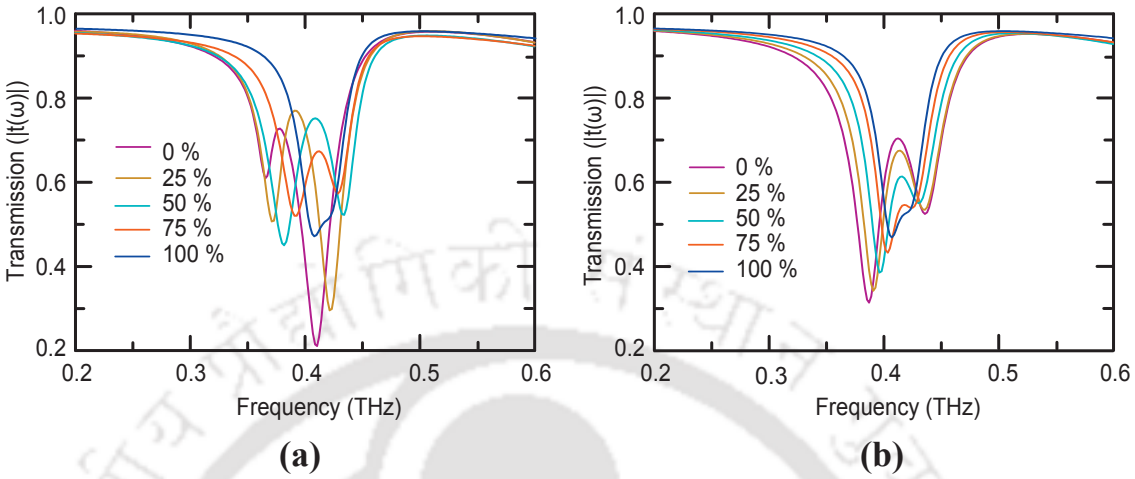

Figure 3.4: Numerically calculated terahertz transmission through a coupled metamaterial geometry. (a) THz transmission through a coupled MM sample when split gap is on the left side and close to the first resonator. Various curves correspond to different displacements of the second resonator with respect to the first i.e. Δx = 0, 25, 50, 75,100%. The results of THz transmission for various positions of the second resonator with split gap on the right side are shown in (b)

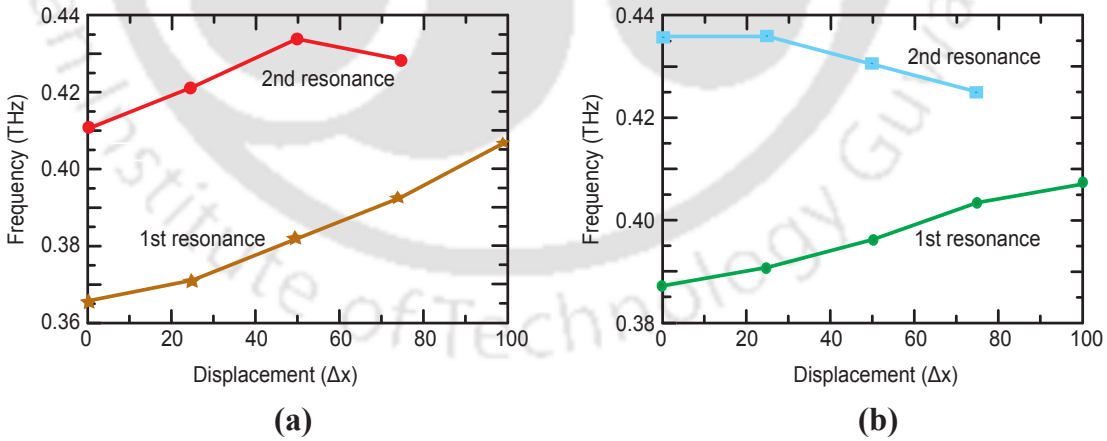

Figure 3.5: Variation of THz frequency with displacement, Δx in the position of 2nd resonator. (a) The change in frequencies of first and second resonances are plotted with displacements, with split gap of the 2nd resonator facing left side close to first resonator. (b) Plot indicates the variation of frequencies with displacements for the same parameters as in (a) however split gap position of the meta resonator is facing right side in this case.

higher frequency dipole resonance due to the presence of 2nd resonator (SRR2). A mutual inductance between the two resonators leads to the excitation of LC resonance in the second resonator therefore leading to coupling between the two resonances. Due to this coupling between the resonators, amplitude transmission indicates a resonance mode hybridization (Fig. 3.4). Normally, a single SRR in a unit cell provides an uncoupled (or intrinsic) resonance at frequency 0.41 THz (Fig. 3.1 (a)).

In Fig. 3.4 (a), we may note that the zero displacement between the resonators i.e. $\Delta x = 0\%$ (Fig. 3.3 (a) case) results in the mode hybridization with two resonance dips appearing at 0.37 THz and 0.41 THz. It is apparent that they exhibit a blue-shift in comparison to the uncoupled resonance of the single SRR. When we shift 2nd resonator in vertically downward direction w.r.t the first, the frequency of 1st resonance gets blue shifted and 2nd resonance also gets blue shifted. For $\Delta x = 50\%$ (Fig.3.3 (c) case), two resonances appear at 0.38 THz (blue shifted) and 0.43 THz (blue shifted). Further displacement in the 2nd resonator results in the merging of two resonances into the single intrinsic resonance. For $\Delta x = 100\%$ (Fig.3.3 (e) case), we get a single resonance at 0.41 THz which basically indicates a transition from coupled resonance state to the uncoupled resonance state. Similarly, we examine the terahertz transmission for the 2nd case i.e. when the split gap of the 2nd resonator is facing on the right side w.r.t. to the first resonator (see Fig. 3.3 (b), (d), and (f)). The results are shown in Fig. 3.4 (b). For the displacement, $\Delta x = 0\%$ (Fig.3.3 (b) case), the transmission indicates a hybridized state with resonances at 0.39 THz (red shifted) and 0.44 THz (blue shifted). Further displacement in x-direction results in red and blue shift of first and second resonances respectively. For the case when, $\Delta x = 50\%$ (Fig.3.3 (d) case), two resonances appear at 0.40 THz (red shifted) and 0.43 THz. Similar to the results of Fig. 3.4 (a), the displacement of, $\Delta x = 100\%$ (Fig.3.3 (f) case) results to the uncoupled state. The two resonances merge into a single resonance. In Fig. 3. 5, we precisely plot a change in frequencies of 1st and 2nd resonances with displacement for both the orientations. These figures also indicate that two resonances merge into a single resonance as the displacement between the resonators increases or in other words when coupling is reduced. We further examined the surface current distributions of the two resonators in strongly coupled, intermediate and uncoupled states in order to make a comprehensive judgment of the results. The results corresponding to the first orientation for the 1st and 2nd resonances are shown in Fig. 3.6. We know that the inductive-capacitive (LC) resonant mode arises from the electric currents oscillating around the full circumference of SRR loop. These

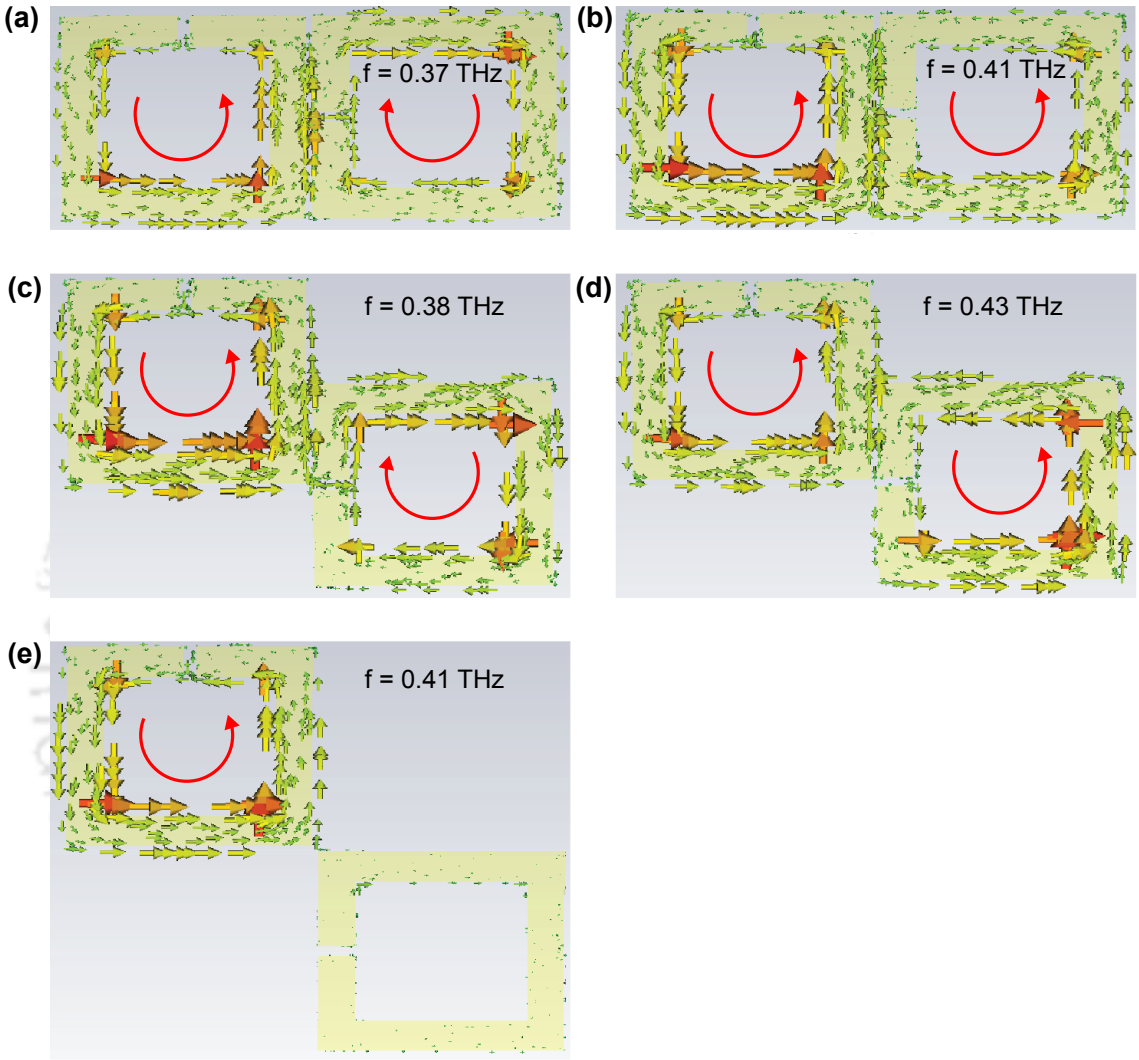

Figure 3.6: Simulated surface current distributions at different resonant frequencies of the coupled resonator when split gap of the 2nd resonator is facing on the left side. The red curves indicate the trend of surface currents through resonators. Figures (a), (c) and (e) correspond to the displacements, Δx = 0, 50, 100% respectively and depicts current distributions for the first resonances in each case. The current distributions for the 2nd resonances (or higher order split resonances) are shown in figures (b) and (d) corresponding to the displacements of Δx = 0, 50%. For Δx =100 %, the coupling is negligibly small.

electric currents are induced by the incident THz beam with electric field along the SRR arm due to asymmetry of the resonator. Once the surface currents set up in both the resonators, they couple to each other through magnetic field lines giving rise to the coupled symmetric and antisymmetric resonant modes.In Fig. 3.6, we see that in the case of displacement $\Delta x = 0\%$, two resonators are strongly coupled with the gap providing the capacitive behavior. The induced surface currents are circular in the two resonators but asymmetrical at the lower frequency, however they are symmetrical at higher resonance frequency. For the case of $\Delta x = 100\%$, we have least coupling (or almost no coupling) between the resonators and surface current does not appear in the 2nd resonator. Similar to Fig. 3.6, we have shown surface current distributions correspond to the 2nd orientation in Fig. 3.7 for both the resonators. In our study, the focus has been to study near field inductive coupling of resonances, however, we believe that there may be a weak capacitive coupling contribution to the transmission response. This can contribute to the mismatching of simulation with the RLC model, where we only consider the inductive coupling effect.

3.3 Semi-analytical approach

In order to understand the behavior of electromagnetically coupled resonances and elucidate our numerical findings, we have employed a semi-analytical model. In this model, lumped-element circuit's model is clubbed with the transmission line model which forms the basis for designing metamaterials of specific properties. The schematic of the transmission-line RLC circuit (TL-RLC) model is shown in Fig. 3.8. It shows two RLC circuits in parallel with impedances Z_1 and Z_2. The impedance Z_1 corresponds to the LC resonance of the first resonator while Z_2 correspond to the LC resonance of second resonator. The capacitive part of the model arises from the split gap of the resonators while loops are responsible for the inductive part. We define M as the inductive coupling parameter which represents the mutual inductance between the two resonances. Note that inductive coupling is dominant in these coupled resonators [90–92]. Therefore we can write the total impedance of the circuit as

$$Z_{tot} = \frac{Z_1 Z_2 + \omega^2 M^2}{Z_1 + Z_2 - j\omega 2M} \tag{3.1}$$

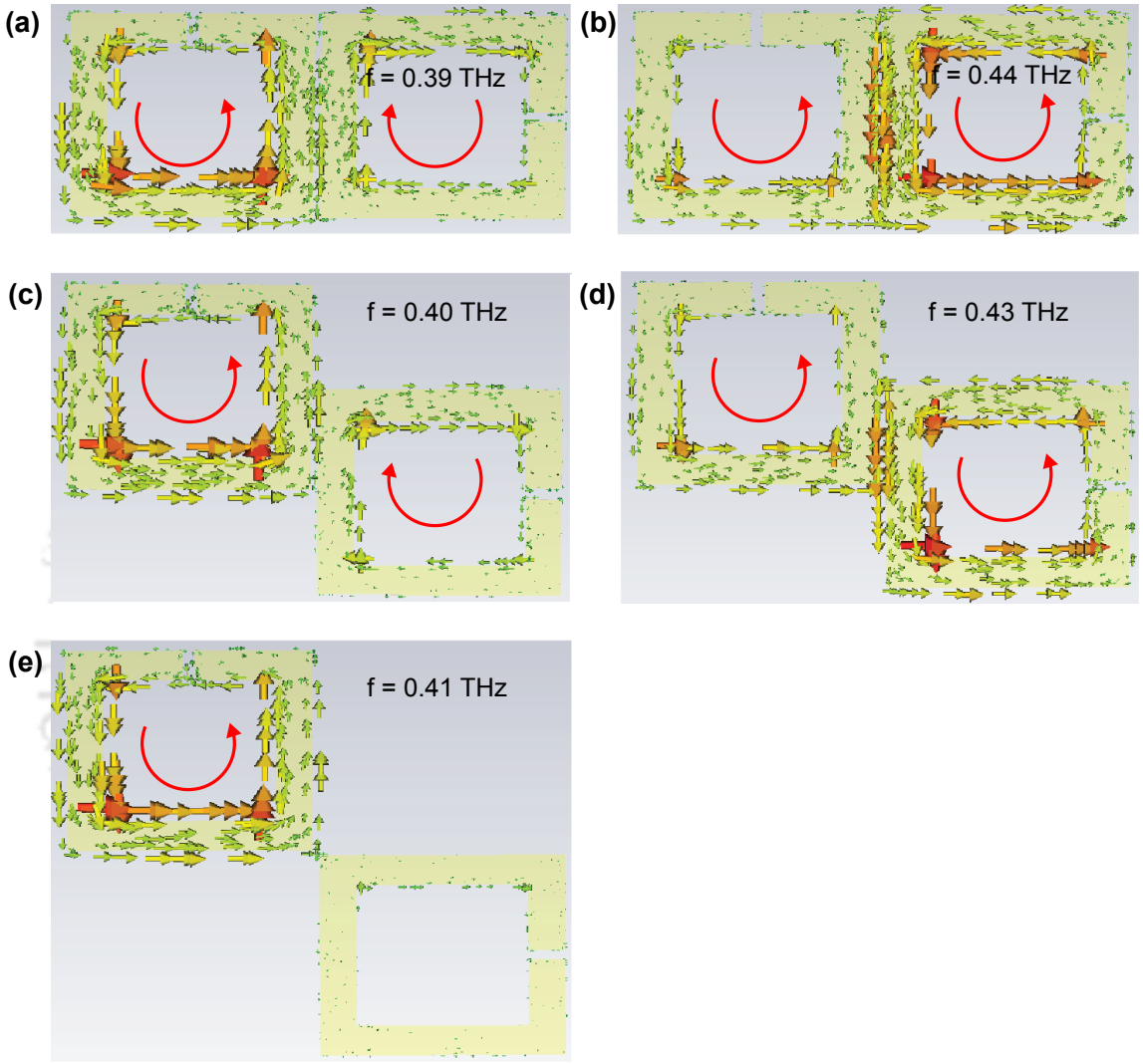

Figure 3.7: Simulated surface current distributions at different resonant frequencies when split gap of 2nd resonator is facing on the right side. Figures (a), (c) and (e) correspond to the displacements of Δx = 0, 50,100% respectively and depicts current distributions for the first resonances. The current distributions for the 2nd resonances corresponding to the displacements of Δx = 0, 50% are shown in figures (b) and (d).The trends of the currents are shown through red curves.

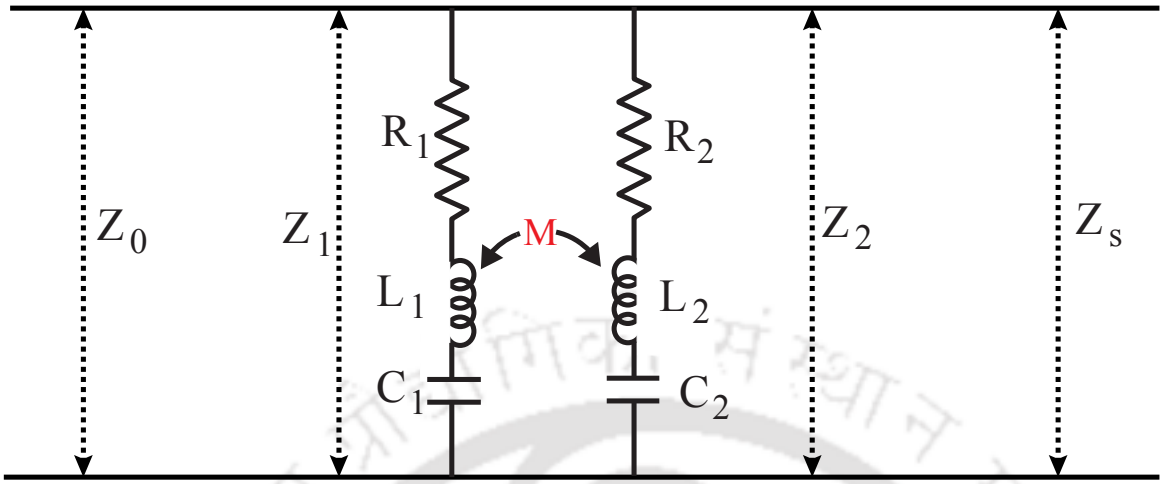

Figure 3.8: Schematic of the transmission-line, RLC (TL-RLC) circuit model. Components R_1, L_1, C_1 represent the resistance, inductance and capacitance describing the LC resonance of the first resonator and R_2, L_2, C_2 describe the 2nd resonator. The parameter M represents the coupling between the resonators. The intrinsic impendences of the transmission lines are depicted by Z_0 and Z_S.

where, M = mutual inductance,

$$Z_1 = R_1 + j\omega L_1 + \frac{1}{j\omega C_1} \tag{3.2}$$

and

$$Z_2 = R_2 + j\omega L_2 + \frac{1}{j\omega C_2}. \tag{3.3}$$

The values of the transmission through the sample, normalized to transmission at a bare GaAs substrate is given by

$$t(\omega) = \frac{Z_{tot}(Z_s + Z_0)}{Z_s(Z_{tot} + Z_0) + (Z_{tot} \times Z_0)} \tag{3.4}$$

where, M = mutual inductance (Coupling parameter), Z_s (Impedance of substrate (GaAs)) = 104.89Ω), Z_0 (Impedance of free space) = 377 Ω). Z_0 and Z_s are used to imitate the wave propagation through free space and substrate. Using Eq. 3.4, we calculate the amplitude transmission for certain specific values of R_1, L_1, C_1, R_2, L_2, C_2 and M (see Table 3.1 and 3.2) for which the model best fit the numerically calculated transmission. Fig. 3.9 represents the transmission results for two different orientations corresponding to various displacements that we examined through numerical simulations earlier. We observed a good agreement in transmission and resonance frequency between the two

R, L, C, and M parameters	**Split gap on L.H.S.**				
	0%	25%	50%	75%	100%
R_1 (Ω)	18	26	63	75	89
L_1 ($\times 10^{-12}$H)	348	348	340	325	321
C_1 ($\times 10^{-15}$F)	0.433	0.414	0.41	0.425	0.44
R_2 (Ω)	112	95	69	82	95
L_2 ($\times 10^{-12}$H)	680	680	650	650	650
C_2 ($\times 10^{-15}$F)	0.279	0.27	0.258	0.246	0.232
M ($\times 10^{-12}$H)	14	12	10	6	3

Table 3.1: The values of R_1,L_1,C_1, R_2, L_2, C_2 and M used in TL-RLC circuit model for split gap on left side case (Fig.3.9(a) case).

R, L, C, and M parameters	**Split gap on R.H.S.**				
	0%	25%	50%	75%	100%
R_1 (Ω)	55	60	69	83	95
L_1 ($\times 10^{-12}$H)	320	320	320	320	320
C_1 ($\times 10^{-15}$F)	0.425	0.422	0.428	0.43	0.435
R_2 (Ω)	44	48	61	78	95
L_2 ($\times 10^{-12}$H)	620	620	620	620	620
C_2 ($\times 10^{-15}$F)	0.268	0.263	0.256	0.249	0.242
M ($\times 10^{-12}$H)	16	13	9	6	4

Table 3.2: The values of R_1,L_1,C_1, R_2, L_2, C_2 and M used in TL-RLC circuit model for split gap on right side case (Fig.3.9(b) case).

simulations. The transmission line model gives us the ability to examine the effect of resonances depending upon the values of R, L, C and M parameters. The coupling parameter is responsible for the coupling between the resonators and affected by the mutual displacements of the resonators. For instance, when displacement between the resonators increases, the value of M decreases (see Table 3.1 and 3.2). Table 3.1 and 3.2 indicates the values of R_1,L_1,C_1, R_2, L_2, C_2 and M that we have used in TL-RLC circuit model for which it validate our numerical observations in both the orientations for several displacements. We have calculated the inductance of SRR from its geometric dimensions. From inductance value, we can estimate capacitence value at the resonance frequency by using $\omega = 1/\sqrt{LC}$. The resistance can be estimated from the quality factor (Q = $\frac{1}{R}\sqrt{\frac{L}{C}}$) of the resonance. The values of R, L, and C from theory as follows R = 51.76Ω, L = 268.63$\times$ 10^{-12} H, and C = 0.562$\times$ 10^{-15} F (see APPENDIX B for detailed calculations).

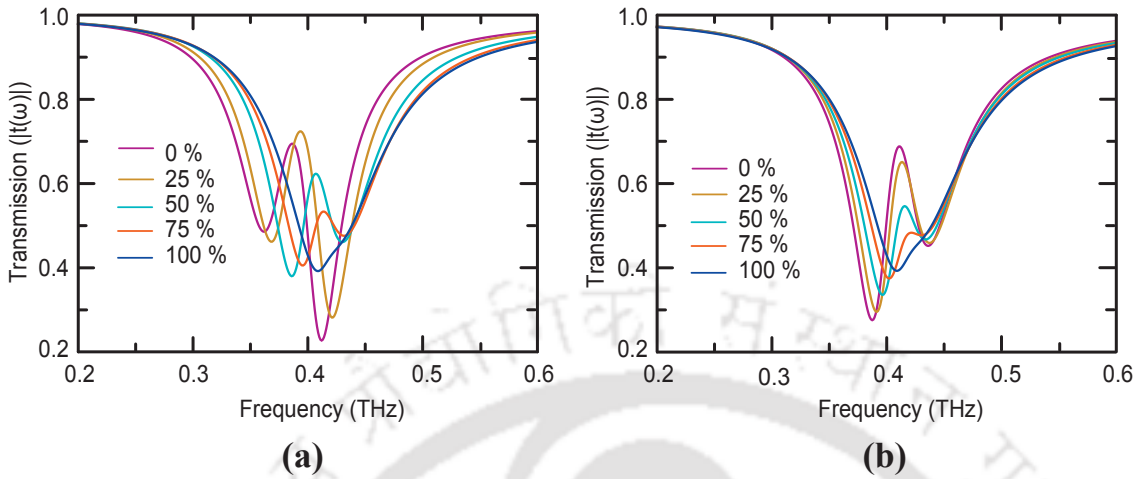

Figure 3.9: Terahertz transmission through the coupled resonators obtained using transmission line RLC circuit model. The results are obtained for various displacements of 2nd resonator w.r.t. 1st. The results predict numerical observations. Figure (a) corresponds to the situation when 2nd resonator of the unit cell is facing left side while in (b) it is on the right side.

3.4 Conclusions

In conclusion, we report the tuning of electromagnetically coupled resonances in planar THz metamaterials by manipulating near field interactions via shifting the position of a resonator with respect to the other within the metamolecule. The metamaterial system presented demonstrates a resonance mode hybridization effect due to the coupling between two resonance modes of a coupled resonators. The transition from coupled to uncoupled state is achieved through various vertical displacements of one of the resonator inside the unit cell. We have shown that with the increasing displacement between the resonators, coupling strength reduces hence two resonances merge into a single resonance (intrinsic resonance). In order to support our numerical observations, we have employed a semi-analytical transmission line model and found that it reasonably reproduces our observations for certain specific values of resistance, capacitance, and inductance of the SRR. Such tuning of metamaterial resonances provides an efficient way to manipulate the electromagnetic waves showing their huge potential of applications in THz region which still suffers from lack of functional devices.

CHAPTER 4

RESONANCE COUPLING IN STACKED TERAHERTZ METAMATERIALS

In previous chapter, we have discussed the near field inductive coupling in edge coupled planar terahertz metamaterials (MMs). In this chapter, we focused on the near field inductive coupling in broadside coupled terahertz metamaterials. The near field interaction between SRRs in adjacent layers results in a strong redistribution of energy in comparison to the single layer MMs giving us an additional advantage. More precisely, the broadside terahertz MMs result in maximum coupling between the resonators. This produces a strong resonance mode hybridization effect. In this context, several studies have been made on the near field inductive coupling in bilayer terahertz metamaterials. Na liu *et al*. in their work, they proposed a new concept in nanophotonics, namely stereo metamaterials, which discussed metamaterials with the same components but distinct spatial arrangements. This stereo metamaterial system comprises of a stack of two equal split-ring resonators in each unit cell with several rotation angles. They theoretically and experimentally examine the meta-compounds and they showed the relationship of electric and magnetic field lines playing a critical role for the optical properties [101]. Shadrivov *et al*. studied experimentally both the transmission and reflection

An article based upon the work reported in this chapter is published in *IEEE Journal of Selected Topics in Quantum Electronics*, vol. **23(4)**, year 2017, pages 1-7; title: "Probing the Near-Field Inductive Coupling in Broadside Coupled Terahertz Metamaterials"; authors SJM Rao, D Kumar, G Kumar, DR Chowdhury.

of microwave radiation from metamaterial super lattices created by layers of periodically arranged wires and split-ring resonators. They measure the dependence of the metamaterial resonance on the spatial period of the superlattice and showed broadening and splitting of resonance for the binary metamaterial structures [102]. Mikhail Lapine *et al*. suggest proficient method for tuning the transmission characteristics of metamaterials through a continuous adjustment of the lattice structure and confirm it experimentally in the microwave range [103]. David A. Powell *et al*. examine the near-field interaction between the resonant sub-wavelength particles of a metamaterial and present a method to calculate the electric and magnetic coupling coefficients. They showed that by altering the relative configuration of the neighboring SRRs it becomes possible to manipulate this near-field coupling, and thus tune the response of metamaterials [104]. Ekmekci *et al*. showed the frequency tunable metamaterial designs at terahertz (THz) frequencies using broadside coupled split-ring resonator (BC-SRR) arrays. They showed that frequency tuning, arising from changes in near-field coupling and is obtained by in-plane displacement of the two SRR layers [105]. Reiten *et al*. Experimentally and numerically studied the interaction between closely spaced bilayer split ring resonators by changing the thickness of separation layer and orientation of SRRs. They have used a thin micron-scale polyimide layer as spacer between two SRRs. They showed that bilayer SRRs resonances strongly depend on interlayer coupling tunable by separation and orientation [76].

Previous investigations on broadside coupled terahertz metamaterials shows resonance frequency shift by changing the thickness of the spacer or displacement of the two SRR layers. In this chapter, we explicitly explore the near field inductive coupling between the coupled meta-resonators in a broadside coupled configuration. This is achieved by displacing the top resonator w.r.t. to the bottom resonator in the horizontal as well as vertical directions (Fig. 4.1). In our proposed metamaterial geometry, the meta-molecule unit cell is comprised of two square shaped split ring resonators aligned in an orthogonally twisted fashion and separated by a layer of polyimide as the spacer. We examine terahertz transmission properties under the mutual displacements of the resonators. The transmission response is observed in the form of mode hybridization because of strong coupling between the resonators. We have studied in depth the transitions between the coupled and uncoupled resonant state as the resonator shifts. In the first section, the designed geometry has been discussed along with the effect of displacement on the coupling of fundamental LC resonances. The numerical results are discussed in

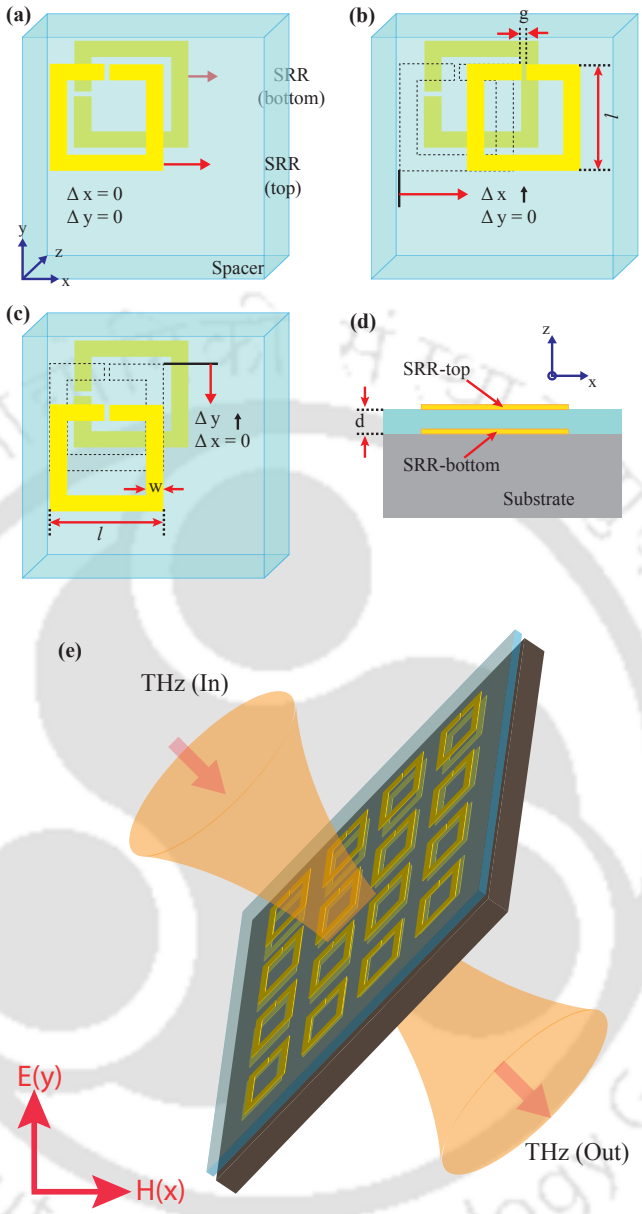

Figure 4.1: Schematic of a single unit cell consisting of two SRRs in the broadside coupled bilayer THz metamaterial. The yellow regions represent the metallic gold areas which are separated by a polyimide spacer shown by the transparent green color. Δx and Δy represent the displacements in x and y directions, respectively. The dotted SRR in figures b and c indicates the initial position of the resonator. Each of resonators has outer dimensions of l × l = 48 μm × 48 μm. The w and g in the schematic stand for the width and split gap of the resonators, respectively. (a) Shows the bilayer metamaterials configuration without any displacement between the resonators. (b) The displacement of the top resonator in the horizontal direction w.r.t. to the bottom resonator while maintaining Δy = 0. The red arrow indicates the direction of displacement. (c) Vertically displaced top resonator w.r.t. the bottom resonator i.e. Δy is finite while Δx = 0. (d) Side view of the bilayer metamaterial with spacer thickness 'd' = 4 μm when top and bottom resonators are aligned. (e) Schematic diagram of broadside coupled terahertz metamaterial.

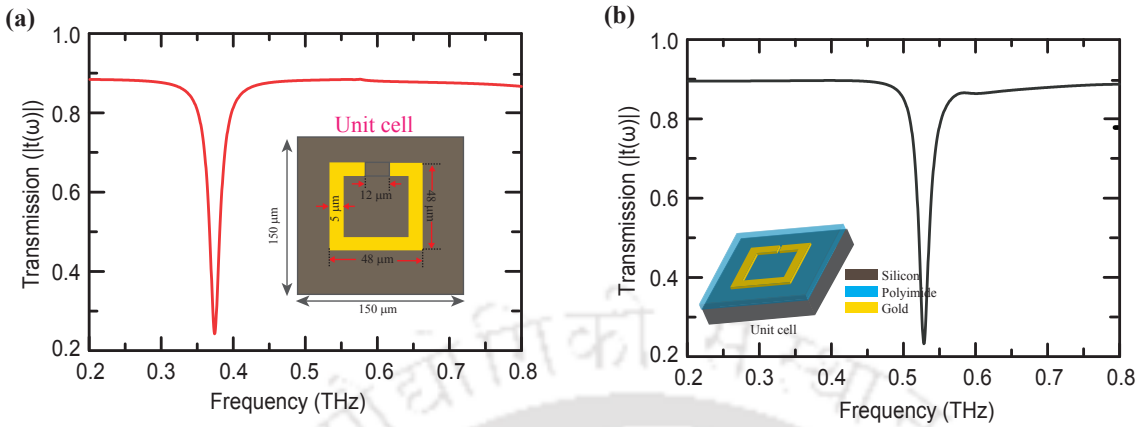

Figure 4.2: (a) Numerically calculated terahertz transmission through a metamaterial geometry having only bottom SRR as a unit cell. (b) Numerically calculated terahertz transmission through a metamaterial geometry having only top SRR as a unit cell.

detail in the next section. Further, we discuss RLC circuit model, which we designed in conjunction with the proposed bilayer metamaterials configuration. Finally, the results are summarized in the conclusion section.

4.1 Bilayer metamaterial configuration and numerical simulation details

The choice of the design of terahertz (THz) metamaterials is crucial in accomplishing the tunable response of the resonances. In our proposed metamaterial configuration, metamolecule unit cell is comprised of two split ring resonators separated by a polymer spacer of thickness d = 4 μm. We assumed the polymer to be polyimide which is transparent to terahertz and exhibit no loss. A schematic of the proposed configuration is shown in Fig. 4.1. We have assumed silicon of thickness 25 μm as the substrate with other dimensions as length× breadth = 150 μm × 150 μm. The unit cell is chosen to be much bigger in size compared to the metamolecule pair in order to avoid any coupling between the neighboring unit cells of the bilayer metamaterial system. In this metamolecule unit, both the SRRs i.e. top and bottom as depicted in the figure are 48 μm ×48 μm in length and breadth with a gold layer thickness of 200 nm. The capacitive gap and line width of the resonators are assumed to be 'g' = 12 μm and 'w' = 5 μm, respectively. The above mentioned parameters are considered to be constant throughout the analysis. It is

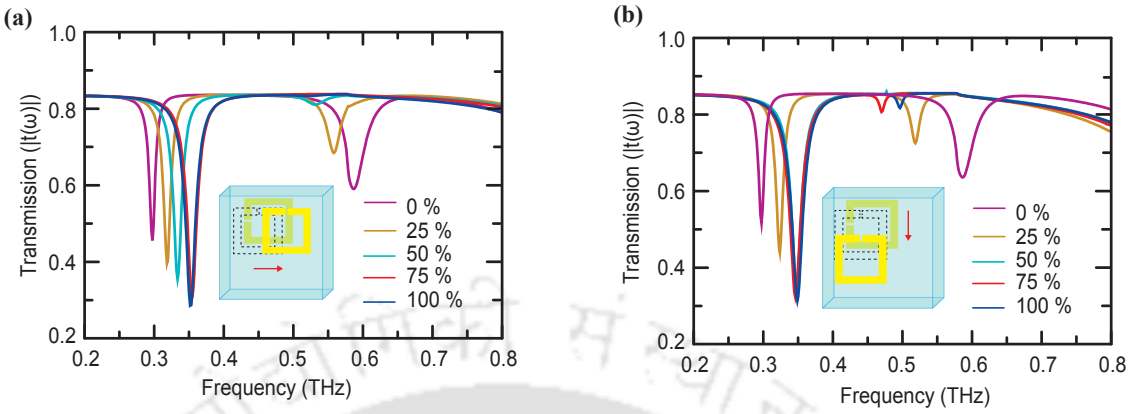

Figure 4.3: Numerically calculated terahertz transmission through the coupled metamolecule as studied in this work. (a) Terahertz transmission for various horizontal displacements i.e. Δx = 0, 25, 50, 75, 100% of the top resonator w.r.t. the bottom resonator. The results of the terahertz transmission for different vertical displacements i.e. Δy = 0, 25, 50, 75, 100% are shown in figure (b). The inset in both the plots represents a SRR unit cell along with the direction of displacements of the resonators.

important to highlight that the top and bottom split ring resonators of the metamolecule sample are orthogonally twisted with respect to each other. In our study, we fix the bottom resonator and displace top resonator w.r.t. the bottom, both in horizontal and vertical directions, see Fig. 4.1. The horizontal and vertical displacements are symbolized by Δx and Δy in x and y directions, respectively. Fig. 4.1 (a) represents the bilayer geometrical configuration when there is no displacement between the resonators, whereas Fig. 4.1 (b) and 4.1 (c) represent horizontally and vertically displaced top resonator w.r.t. the bottom one. Fig. 4.1 (d) depicts the side view of the metamolecule unit cell. We have examined the response of THz transmission through the proposed design for various displacement values ranging from 0% to 100% in the horizontal and vertical directions.

For our numerical study, we have used commercial available numerical software, named CST Microwave Studio and used tetrahedral meshing in order to simulate the geometry. The boundary conditions are assumed to be periodic in the full wave numerical simulations. We have used waveguide ports as the source and detector. Before going to proposed bilayer structure, firstly we have done simulation separately for bottom and top resonators and results are shown in Fig. 4.2. In our study of the terahertz transmission through the broadside coupled metamaterials, the polarization of the incident THz beam is assumed to be along the split gap of the bottom resonator in order to excite the fundamental LC resonance. The top resonator is excited through the near field inductive

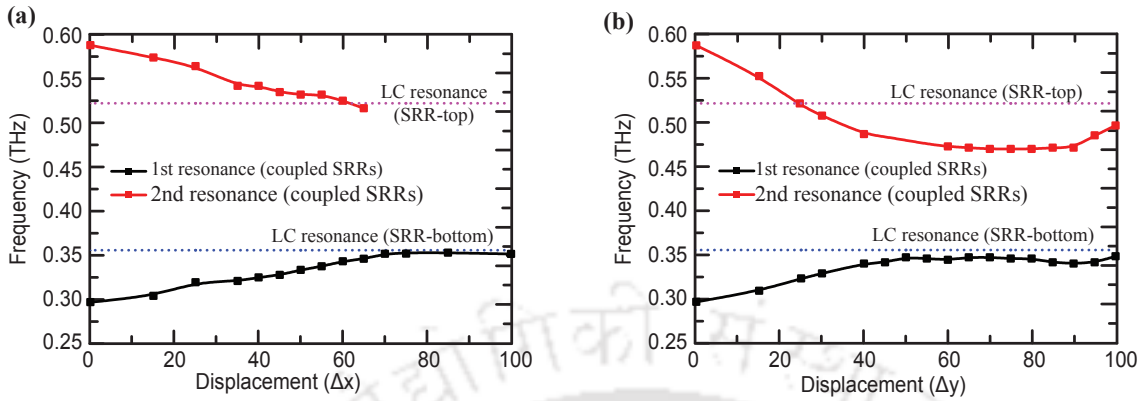

Figure 4.4: Variation of THz frequency corresponding to the first and second resonances exhibited by the bilayer metamaterial sample versus displacement between the resonators. (a) Shows the variation of first resonance (solid black traces) and second resonance (solid red traces) when the top resonator is horizontally displaced w.r.t. the bottom resonator. The variation of 1st and 2nd resonances w.r.t. the vertical displacement (Δy) is shown in (b). The traces in violet and blue dots represent intrinsic resonances of the two uncoupled resonators i.e. SRR (top) and SRR (bottom), respectively.

coupling of the bottom resonator. The resonance mode hybridization result from the coupling of bottom split ring resonators with the top resonators through a combination of magnetic and electric flux because of close proximity of the resonators [95]. In our case, the top layer of the SRRs is surrounded by the air and polyimide layer of electric permittivity's i.e. ϵ = 1 and ϵ=3.5, respectively, however, the bottom SRRs by polyimide and silicon (ϵ = 11.9), and hence they experience different dielectric ambience. Because of the inhomogeneous bilayer structure, the LC resonance from the top resonator gets modified compared to the bottom LC resonance. The terahertz transmission (|t(ω)|) shows resonance mode hybridization effect (Fig. 4.3) due to the coupling between fundamental resonances of top and bottom resonators. The results of the terahertz transmission through the inductively coupled THz metamaterial systems are discussed elaborately in the next section.

4.2 Results and discussions

In order to examine the terahertz transmission properties of the broadside coupled metamaterial resonances, we displace top SRR w.r.t. the bottom resonator in both the x- and y- directions. The results for the displacements of 0,25,50,75,100% are shown

in Fig. 4.3. In Fig. 4.3 (a), we plot the terahertz transmission (|t(ω)|) versus frequency for the horizontal displacement of the top resonator. We notice that when there is no displacement i.e.Δx = 0%, we get two resonances at 0.30 THz and 0.59 THz. The first resonance indicates a red shift while the 2nd resonance shows a blue shift w.r.t. the intrinsic resonances of the bottom and top resonators when they are in the uncoupled state. The uncoupled resonances from the top and bottom resonators are observed at 0.52 THz and 0.36 THz, respectively (Fig. 4.1). They are more specifically discussed in Fig. 4.4. When we increase the horizontal displacements i.e. for Δx = 25 & 50%, a similar trend in the shift of resonances is observed. With further increase in the displacements i.e.Δx = 75 & 100%, the transmission spectrum shows a single resonance dip at 0.35 THz which is close to the resonant frequency of bottom resonator in the uncoupled state. Similarly, we examined the terahertz amplitude transmission for the case when top SRR is displaced vertically downward w.r.t. the bottom resonator. The results are shown in Fig. 4.3 (b). For Δy = 0% displacement, the 1st and 2nd resonances appears at 0.30 THz and 0.59 THz respectively as we discussed above. As the displacement is increased i.e. for Δy = 25%, the 1st and 2nd resonances shifts to 0.32 THz and 0.52 THz respectively. This indicates a blue shift in the 1st resonance and a red shift in the 2nd resonance.As we increased the displacements to Δy = 75%, and beyond the 2nd second resonance goes through further red shifting.

In order to comprehensively understand the coupled and uncoupled behavior of the resonances, in Fig. 4.4 we plot the resonant frequency of the 1st and 2nd resonances versus displacements of the top resonator w.r.t. the bottom one. In Fig. 4.4 (a), the resonant frequency is plotted versus horizontal displacement Δx. The solid black and red traces correspond to the 1st and 2nd resonances of the transmission amplitude. The dotted violet and blue lines represent uncoupled or intrinsic resonances of the top and bottom resonators, respectively. When there is no displacement, the transmission through bilayer metamaterials exhibit coupled resonant behavior, and we observe the 1st and 2nd resonances as red and blue shifted w.r.t. the uncoupled resonances of the respective resonators. However, as we increase the displacement, the red and black curves approached the dotted lines signifying a transition from the coupled to the uncoupled state. In vertical displacements for which the results are shown in Fig. 4.4 (b), we observe a similar behavior of the 1st and 2nd resonances with the displacement. Interestingly with displacement Δy > 50% the higher frequency resonance or the top resonance shifts beyond the intrinsic resonance of the top resonator.

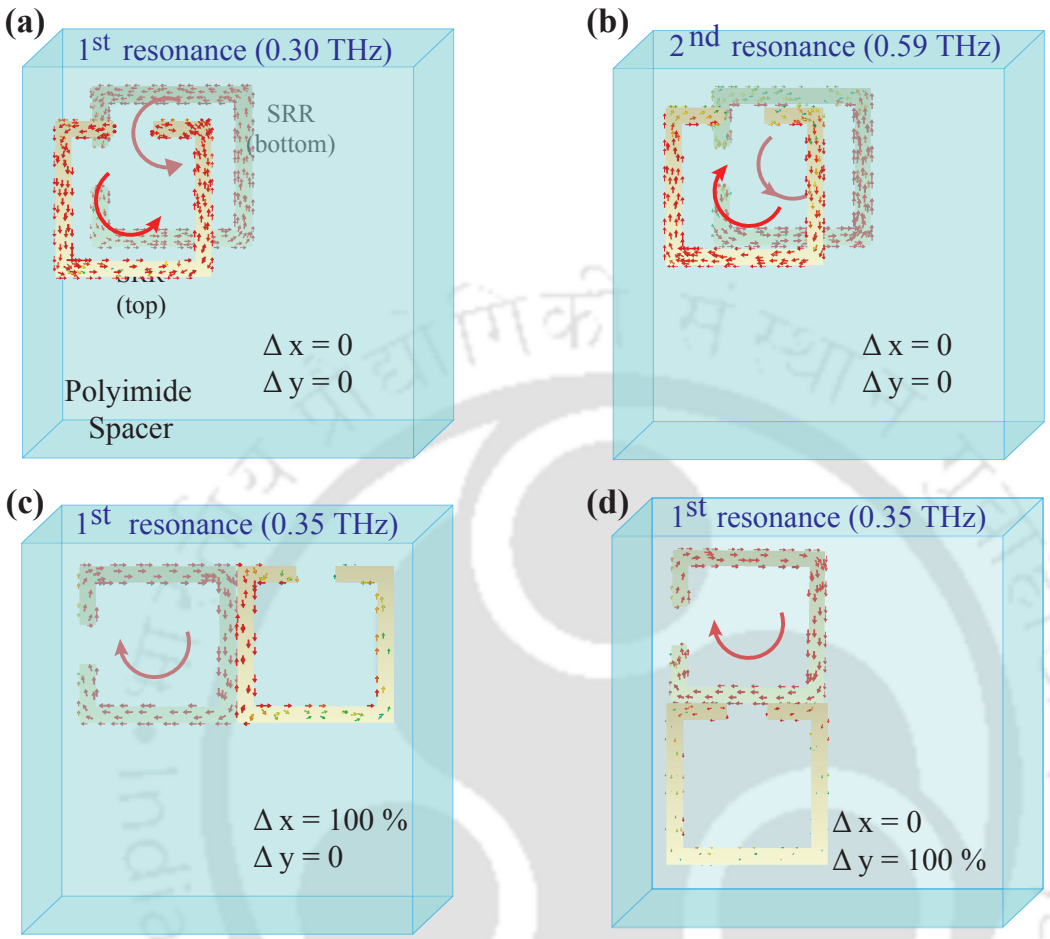

Figure 4.5: Simulated surface current distributions for different displacements between the resonators. (a) and (b) show current distributions for the 1st and 2nd resonances when Δx = Δy = 0%. (c) and (d) represent current distribution for Δx = 100%and Δy = 100% respectively at the 1st resonance frequency. The red arrows indicate the direction of currents in the resonators.

In order to further analyze the displacement dependent coupling between the resonators, we examined the surface current distributions of the top and bottom resonators in the coupled and the uncoupled states. The results are shown in Fig. 4.5. The surface current distributions for the horizontal displacements of Δx = 0% and 100%, keeping Δy = 0 %, are depicted in Fig. 4.5 (a)-(c). In the case of Δx = Δy = 0%, the resonators are strongly coupled and we clearly notice a hybridized state. The surface currents in both the resonators are in anticlockwise directions (in phase) at first resonance of 0.30 THz (Fig. 4.5 (a)), however at second resonance frequency i.e. 0.59 THz, the current distributions are out of phase meaning that the currents directions are in clockwise and

anticlockwise directions in the top and bottom resonators respectively (Fig. 4.5 (b)). The current distribution shown in Fig. 4.5 (c) corresponds to 100% displacement along the x axis, where we see only the 1st resonance. At this resonance we observe a strong circular current in the bottom resonator. Fig. 4.5 (d) shows the current distributions for the observed resonance for the displacement corresponding to Δx = 0,Δy = 100%. In this case at resonance we see strong circular current in the bottom resonator however there is almost no current in the top resonator indicating almost no or very weak coupling in between the resonators. The red arrows in all the distributions indicate the direction of currents in the resonators. Ideally the mode hybridization model was explained on the assumption of the same energy state by Hallas group [106]. But mode hybridization can further enhance the already separated resonance positions provided the two resonators can couple strongly enough. In this context we would like to provide the following reference [76] where such a situation was encountered. The strongest signature of hybridization is the anti-parallel and parallel induced current in both the resonator at the resonance frequencies[See Fig. 4.5.].

4.3 Semi-analytical transmission line model

In order to understand the resonant behavior of the transmission properties through broadside coupled terahertz metamaterials and explain transitions between the coupled and uncoupled states of the resonances, we used a semi-analytical transmission line (TL)-RLC model. This model has the ability to give us insight of the resonant transmission behavior through the proposed THz metamaterials system. In this semi-analytical approach, a single SRR is modeled with an equivalent RLC circuit which exhibits resonance at a specific frequency depending upon the shape and size of the split ring resonator. For our case we assumed two RLC circuits with resistances, inductances and capacitances as R_1, L_1, C_1 and R_2, L_2, C_2 corresponding to the top and bottom resonators, respectively. In order to justify the results of our numerical findings, we calculated terahertz transmission results through the TL-RLC circuit model under different values of coupling between the resonators (see Table 4.1 and 4.2). The schematic of the TL-RLC circuit is shown in Fig. 4.6. The circuit shows a parallel combination of LC impedance Z_1 and second order resonance impedance Z_2 [90–92]. In order to understand the effect of the second order resonance of the bottom resonator on the fundamental LC resonance of the top resonator, we introduce a coupling parameter 'M' between the SRRs. The overall

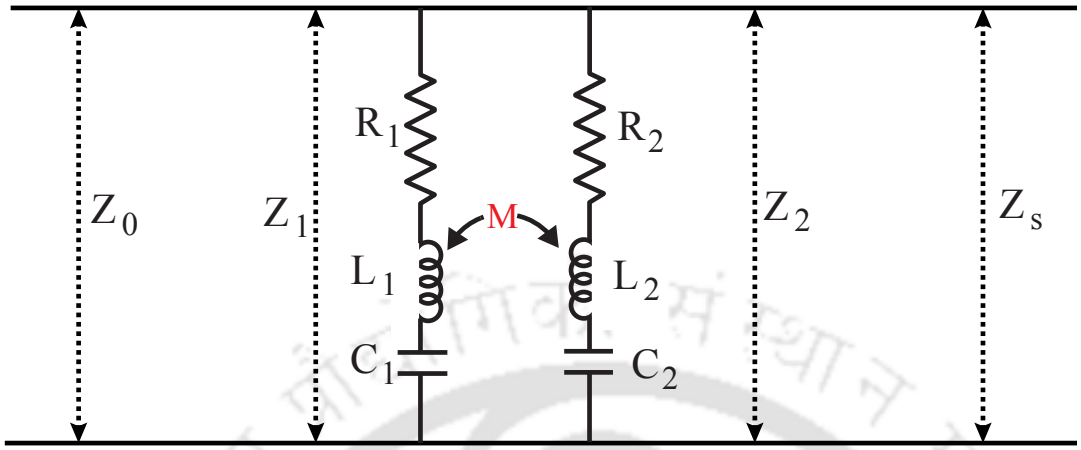

Figure 4.6: Schematic of the transmission line RLC circuit model. The electrical components R_1, L_1, C_1 represent the resistance, inductance, capacitance describing the fundamental LC resonance of the top meta-resonator and R_2, L_2, C_2 describe the resonance for the second bottom resonator. Z_1 and Z_2 represent the LC impedance and second order resonance impedance respectively. The characteristic impedances of transmission lines are represented by Z_0 and Z_s. The parameter M is responsible for the coupling between the resonators.

impedance of the circuit can be written as

$$Z_{tot} = \frac{Z_1 Z_2 + \omega^2 M^2}{Z_1 + Z_2 - j\omega 2M} \tag{4.1}$$

where, M = mutual inductance,

$$Z_1 = R_1 + j\omega L_1 + \frac{1}{j\omega C_1} \tag{4.2}$$

and

$$Z_2 = R_2 + j\omega L_2 + \frac{1}{j\omega C_2}. \tag{4.3}$$

The values of the transmission through the sample, normalized to transmission at a bare Si substrate is given by

$$t(\omega) = \frac{Z_{tot}(Z_s + Z_0)}{Z_s(Z_{tot} + Z_0) + (Z_{tot} \times Z_0)} \tag{4.4}$$

where, Z_s (impedance of Si substrate) = 109.38 Ω and Z_0((Impedance of free space) = 377 Ω. Z_0 and $Z_s$are used to imitate the TEM wave propagation through free space and substrate. We calculate, transmission using Eq. (4.4) by adjusting the model parameters

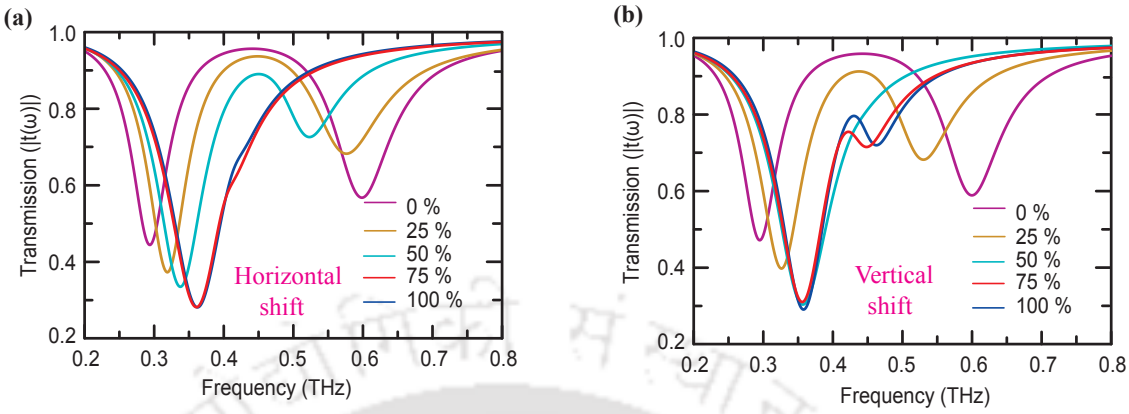

Figure 4.7: Terahertz transmission through the coupled resonators in bilayer THz metamaterials obtained from transmission line RLC circuit model for various displacements of top split ring resonator w.r.t. bottom SRR. The results affirm numerical observations. (a) Terahertz transmission for various displacements of the top resonator in the horizontal direction. For vertical shift of the top resonator w.r.t. the bottom, the transmission results are shown in (b).

R, L, C, and M parameters	**Horizontal shift (Δx)**				
	0%	25%	50%	75%	100%
R_1 (Ω)	95	72	64	58	58
L_1 ($\times 10^{-12}$H)	498	420	340	340	330
C_1 ($\times 10^{-15}$F)	0.57	0.57	0.62	0.52	0.555
R_2 (Ω)	62	98	98	88	88
L_2 ($\times 10^{-12}$H)	200	210	250	300	300
C_2 ($\times 10^{-15}$F)	0.399	0.41	0.42	0.53	0.54
M ($\times 10^{-12}$H)	90	78	69	45	35

Table 4.1: The values of $R_1, L_1, C_1, R_2, L_2, C_2$ and M used in TL-RLC circuit model for horizontal shift (Δx) case (Fig.4.7(a) case).

R, L, C, and M parameters	**Vertical shift (Δy)**				
	0%	25%	50%	75%	100%
R_1 (Ω)	95	80	53	45	50
L_1 ($\times 10^{-12}$H)	498	420	330	325	324
C_1 ($\times 10^{-15}$F)	0.57	0.538	0.52	0.58	0.59
R_2 (Ω)	62	78	80	89	99
L_2 ($\times 10^{-12}$H)	200	210	300	282	285
C_2 ($\times 10^{-15}$F)	0.399	0.499	0.55	0.47	0.49
M ($\times 10^{-12}$H)	90	80	60	50	45

Table 4.2: The values of $R_1, L_1, C_1, R_2, L_2, C_2$ and M used in TL-RLC circuit model for vertical shift (Δy) case (Fig.4.7(b) case).

$R_1, L_1, C_1, R_2, L_2, C_2$ and M until the model transmission fits the measured data (see the Table 4.1 and 4.2). Using the simulation and modelling, we can analyze on how the R, L, C and M parameters affect the resonance shapes. The coupling between two resonators affects the shape of the graphs by virtue of mutual inductance (M) which is affected by the mutual displacements between the two meta-resonators. The results of transmission through RLC-circuit model for horizontal displacements are shown in Fig. 4.7 (a). The corresponding values of coupling parameter 'M' and R_1, L_1, C_1, R_2, L_2, C_2 are given in table-4.1. We observe a decrease in value of M with an increase in horizontal displacement. The calculated transmission is found in good agreement with the numerical simulations. In Fig. 4.7 (b), the results of terahertz transmission from the TL-RLC circuit model for the vertical displacements are also shown. The corresponding values of coupling parameter 'M' and R_1, L_1, C_1, R_2, L_2, C_2 are given in table-4.2. The values of R, L, and C from theory as follows R = 61.49Ω, L = 344.027× 10^{-12} H, and C = 0.51× 10^{-15} F (see APPENDIX C for detailed calculations). In this problem, polyimide layer thickness is very small that's why we have not consider in transmission line model. The thickness of polyimide layer is of the order of three hundredth part at our spectrum of interest. We have calculated the Fresnel coefficients for two layers (Air (n=1) and Silicon (n=3.4496)) case and three layers (Air (n=1), Polyimide (n= 1.8708), and Silicon (n=3.4496)) case. We got Reflectivity(R) = 0.3031 and Transmissivity(T) = 0.6969 for two layers case and we got Reflectivity(R) = 0.3017 and Transmissivity(T) = 0.6984 for three layers case. So we believe it is justified to ignore the contribution of polyimide layer. In our study, the focus has been to study near field inductive coupling of resonances, however, we believe that there may be a weak capacitive coupling contribution to the transmission response. This can contribute to the mismatching of simulation with the RLC model, where we only consider inductive coupling effect.

4.4 Conclusions

In summary, we have examined the ability to tune the inductive coupling resonances in closely spaced inhomogeneous broadside coupled THz metamaterials. This has been achieved by manipulating the near field interactions via shifting the top resonator with respect to the bottom resonator both in horizontal as well as vertical directions within the metamolecule. In case of zero displacement, we observe a resonance mode hybridization effect due to the coupling between two resonance modes, indicating a strong near field

coupled metamaterials system. The 1st and 2nd resonances are observed to be red and blue shifted compared to the uncoupled resonance of the bottom and top resonators. In case of horizontal displacement of the top resonator, the coupling between the resonators decreases and gradually uncoupled state is reached when the resonant frequencies correspond to the uncoupled resonance response of the resonators. In vertical displacements, we see similar tendency in resonance shift however when coupling reduces, the higher order resonance mode is red shifted beyond the intrinsic resonance. In order to validate and support our observations, we used a semi-analytical transmission line model and found that for certain specific values of resistance, capacitance and inductance of the SRR, it reproduces our numerical findings for the amplitude transmission. We have further noticed that the inductive coupling parameter monotonically reduces its strengths as the displacement between the resonators increases. The tuning of inductively coupled broadside metamaterial resonances has great potential in manipulating and controlling electromagnetic waves which can ultimately result in novel applications at THz such as designing antennas, modulators, switches etc.

CHAPTER 5

MODE HYBRIDIZATION IN CAPACITIVE COUPLED TERAHERTZ METAMATERIALS

In this chapter, we have focused on near field manipulations between nearest neighbor SRRs. Metamaterials in near field coupled configurations can consist of more than one SRR (meta-atoms) in a unit cell and intelligently manipulating the near field coupling between these resonators, can have significant impact on the metamaterials responses. The control in near field coupling is crucial in design and fabrication of terahertz photonic components viz. modulators, filters, polarization rotation etc. In the earlier chapters, we have investigated near filed inductive coupling in edge to edge coupled terahertz metamaterial and broadside coupled terahertz metamaterial. Here, we focused mainly on the capacitive near field coupling in a terahertz metamaterial. Although, the investigations on near field coupling in terahertz metamaterials have led to many interesting physics and engineering, but actualization of terahertz devices using such coupling mechanisms require other challenges to be addressed. This includes engineering the near field capacitive coupling to excite sharp low bandwidth resonance which has not been discussed earlier. In this context, gap to gap near field capacitive coupling between adjacent SRRs can result in either blue shift or red shift of the fun-

An article based upon the work reported in this chapter is published in *Scientific Reports*, vol. **8(1)**, year 2018, pages 16773; title: "Modulating Fundamental Resonance in Capacitive Coupled Asymmetric Terahertz Metamaterials"; authors S. Jagan Mohan Rao, Yogesh Kumar Srivastava, Gagan Kumar and Dibakar Roy Chowdhury.

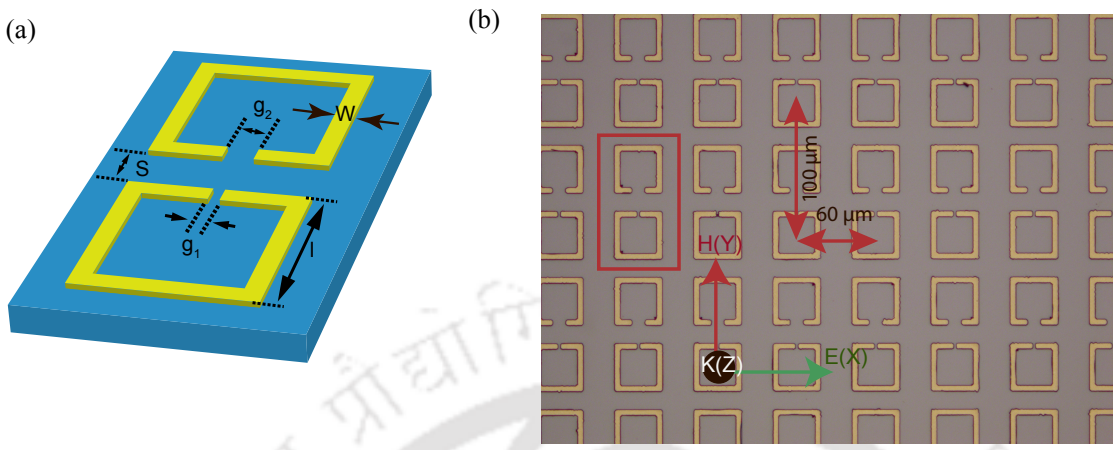

Figure 5.1: (a) Schematic of a unit cell comprising of two SRRs in a coupled THz metamaterials. The blue regions indicate substrate while the yellow regions represent metallic areas. Each of the SRRs has an outer dimension of 36 μm ×36 μm and gap (g_1) of bottom SRR is 2 μm, gap of top SRR is g_2 (g_2 = 2, 6, 10. . . .28 μm), width (w) of SRR is 4 μm. 'S' represents a separation between two SRRs in y-direction(S= 2, 6, 10 and 14 μm). (b) Optical microscope image of fabricated sample.

damental resonance, based upon the near field coupling through the split gap of SRRs [79]. This provides an extra degree of freedom to manipulate and control the phase and amplitude of the terahertz wave propagation. Further, near field interactions between the adjacent SRRs results in a strong redistribution of energy in comparison to the single SRR giving an additional degree of freedom in designing metamaterials. In this contest Chowdhury *et al*. showed the nature of coupling between laterally paired split ring resonators in a unit cell of terahertz metamaterial. Their results specify that tuning of the electric and magnetic coupling parameters may be achieved not by varying the orientation or density of SRRs, but by a design change at the unit cell level [79]. In another study, they experimentally examine a strong effect of Coulomb interaction in strongly coupled terahertz metamaterials where the SRR compounds in a unit cell are coupled through their near fields across the resonator split gaps. In another study, multiple high-Q-factor resonances and modulation depth of two resonances demonstrated by using, two rectangular SRRs in a unit cell of terahertz metamaterial. These two SRRs are mirror-arranged to construct mirror-symmetric-broken metamaterial. In this mirrored system, they showed that capacitive coupling between the two SRRs is dominated [107].

In this chapter, we experimentally and numerically study the asymmetric gap to gap near field capacitive coupling between a pair of SRRs in a coupled unit cell of

terahertz metamaterial. This is achieved by changing the gap size of one resonator with respect to the other resonator in a unit cell of THz metamaterial. Further, we have examined a change in coupling from strong near field regime to weak near field regime by changing the inter resonator separations in the unit cell. In next section, we have calculated Q factors for each resonance mode. Because of the interactions between the asymmetric split gaps, the asymmetric and symmetric coupled resonance modes are excited which results in low bandwidth and frequency tunable resonance modes. The results are summarized in the conclusion section.

5.1 Metamaterial design and experimental details

The design of terahertz (THz) metamaterials is crucial in accomplishing the desired electromagnetic response. In our proposed metamaterial configuration, metamolecule unit cell is comprised of two split ring resonators with gaps facing each other. A schematic of the proposed configuration is shown in Fig. 5.1 (a). We have assumed silicon as the substrate. The unit cell is chosen to be sufficiently bigger in size (P_x =60 μm and P_y=100 μm) compared to the metamolecule or SRR pair in order to avoid any undesired near field couplings between the neighboring unit cells. In such a metamolecule design, both the SRRs i.e. top and bottom as depicted in the figure are 36 μm × 36 μm in length and breadth with an aluminum layer of thickness of 200 nm deposited at the top side. The capacitive gap and line width of the bottom resonators are assumed to be 'g_1' = 2 μm and 'w' = 4 μm, respectively. The above mentioned parameters remain constant throughout the analysis for the bottom resonator. However, in case of top resonator, the line width is same i.e. 'w' = 4 μm, but the top capacitive gap (g_2) is varied from 2 μm to 28 μm. The inter resonator separation (S) is varied from 2 μm to 14 μm in the step size of 4 μm. For the fabrication of samples, we used conventional photo-lithography technique in the clean room environment. The samples were fabricated on a 500 μm thick high resistivity (> 5000 ohm-cm) silicon substrate. Followed by photo-lithography, a 200 nm thick aluminum was deposited by using a thermal evaporator, after which a lift-off process enabled the formation of the SRR array. Optical microscope images of the fabricated samples are shown in Fig. 5.1 (b) with the detailed geometric dimensions.

The measurements were carried out using a typical 8f confocal terahertz time-domain spectroscopy (THz-TDS) system consisting of a photo-conductive antenna based transmitter and receiver. The metallic antenna on GaAs chip is dc biased at 70 V and excited

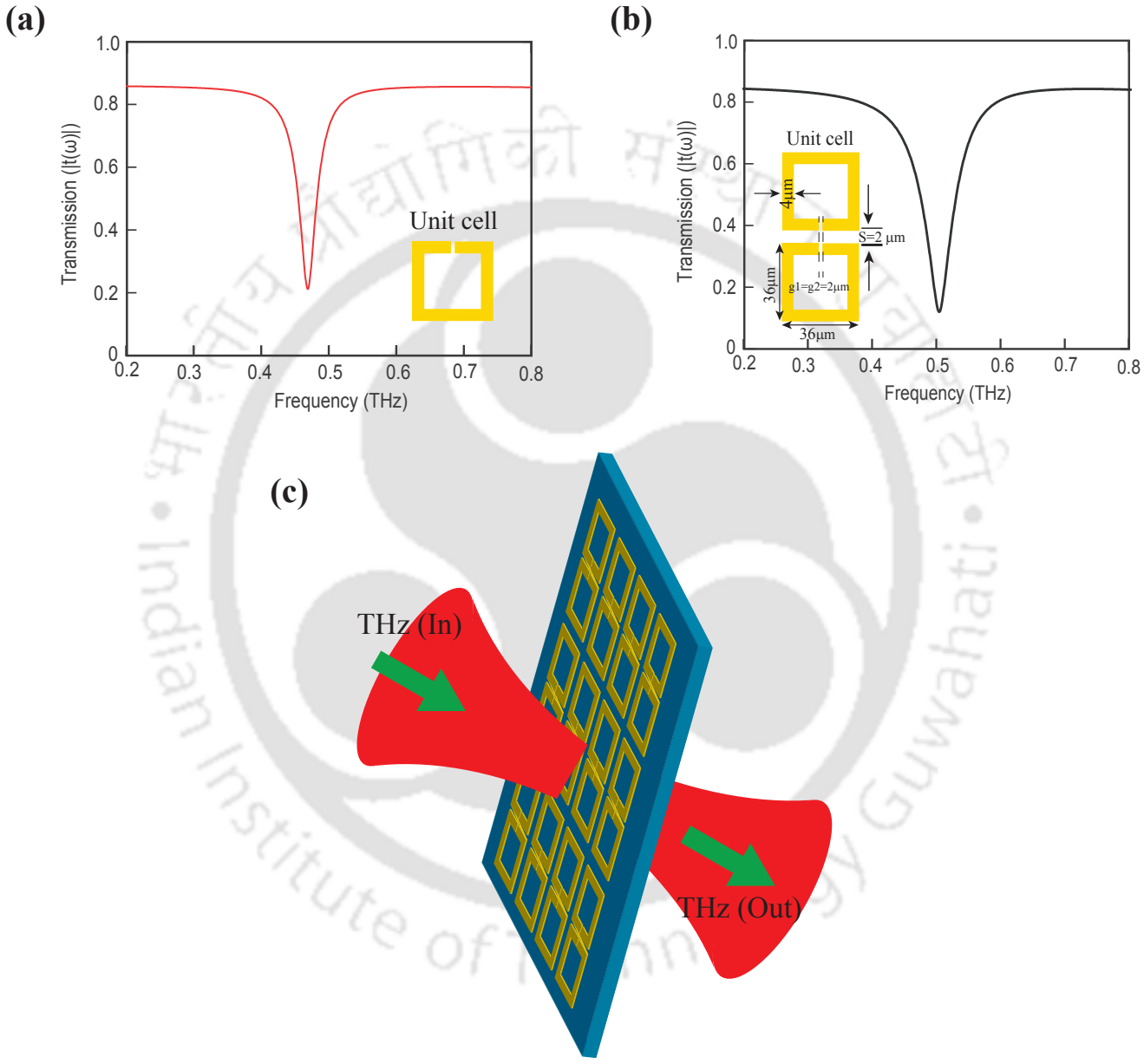

Figure 5.2: (a) Simulation results for single SRR as unit cell in THz MMs. (b) Simulation results for two symmetric coupled SRR as unit cell in THz MMs. (c) Schematic diagram for capacitive coupled THz MMs.

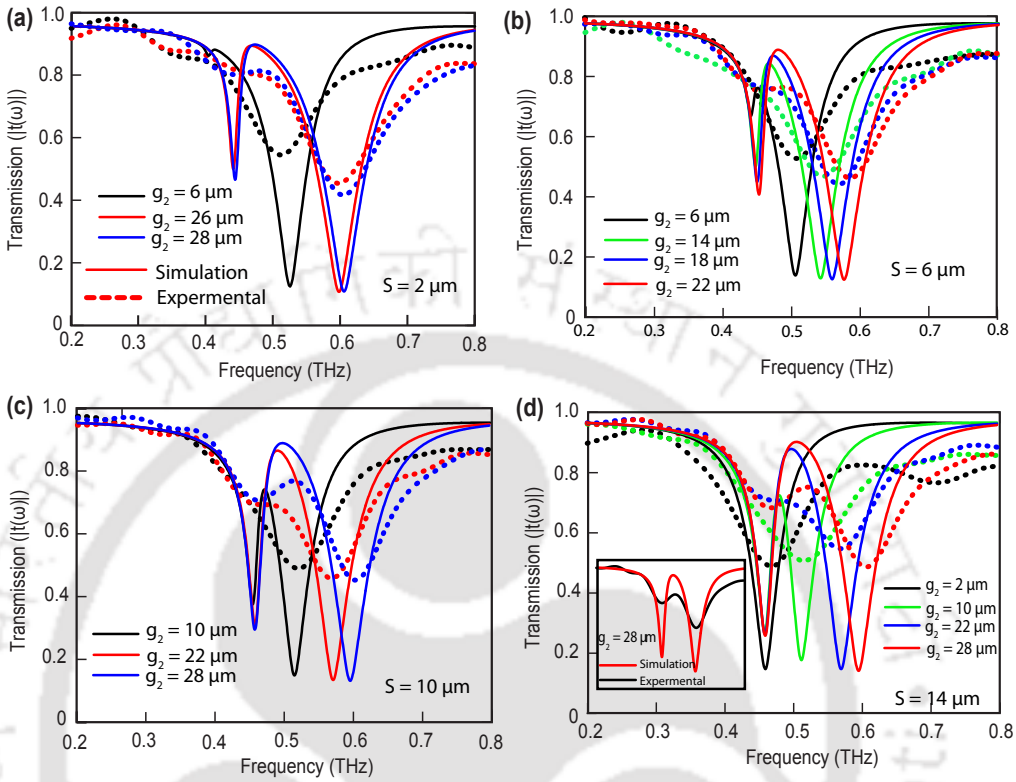

Figure 5.3: Experimental and numerically calculated amplitude spectra for 4 different separations. Dotted lines represent the experimental results and the thick line represents numerical simulation results.

by 130 fs optical pulses with a wavelength of 800 *nm* and a repetition rate of 80 MHz from a Ti: sapphire oscillator laser system generating THz pulses with a bandwidth of 0.2 THz – 3 THz. The polarization of the incident THz electric field is aligned parallel to the gap bearing arms of the SRRs in order to excite the fundamental LC resonance mode (Fig. 5.1) based on the experiments, THz signal was measured in the time domain after transmitting through the metamaterial samples. It was Fourier transformed to obtain the frequency domain spectra, which is further normalized with the signal from a bare silicon substrate of the same thickness (as reference) as used in the metamaterials samples. All the measurements were done at room temperature and in a dry nitrogen atmosphere in order to mitigate the effect due to water vapor absorption. We have studied four different sets of samples corresponding to four different separations (S) between SRRs with a fixed bottom gap (g_1), while the top resonator gap (g_2) is changed gradually

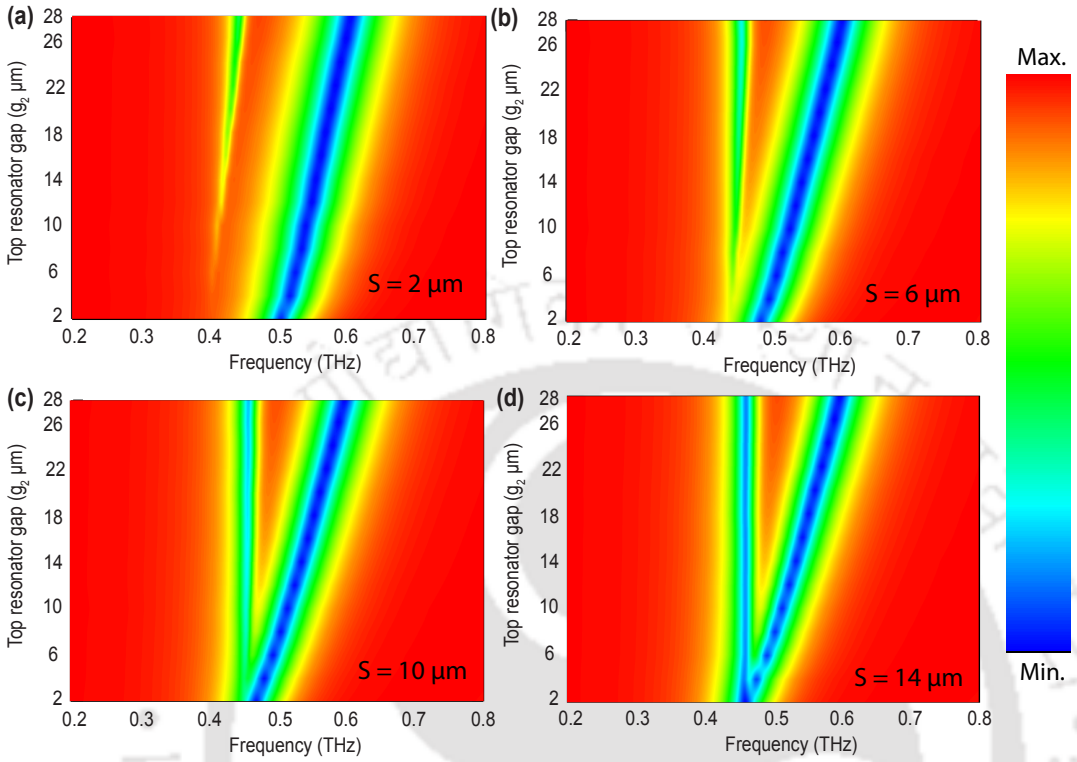

Figure 5.4: Contour plot of numerically simulated THz transmittance for four different separation between two SRRs. Color bar shows the magnitude of transmission intensity. (a) Represents contour plot for separation between two SRRs i.e. S= 2 μm case. (b), (c) and (d) represents contour plots for S = 6, 10, 14 μm respectively.

as indicated in Fig. 5.1 (a). The separation between the resonators is symbolized by S in y direction. In this study, different values of S are considered to be as 2, 6, 10 and 14 μm. We have examined the response of THz transmission through the proposed design for various capacitive gaps (g_2 = 2, 6, 10, 14, 18, 22, 26 and 28 μm) of the top resonator for four different separations (S) both experimentally and numerically. For our numerical study, commercially available numerical software, CST Microwave Studio is employed and tetrahedral meshing is adopted for simulating the metamaterials geometry.

The boundary conditions are taken as periodic in the full wave numerical simulations. We have used waveguide ports as the source and detector. The results of the THz transmission through the planar THz metamaterial systems are discussed elaborately in the next section. In Fig. 5.2 (a) we have shown simulation result for single SRR as a unit cell in THz MMs and In Fig. 5.2 (b) represents simulated transmission result for

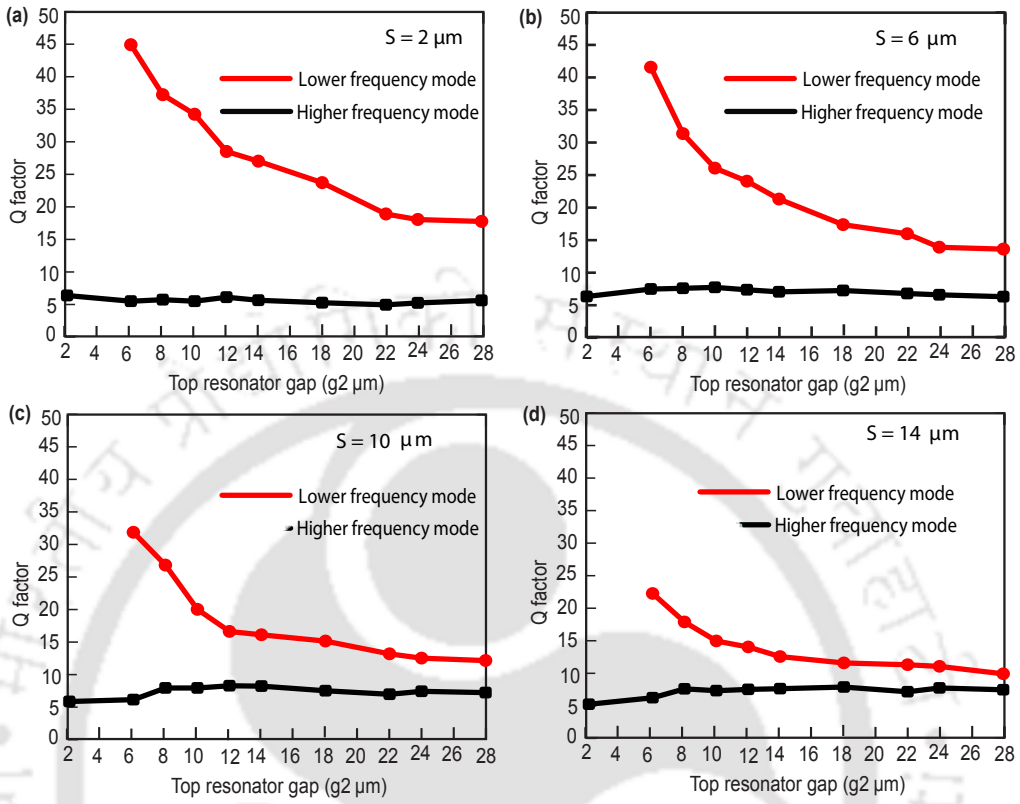

Figure 5.5: (a), (b), (c) and (d) represents Q factor verses top resonator gap plots for S = 2, 6, 10 and 14 μm cases respectively.

coupled SRR as a unit cell. Schematic diagram of THz transmission through capacitive coupled THz MMs shown in Fig. 5.2 (c).

5.2 Results and discussions

The THz transmission results through the fabricated metamaterial samples for four different separations (S) are shown in Fig. 5.3. In Fig. 5.3 (a), the separation (S) between top and bottom SRRs is fixed at 2 μm and the top SRR gap (g_2) is varied for 6 μm, 26 μm and 28 μm. In case of g_2 = 6 μm, high frequency resonance mode is observed at around 0.52 THz and low frequency mode at 0.41 THz. As the top resonator gap changes to 28 μm, we observed a blue shift in the higher order mode i.e. frequency shifts to 0.6 THz while the low frequency resonance remains almost unperturbed. In case of 6 μm separation, high frequency mode appears at 0.5 THz and the low frequency mode appears

around 0.44 THz. As the top gap (g_2) increases, the high frequency mode goes through blue shifting just like the previous case (Fig. 5.3 (b)). Similar trends are observed for separations 10 μm and 14 μm (Fig. 5.3 (c) and (d). We have performed experiments to validate our results which are plotted in dashed lines in Fig. 5.3 along with the numerical simulations. Note that the resonance frequencies in the experiments follow simulations well however the line widths are not in good match. The difference in the line-width of the resonance is primarily due to low spectral resolution of measurement, which is limited by the Fabry-Perot reflection pulse from the rear surface of the substrate. The reflection of terahertz pulse is bound to arise from the rear end of the wafer resulting in reduction in the line width of resonances in measurements. However the good match in position of resonances with respect to frequencies validates our study. The apparent mismatch of resonance line widths is an universal problem in terahertz metamaterials because of measurement limitations as described above, similar results were observed in earlier works too [76, 108]. In order to develop a comprehensive understanding of near field coupling in the proposed metamaterials, we simulated the coupled structures for several top resonator gap for all the four separations. The results are shown in Fig. 5.4 using contour plots. In Fig. 5.4, X axis is taken as frequency (THz), top resonator gap (g_2) is plotted in Y axis and the color bar represents magnitude of transmission. Figure 5.4 (a) shows the terahertz transmission for the case of separation, S = 2 μm, whereas, Fig. 5.4 (b), (c) and (d) shows the transmission results when the separations between the coupled SRRs are S = 6, 10 and 14 μm, respectively. These plots clearly indicates a resonance mode hybridization effect when gap g_2 no longer equal to g_1. As g_2 increases, the split becomes prominent. We attribute the split in resonance to the strong coupling between the resonators primarily.

The higher mode suffers clear blue shifting and this is due to the reduced capacitance of the top resonator where g_2 is increasing leading to reduction in value of split gap capacitance of the top resonator. In order to understand the device performance further, we have calculated the quality factor for both the resonance modes. Quality (Q) factor which is typically defined as Q = $\frac{f_r}{\Delta f}$ (the ratio between the resonance frequency and the bandwidth determined at the full width at $\frac{1}{\sqrt{2}}$ maxima in case of amplitude transmission). We have resonator gap g_2 = 2, 6, 10, 14, 18, 22 and 28 μm. To evaluate quality factor, first we have calculated the full width of each resonance mode at $\frac{1}{\sqrt{2}}$ maxima. For S = 2 μm case, when $g_1 = g_2$ = 2 μm, we have only one resonance mode at 0.5024 THz with full width 0.08 THz and the corresponding Q factor is 6.28 and for g_2 = 6 μm case, we

have two resonance peaks, first resonance peak at 0.405 THz with Δf= 0.009 THz and corresponding Q factor is ~45. The second resonance peak appears at 0.524 THz with Δf = 0.1 THz and corresponding Q factor turns out to be 5.24. Similarly, we have calculated Q factor for g_2 = 10, 14, 18, 22 and 28 μm and results are shown in Fig. 5.5 (a). For S = 6, 10 and 14 μm also, the calculated Q factors are shown in Fig. 5.5 (b), (c) and (d), respectively. In all the cases, we observed lower frequency mode has higher Q factor compared to the higher frequency mode. In case of minimum separation (S = 2 μm) the Q factor observed is maximum.

In order to validate our physical explanations, we have monitored the induced surface current profiles and electric field profiles for strongly coupled regime (Fig. 5.6). In case of S = 2 μm separation with asymmetric split gaps in the resonators, surface currents are shown corresponding to lower and higher resonance modes, see Fig. 5.6 (a) and 5.6 (b). The induced surface currents in the resonators are in phase in case of lower resonance mode and 180 degree out of phase in case of higher resonance mode. This clearly indicates that the resonators are strongly coupled through electric field lines or in other words the resonators are capacitively coupled through the split gaps. In order to validate this explanation, we have further simulated the electric field profiles at the split resonance dips as shown in figures 5.6 (c) and 5.6 (d). Electric field profiles clearly indicate that the resonators are strongly coupled at the split resonances. This also explains the trend in Q factor along with resonance frequency shift. S = 2 μm (Fig. 4 (a)) signifying strongly coupled regime, the resonators are strongest coupled therefore leading to maximum deviation in Q factor along with maximum shift in frequency between the resonance dips (Fig. 5.3 (a) and Fig. 5.4(a)). In Figure 5.6 (c) and (d) shows the spatial configuration of the charge density near the gap and this validates the electric filed coupling is dominant. However as we move to weakly coupled regime, for example S = 14 μm, the difference in Q factor between the modes are lesser. Because of weak capacitive interactions between the resonators the resonance dips are also not deviated from their intrinsic or uncoupled positions. In order to validate this point, we have further simulated the surface current distributions and electric field distributions of the resonators at weakly coupled regime (S = 14 μm) (Fig. 5.7). One may note that the individual resonators are strongly excited at the resonance dips signifying the coupling as weak or almost absent. At the low frequency mode, the lower resonator is excited to its fundamental mode (Fig. 5.7 (a)). Similarly at the higher frequency mode the top resonator is excited to its fundamental mode (Fig. 5.7 (b)). Therefore it clearly shows that the resonators are no coupled but

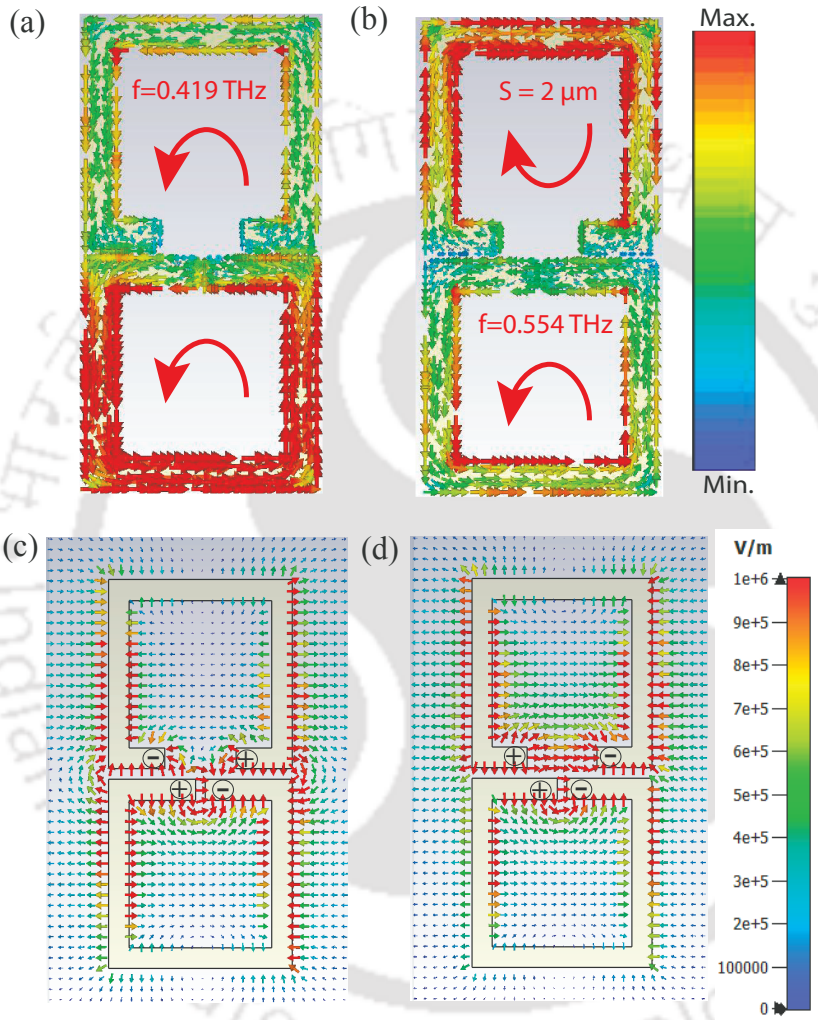

Figure 5.6: (a) & (b) Represent the surface current profile of S= 2 μm case for g_1 =2 μm, g_2 = 14 μm at f=0.419 THz and f=0.554 THz. (c) & (d) Represents the electric field profiles of S= 2 μm case for g_1 = 2 μm and g_2 = 14 μm at f=0.419 THz and f= 0.554 THz. In figures (c) and (d), arrows shows the direction of the electric field and the color and size of the arrows indicates field strength. The polarity of the induced electronic charges on the SRR arms is indicated in the figure.

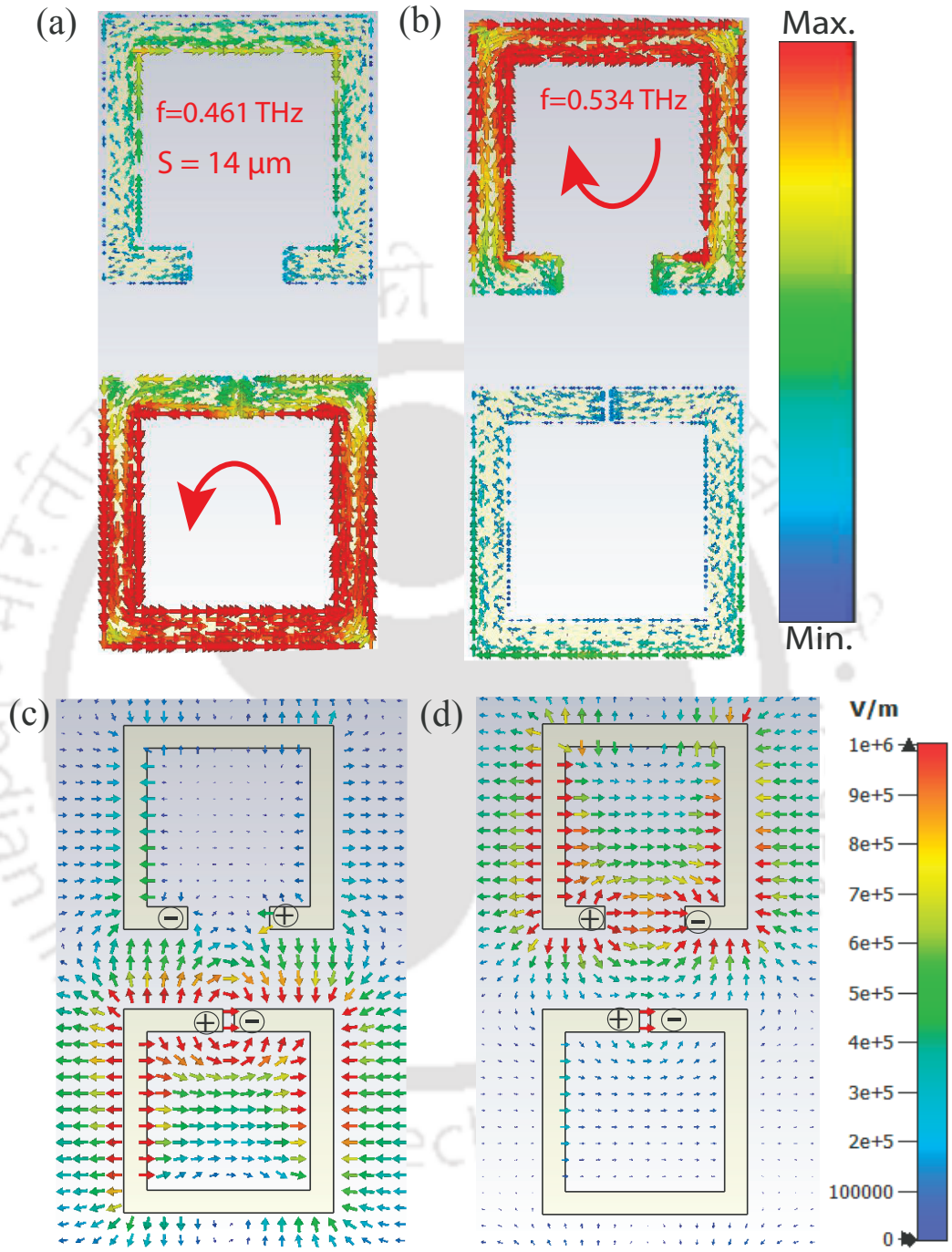

Figure 5.7: (a) & (b) Represent the surface current profile of S= 14 μm case for g_1 = 2 μm, g_2 = 14 μm at f=0.461 THz and f=0.534 THz. (c) & (d) Represents the electric field profiles of S= 14 μm case for g_1 = 2 μm and g_1 = 14 μm at f=0.461 THz and f= 0.534 THz. In figures (c) and (d), arrows shows the direction of the electric field and the color and size of the arrows indicates field strength. The polarity of the induced electronic charges on the SRR arms is indicated in the figure.

resonating close to their intrinsic resonance frequencies. In our study, the focus has been to study near field capacitive coupling of resonances, however, we believe that there may be a weak inductive coupling contribution to the transmission response.

5.3 Conclusions

In this chapter, we have examined the ability to tune resonance behavior via near field capacitive coupling in planar terahertz metamaterials. This has been achieved by manipulating the near field electric interactions via changing one resonator split gap with respect to the other resonator split gap for several inter resonator separations. Introducing asymmetry by changing the split gap in one resonator with respect to the other resonator, results in the mode hybridization when operated in the strong near field coupled regime. The mode hybridization occurs because of the strong near field electric interactions between the resonators. We have further calculated Q factor for the lower and higher resonance modes for different inter resonator separations. We observed that the lower resonance mode has significantly higher Q factor compared to the higher frequency resonance mode. We believe that the higher Q factor observed in the lower frequency resonance mode is due to the strong electric coupling between the resonators. In near field interaction of the resonators, we also observed a blue shift in the higher frequency split resonance. This is attributed to the enhanced split gap size leading to reduced capacitance value. The modulation of resonances in capacitive coupled planar terahertz metamaterial systems has great potential in manipulating and controlling electromagnetic waves which can ultimately result in novel applications for terahertz frequency domain such as designing sensors, antennas, modulators, switches etc.

CHAPTER 6

ULTRAFAST SWITCHING IN SILICON INTEGRATED TERAHERTZ METAMATERIALS

In last three chapters, our focus has been to engineer the resonances in terahertz metamaterials (MMs) by manipulating the near field coupling in the SRRs. In these studies, we focused on tuning the fundamental resonance by varying the geometry of the MM structures in a passive way. However, carefully integrating them with active materials would allow an additional level of control in manipulating the resonance properties of MM with the help of external stimulus. In this chapter, we have focused on active tuning of the resonances at the ultrafast time scale. In past few years, considerable efforts have been made to realize terahertz active devices using different metamaterial configurations. Chen *et al*. demonstrated ultrafast optical switching of resonant response of terahertz metamaterials. A switching response of ~20 ps was demonstrated by engineering the design of carrier lifetime of the ErAs/GaAs super-lattice substrates upon which the metamaterials were fabricated [82]. In another important contributions, Chowdhury *et al*. have examined the ultrafast optical control of near field coupling between the dark and bright modes by placing an ion implanted silicon patch in the dark resonator [73]. Chowdhury *et al*. have also demonstrated reconfigurable

An article based upon the work reported in this chapter is published in *Journal of Infrared, Millimeter, and Terahertz Waves*, vol. **39(12)**, year 2018, pages 1211–1220; title: "Ultrafast Relaxation of Charge Carriers Induced Switching in Terahertz Metamaterials"; authors S. Jagan Mohan Rao, Gagan Kumar, Azad, Abul K and Dibakar Roy Chowdhury.

terahertz metamaterial in which constituent resonators can be switched from split-ring resonators to closed-ring resonators via optical excitation of silicon islands strategically placed in the split gap [61]. Gu *et al*. studied active control of terahertz radiation in classical electromagnetically induced transparency (EIT) metamaterials at room temperature by keeping photo-active silicon patch into SRR gaps of unit cell in metamaterial. An on-to-off active control of the EIT resonance is established by optical pump-terahertz probe (OPTP) measurements. They took a cut wire and two SRRs as unit cell in EIT metamaterial and these two SRRs are placed beside the cut wire, silicon patch is placed in the SRR gaps and studied the terahertz transmission through the sample [109].

Previous studies show that the switching off of metamaterial resonances is determined primarily by the photo-excitation of free carriers throughout the substrate [82]. But our scheme allowed us only in the gap region of the SRR to photo - dope and tune the silicon conductivity at an ultrafast time scale. In this chapter, we demonstrate ultrafast control of intrinsic metamaterial resonances through population and depopulation of the defect states in silicon, strategically placed inside the split gap of single gap ring resonator. This scheme has potentials to enable ultrafast terahertz devices by combining the emerging phenomena of metamaterials with well-established silicon platforms. The metamaterial samples studied in this work consist of single gap SRRs with a radiation damaged silicon layer placed solely inside the SRRs gap. In the next section, in order to understand the carrier life time dynamics of the radiation damaged silicon and their role in ultrafast switching, we have considered tri-exponential theoretical model in conjunction with the experimental observations. Finally results are summarized into the conclusion section.

6.1 Ultrafast metamaterial design and experimental results

Our metamaterial samples were fabricated on radiation damaged silicon-on-sapphire (SOS) wafer [110]. The wafer consists of a 660-nm-thick epilayer of <100> oriented radiation damaged silicon epitaxially grown on a 530-μm-thick sapphire substrate. The silicon layer was implanted with two doses of O^+ ion, $1.0 \times 10^{15}/cm^2$ at 200 keV and $1.0 \times 10^{15}/cm^2$ at 100 keV. The samples were fabricated using two-step photo-lithography. First, photo-lithography was done to create patterns to form metal resonators. Followed by this

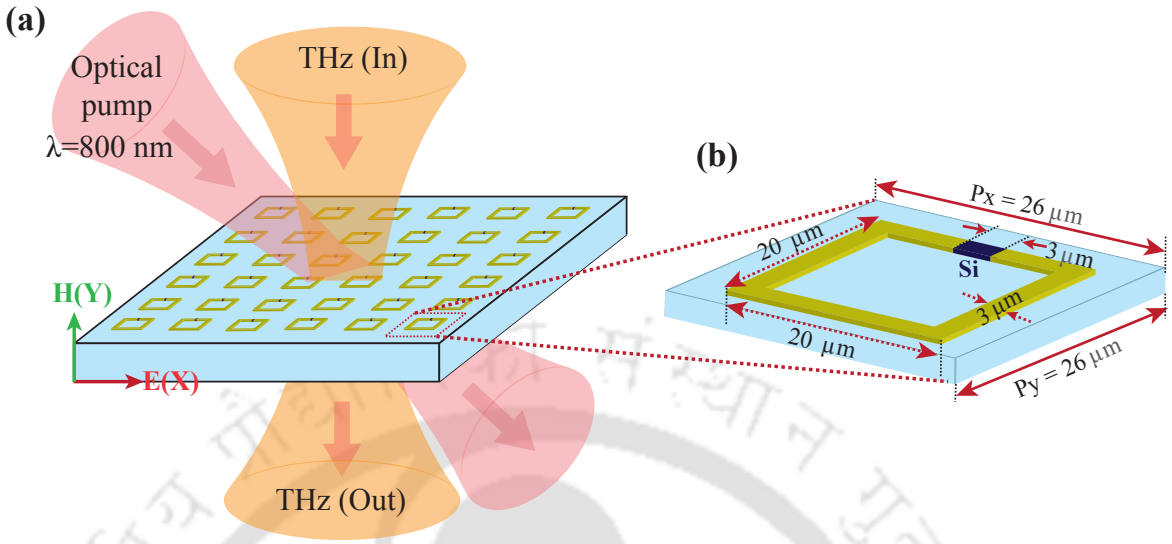

Figure 6.1: (a) Schematic of the SRR array depicting the MM sample studied in this work. (b) Unit cell of MM sample. The geometrical dimensions of the SRR are indicated inside the figure. In the image, P_x and P_y are periodicities in the x and y directions, respectively and silicon is placed inside the split gap.

step, 10-nm-thick titanium and 200-*nm*-thick gold layer were deposited by electron beam evaporation, which was then lifted-off to form the single gap SRR array. In the second step, photo-lithography was performed to cover the split gap of the SRRs but to expose the remaining silicon layer across the entire sample area. With plasma etching, silicon was removed from the entire sample except the gap region of the SRR which was masked by the photo-resist. The schematic design of the sample along with the optical images of the fabricated sample are shown in Fig. 6.1 with the detailed geometric dimensions. The metamaterial samples were characterized using the optical pump terahertz probe (OPTP) measurement technique [89, 111] where the polarization of the incident THz electric field was carefully aligned parallel to the gap bearing SRR arm in order to excite the resonance modes (Fig. 6.1 (b)). A near-infrared femtosecond (fs) laser beam, with a pulse duration of 30 fs, energy of 3.2 mJ/pulse operating at 800 nm with a 1 kHz repetition rate, was employed for terahertz generation/detection and optically pumping the sample. The pump laser beam had a beam diameter of ~1 cm, much larger than the focused THz spot diameter of ~3 mm at the sample, providing uniform excitation over the SOS film in the split gaps of our metamaterial sample. The time delay between optical-pump and terahertz-probe pulses was precisely controlled using a linear translation stage to change the optical path length of the femtosecond optical pulses. For several pump-

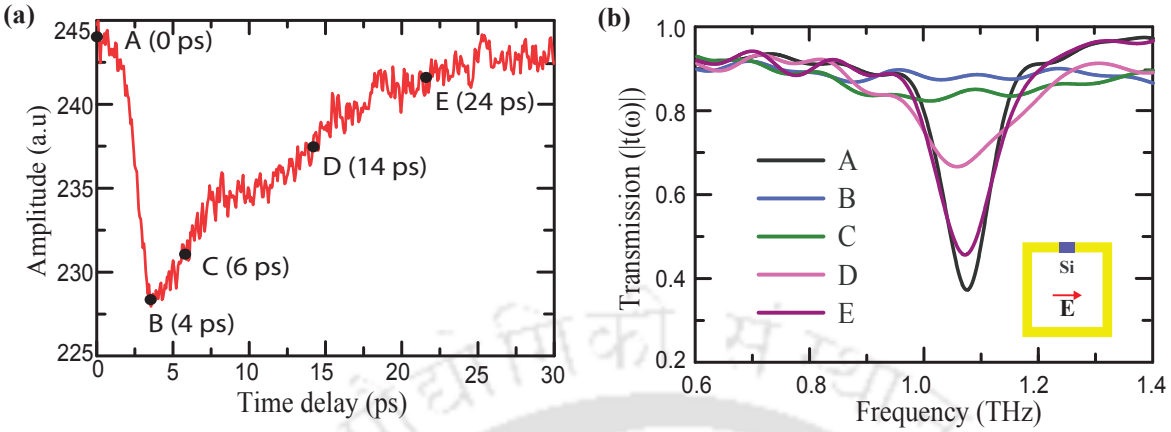

Figure 6.2: (a) Transient change in the terahertz transmission peak due to the optical pump induced conductivity in RD-SOS. (b) Transmitted E-field amplitude through the metamaterial sample at various pump-probe delays. The incident electric field polarization was carefully aligned along the gap-bearing arm of the SRR.

probe time delays, the THz signal was measured in the time domain after transmission through the metamaterial samples. The time domain signals were transformed to the frequency domain and normalized using a bare sapphire substrate as the reference. All the measurements were performed at room temperature and in a dry atmosphere in order to mitigate unwanted absorption introduced by the presence of water vapour in the ambient air. The carrier lifetime dynamics of the radiation damaged unpattern SOS film at pump fluence of 1400 μJ/cm^2 was measured. Fig. 6.2 (a) depicts change in transmitted THz peak signal as a function of time delay between the optical pump beam and the THz probe pulses. The photo-carriers generated by the near-infrared optical excitation in the silicon layer, initially causing a decrease in the transmitted THz signal because of the transient conductivity.

As the time delay increases, the transmitted THz signal increases due to carrier trapping in the radiation damaged silicon [112]. Fig. 6.2 (a) shows that the THz peak is reduced as the optical pulse arrives and then recovers to its full strength within next 20 ps. As revealed by the carrier dynamics of the radiation damaged silicon film, the photo-carrier concentration in silicon layer changes as a function of the pump probe time delay (Fig. 6.2 (a)) due to the characteristic carrier lifetime. This change in charge carrier concentration is directly reflected in change in conductivity as demonstrated in Fig. 6.2 (a). Terahertz transmission measurements through the metasurface sample were carried out at several pump probe delays as indicated in Fig. 6.2 (a). The amplitude transmission

through the metamaterial sample shows strong fundamental resonance at 1.08 THz before the arrival of the optical pump pulse (point A in Fig. 6.2 (a)). At a time delay of ~4 ps after the arrival of pump pulses (point B in Fig. 6.2 (a)), we observe the complete disappearance of the fundamental resonance, allowing a flat transmission spectra ~1.08 THz represented by the blue curve where the fundamental resonance previously was existed. At a time delay of ~6 ps (point C), the transmission still remains flat without any indication of resonance. At a longer time delay of ~12 ps (point D in Fig. 6.2 (a)), there is an evolution of a feeble resonance feature near 1.08 THz. At delay of 24 ps, the strong fundamental resonance reappears again at 1.08 THz (point E in Fig. 6.2 (b)). Before the arrival of pump beam (point A), the transmission spectrum of the metamaterial sample shows strong resonance due to the intrinsic dielectric nature of the silicon in the split gaps, supporting the fundamental LC resonance mode. This fundamental mode is excited by the incident electric field due to the asymmetry of the SRR [61, 67, 72].

As the pump-probe delay increases, the transmission spectrum reaches to point B due to the photo-excited carrier generation. At point C, the resonance remains suppressed because of the conduction of silicon islands inside the split gap. Although at this point, a fraction of the photo-carriers have been trapped, the overall conductivity of the silicon still remains high enough to prohibit the electric field build-up required to drive LC oscillations. At longer delays (point D), a major fraction of photo carriers depart from the conduction band through the carrier trapping as confirmed by the change in terahertz transmission measured in Fig. 6.2 (a). Due to the reduction in its conductivity of the silicon patches in split gaps, we observe the reappearance of the fundamental resonance at 1.08 THz. As the optical pump delay increases (≥24 ps, point E), all the excited photo-carriers are completely trapped, restoring the loss-less dielectric nature of the silicon region in the split gap, therefore, the SRR is able to support full-strength LC resonance at 1.08 THz as revealed in Fig. 6.2 (b).

6.2 Numerical simulation results

In order to confirm our qualitative explanation regarding the experimental demonstration of resonance switching, we performed finite-element simulations using commercially available numerical software Microwave Studio from Computer Simulation Technology (CST) [88]. In our full wave numerical simulations, we have used periodic boundary conditions to simulate a single unit cell, as shown in Fig. 6.1 (b) and in the inset of Fig. 6.

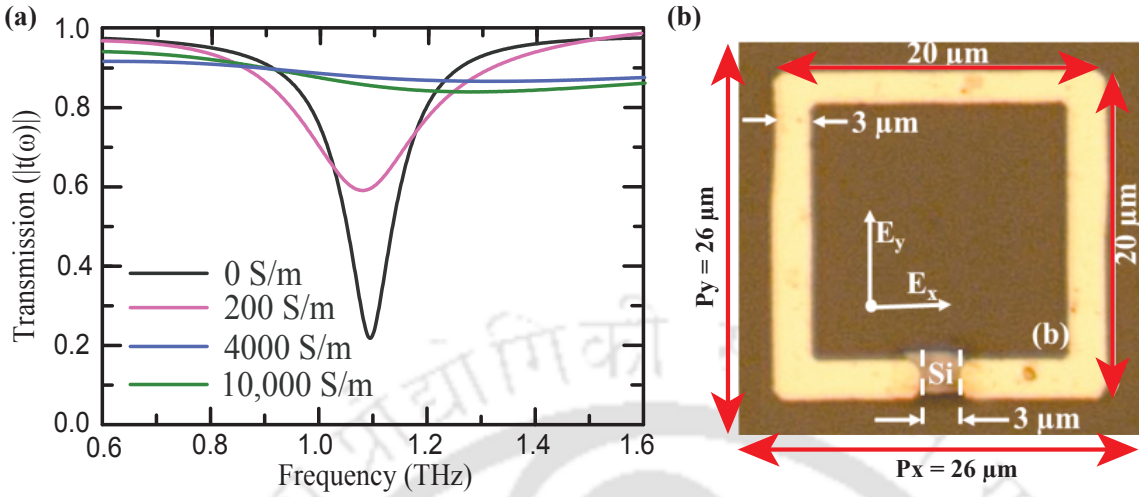

Figure 6.3: (a) Numerical simulations of electric field amplitudes transmitted through the MM sample for different silicon conductivities in the split gap. (b) Optical image of the unit cell of the fabricated MM sample.

3. An adaptive mesh configuration is employed, generating ~30000 tetrahedron mesh cells during the numerical simulations. The transmitted component of the S parameter through the sample is normalized with a blank sapphire substrate in order to replicate the experimental data. During the simulation the excited E-field was set parallel to the gap-bearing arm of SRRs as shown in Fig. 6.1 (b). The metal resonators (gold) were simulated as lossy metal with a conductivity of 6.7×10^7 S/m, whereas the sapphire substrate was modeled as a lossless dielectric with permittivity equal to 10.5. Silicon in the gap is modeled as lossy silicon with variable conductivity in order to account for the effect of photo-excitation in the silicon region placed inside the split gap at different pump probe delays.

The simulation results are shown in Fig. 6.3 (a) and excellent agreement is observed both quantitatively and qualitatively when compared to the experimental measurements. Numerical simulation at point A is done by considering intrinsic silicon in the gap region without any photo-doping. Next, we considered a silicon conductivity value of 10,000 S/m to reproduce the situation at pump-probe delay of 4 ps (point B in Fig. 6.2 (a)). Experimental transmission at point C is modeled by assigning conductivity equal to 4,000 S/m. For point D, a relatively small value of silicon conductivity (200 S/m) is assigned in simulations. We have observed a weakened resonance at this point since there is an initial damping of the resonance strength due to the Ohmic losses in the silicon in the gap region (Fig. 6.2 (b) and Fig. 6.3 (a). At point E, the carriers are completely relaxed

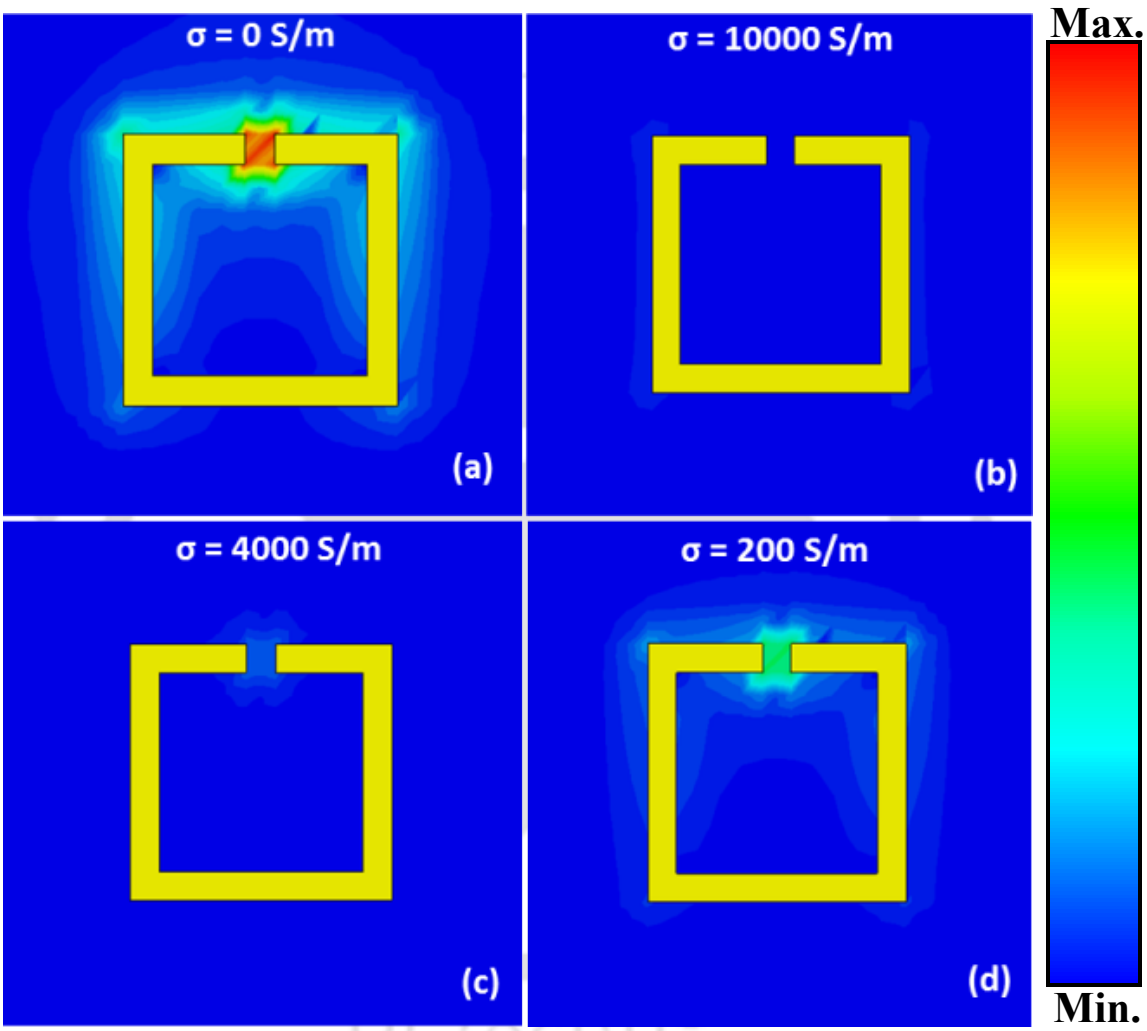

Figure 6.4: simulated induced electric field at fundamental resonance frequency (1.08 THz) for different conductivities of silicon in the split gap resembling the situations with different pump-probe time delay. In all the sub-figures, the same scale is employed to represent the induced electric field strength.

from the conduction band. So the situation is equivalent to the case we observed at point A in the lifetime dynamics plot. A little difference in the simulations and experimental line widths can be noticed, which can be contributed to the low spectral resolution of measurement and imperfection in the sample fabrication. In Fig. 6.4, we have plotted the induced electric field distribution for several silicon conductivities but at the same frequency (1.08 THz) where fundamental resonance appeared. With silicon conductivity σ = 0 S/m (point A), a strong electric field enhancement takes place inside the split gap confirming the mode is due to the inductive capacitive (LC) resonance (Fig. 6.4 (a)). When resonances are measured at the peak of the pump beam, as in the situation at point B of pump-probe delay, the high conductivity of silicon in the split gap transiently modifies the physical configuration of the spit-ring-resonator to a closed-ring-resonator which does not allow a LC resonance at 1.08 THz. Therefore, we do not see any electric field confinement in the split gap (Fig. 6.4 (b)). This indicates the complete switch OFF of LC resonance mode. As the time delay is increased further (situation at point C), the conductivity inside the split gap still remains high hence still unable to support the fundamental resonance mode. Therefore the induced electric field strength in the split gap remains very low (Fig. 6.4 (c)) confirming that the LC mode is still OFF. With further delay at point D, a large fraction of charge carriers have recombined, so the electrical conductivity of the split gap is reduced considerably and we see the evolution of resonance with reduced strength in transmission. The simulated electric field supports this fact with reduced amount of electric field strength induced in the split gap region as seen in Fig. 6.4 (d).

6.3 Tri-exponential analytical model

The radiation damaged silicon exhibits fast carrier response time due to their relatively short free carrier lifetimes. The short carrier lifetime is ensured because of the introduction of defects into the crystalline semiconductor. The carrier dynamics in the radiation damaged silicon are primarily determined by the free-carrier relaxations through the defect states [112]. In order to understand the underlying mechanism involved in the ultrafast carrier dynamics of our experimental study, we employ a tri-exponential theoretical model,

$$I = Ae^{\frac{-t}{\tau_1}} + Be^{\frac{-t}{\tau_2}} + Ce^{\frac{-t}{\tau_3}} \tag{6.1}$$

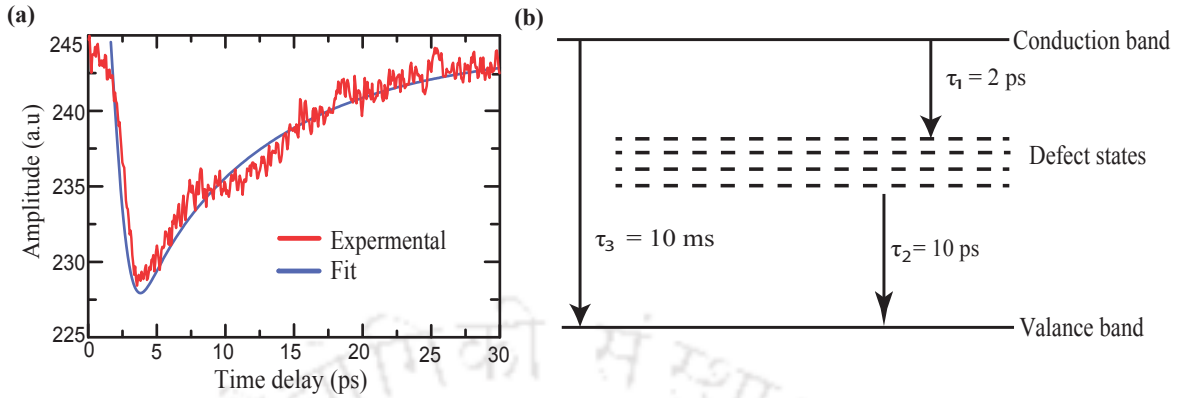

Figure 6.5: (a) Carrier lifetime dynamics of radiation-damaged silicon plots - theoretical and experimental. (b) Charge carriers can relax via three process: into the ion trap states (τ_1, τ_2) or radiative recombination from conduction band to valence band (τ_3).

where, I represents the absorption of the THz probe and t is the time delay between the optical pump and THz probe. τ_1, τ_2 and τ_3 are three relaxation time constants. A, B and C provide information about the fraction of carriers participating in each relaxation process. We used equation (6.1) to fit experimental observations, hence calculate the relaxation time constants. The results are shown in Fig. 6.5 (a). The red traces represent experimental observations while the blue traces correspond to the theoretical fitting. It may be noted that the theoretical model fits in a reasonably good agreement to the experimental observations. We calculated the different parameters used for fitting which are as follows: A = 40, B = 135, C = 155, τ_1 = 2 ps, τ_2 = 10 ps and τ_3 = 10 ms the different relaxation times as indicated by theoretical model can be explained through Fig. 6.5 (b). It shows that the carrier relaxations occur via two different mechanisms. One mechanism involves band to band direct recombination while the other occurs via the defect states present in the energy band gap. During ion-implantation of crystalline silicon, the defects are formed between the conduction band and valance band. These defects can facilitate the relaxation of carriers from the conduction band to the valence band. In radiation damaged silicon, these defect states lie close to the conduction band [113, 114]. The rate of relaxation from the conduction band edge into the defect state is fast. Typical relaxation time constant for this transition is τ_1 = 2 ps as indicated in Fig. 6.5 (b). Similarly we attribute the relaxation time constant of τ_2 = 10 ps is due to carrier relaxation from the defect state to valance band. The carrier relaxation time of intrinsic silicon is usually large and of the order of millisecond due to the direct transition from the conduction band to valance band. In our case of the order of $\tau_3 \approx$ 10 ms which

corresponds to the direct transitions between the conduction band and valance band [114–117]. The ultrafast response of metamaterials is actually originated through the relaxation processes involving the τ_1 and τ_2 processes.

6.4 Conclusions

In conclusion, we have demonstrated fundamental resonance switching of single gap SRR based planar THz metamaterial in an ultrafast timescale. Resonance switching on an ultrafast time scale is achieved by selective, but transient, excitation of split gap conductivity. The evolution of the fundamental resonance mode is studied at different pump-probe time delays. The different time constants involved in the carrier relaxation mechanisms during the process of active switching of terahertz metamaterials are identified using a tri-exponential analytical model. Numerical simulations of induced electric field distributions inside the split ring resonator confirms our experimental findings too. The silicon based device structure adopted in this work can provide a unique platform to integrate current metamaterials with silicon technology. Additionally this scheme can be helpful in realizing ultrafast metamaterials based THz switches.

CHAPTER 7

SUMMARY AND FUTURE WORK

In the first section of this chapter, we present a summary of this thesis work. In the next section, we discuss future scopes of this work and possible directions.

7.1 Summary

In this thesis, we have studied the near field coupling and ultrafast resonance switching in terahertz metamaterials. Near field coupling and ultrafast switching in terahertz metamaterials is an evolving research field in physics that have gathered huge research interests recently as evident from the recent literatures [59, 61, 73–76, 79–82, 85–87, 91, 95, 100, 118, 119]. As an introduction to the thesis, chapter 1 presented a comprehensive review of the literature in the field of terahertz metamaterials and the strengths of near field coupling in metamaterials and ultrafast switching through metamaterials. The applications of these mechanisms in developing next generation metadevices for terahertz gap is also discussed in this chapter. In chapter 2, we have discussed the design, fabrication, and characterization of terahertz metamaterials. As a tool to elucidate numerical findings and experimental observations, we have also discussed the RLC circuit model in this chapter.

In the next three chapters, we have explored different novel schemes of near field couplings in terahertz metamaterials. Near field coupling phenomena in metamaterials plays an important role in designing terahertz metadevices. We have studied two

different types of near field coupling mechanisms. When coupling happens through the circumference of SRRs, magnetic or inductive coupling dominates through magnetic field lines. In case of coupling taking place through the gaps of SRRs, electric or capacitive coupling dominates as coupling takes place through electric field lines. Chapter 3 investigates the near field inductive coupling in edge side coupled terahertz metamaterials. The effect of vertical displacements of resonators is examined on the coupling response and hence on the terahertz wave modulations. The metamaterial system demonstrates resonance mode hybridization effect due to the coupling between two resonance modes of [73, 91] coupled resonators. We have employed RLC theoretical model to understand the coupling mechanism in this near field coupled metamaterial system.

In edge coupled metamaterials, normally a limited interaction between the meta-resonators comprising the unit cell happens. This is due to the physical separation between the resonators since two resonators are placed side by side limiting the near field inductive coupling. Broadside coupled metamaterials can improve this issue by taking advantage of coupling among individual metasurface layers, resulting in strong near field coupling. In chapter 4, we discuss near field inductive coupling in broadside coupled terahertz metamaterials. In this broadside coupled terahertz metamaterial, unit cell is comprised of two split ring resonators separated by a polyimide spacer and these two resonators are twisted in orthogonal fashion. First resonator is placed just above the substrate and we call it as bottom resonator and second resonator is placed above the polyimide spacer and this we call it as top resonator. The tuning of resonances in the metamaterials systems realized by varying the near field interactions via shifting the top resonator with respect to the bottom resonator both in horizontal as well as vertical directions within the unit cell of metamaterial. The RLC circuit model further elucidates numerical simulation results and help us to understand the coupling response in this bilayer terahertz metamaterials system.

In addition to inductive coupling, near field capacitive coupling is also equally important to realize high performance metadevices. Also such schemes allow one more degree of freedom to tune terahertz metamaterials responses. In chapter 5, we have focused upon near field capacitive coupling in terahertz metamaterials which comprises of a pair of single split gap ring resonators. We manipulate the near field electric interactions via changing the one resonator split gap with respect to the other for several inter resonator separations in the unit cell of a metamaterial. We observed resonance mode hybridization effect because of asymmetry in the SRR gaps and switching from strongly coupled regime

to weakly coupled regime. We have further analyzed the Q-factors of the different excited modes to get more insight of the resonance modes.

In order to realize, high speed metadevices, active tunable response of resonances at ultrafast time scale is highly important. In chapter 6, we studied ultrafast switching of fundamental (inductive-capacitive) resonant mode in terahertz metamaterials through optical excitation of radiation damaged silicon placed in the gap of a single split gap ring resonator. We observe the dynamic transition of the fundamental resonance from ON-to-OFF state in a time scale of 4 picoseconds (ps) and then rapid recovery of the resonance to the ON-state within next 20 ps. At the point when the conductivity of radiation damaged silicon is extremely small replicating the dielectric condition, we observe the evolution of strong resonance in transmission mode and when the radiation damaged silicon conductivity goes to higher, we observe no resonance in transmission mode. Higher conductivity in the gap region destroys the capacitive nature of the split gap, hence switching OFF the LC resonance mode. We performed the finite - element simulations using CST Microwave Studio to confirm our qualitative explanation for the experimental demonstration of resonance mode switching. We further employed tri-exponential charge carrier relaxation model to understand the carrier relaxation processes happening inside the radiation damaged silicon.

Because of its potential in the development of terahertz devices, near field coupling in terahertz metamaterials has proven to be a promising area of research. Interaction between resonant elements in metamaterial can result in several novel phenomena and interesting applications that cannot be achievable with conventional uncoupled single resonator based metamaterials. Such effects are resonance mode hybridization [61, 91], Electromagnetically induced transparency [109, 120], Fano type resonances [121], broadband response [75] polarization rotations [81] etc. Near field coupling in metamaterials can also give rise to blue or red shift of fundamental mode, which can be useful in making modulators and frequency tunable devices. Metamaterial tuned by broadside coupling enables resonances to be realized at frequencies lower than the natural resonance of individual SRRs involved in the design of electrically small antennas [118]. On the other hand, the switching of the metamaterial resonances from ON to OFF on ultrafast time scale in THz metamaterials is mainly determined by the photo-excitation of free carriers in radiation damaged silicon, in which the lifetime of the carrier is picosecond. Such metamaterials can therefore be used to make ultrafast THz devices, for example, ultrafast switches and modulators.

7.2 Future scope of work

The field of terahertz metamaterial is rapidly growing and our investigations can play a significant role in the realization of terahertz components in near future. In this thesis, I have focused mainly on near field coupling and ultrafast switching in terahertz metamaterials. These phenomena can be important to several future applications to fill the terahertz gap. Polarization rotation is an essential phenomena to several applications [122, 123]. In optical domain, we have well established techniques for polarization conversion such as total internal reflection principle, wave retardation, Brewster's method etc. In terahertz domain, we are lacking with polarization conversion devices [81, 124, 125]. In this context, near field coupled system can be useful for the polarization conversion as well as rotation in terahertz domain.

In our study, we have focused upon the near field coupling and its passive control by changing structural parameters of the metamaterials. An active control on near field coupling and hence of terahertz transmission response of metamaterials is important to build terahertz devices. In this context, graphene metamaterials [126] in the terahertz domain can lead to the active control of the metamaterial responses. It is possible to change the optical and electronic properties of graphene by external stimulation and therefore, graphene metamaterials could pave the way for futuristic actively tunable terahertz devices [127]. In this thesis work, our focus has also been to study the excitation of high-Q factor modes in the terahertz domain. These modes could potentially be useful to perform highly sensitive refractive index sensing of the analytes besides other typical sensing applications. Our study on near field capacitive coupling can be further extended to achieve optimized parameter for ultra-high Q-factor modes [128, 129]. It would be interesting to perform the sensing measurements on these high Q-modes through experiments and theory.

Recently, slow light systems have attracted considerable interest owing to its promising applications such as optical buffers, optical memories and variable optical delays [130, 131]. In this context, electromagnetically induced transparency (EIT) has emerged as one of the most effective tool to manipulate dispersive properties of the materials [132, 133]. EIT is a quantum interference effect that occurs in three-level atomic systems and gives rise to a narrow transparency window within a broad absorption spectrum. The EIT - like spectral response is generally a result of destructive interference between the resonances of the bright and dark mode. In manipulating the speed of light and coupled

terahertz metamaterials could be an attractive area to pursue through this route.

APPENDIX A

IMPEDANCE CALCULATION

Here we have calculated the impedance values for silicon (Si), Gallium Arsnide (GaAs), and free space. Permitivity of Si is 11.9, permitivity of GaAs is 12.94, free space permeability(μ_0) = 1.26×10^{-6} H/m, free space permittivity (ϵ_0) = 8.85×10^{-12} F/m, and μ_r=1.

A.1 Impedance calculation for silicon

$$Z_s = \sqrt{\frac{\mu}{\epsilon}} \tag{A.1}$$

$$Z_s = \sqrt{\frac{\mu_0 \mu_r}{\epsilon_0 \epsilon_r}} \tag{A.2}$$

$$Z_s = \sqrt{\frac{1.26 \times 10^{-6} \times 1}{8.85 \times 10^{-12} \times 11.9}} = 109.38\Omega \tag{A.3}$$

A.2 Impedance calculation for Gallium Arsenide

$$Z_g = \sqrt{\frac{\mu}{\epsilon}} \tag{A.4}$$

$$Z_g = \sqrt{\frac{\mu_0 \mu_r}{\epsilon_0 \epsilon_r}} \tag{A.5}$$

$$Z_g = \sqrt{\frac{1.26 \times 10^{-6} \times 1}{8.85 \times 10^{-12} \times 12.94}} = 104.89\Omega \tag{A.6}$$

A.3 Impedance calculation for free space

In free space relative permeability and relative permittivity are equal to unity, so the impedance equation is simplified to the following equation

$$Z_0 = \sqrt{\frac{\mu_0}{\epsilon_0}} \tag{A.7}$$

$$Z_0 = \sqrt{\frac{1.26 \times 10^{-6}}{8.85 \times 10^{-12}}} = 377\Omega \tag{A.8}$$

APPENDIX B

R, L, AND C VALUES CALCULATION FOR CHAPTER 3

The length of SRR is 40 μm, width (w) of SRR is 6 μm, gap of SRR is 2 μm, gold thickness (t) is 0.2 μm, and total length (l) of SRR is $4 \times 40\mu$m. The inductance of the SRR is determined by geometric dimensions[134]. From inductance value, we can estimate capacitence value at the resonance frequency by using $\omega = 1/\sqrt{LC}$. The resistance can be estimated from the quality factor (Q = $\frac{1}{R}\sqrt{\frac{L}{C}}$) of the resonance.

B.1 Inductance (L) calculation

$$L = \mu_0 \frac{l}{4} \ln \frac{8l}{w+t} \tag{B.1}$$

$$L = 1.26 \times 10^{-6} \times \frac{4 \times 40 \times 10^{-6}}{4} \ln \frac{8 \times 4 \times 40 \times 10^{-6}}{6 \times 10^{-6} + 0.2 \times 10^{-6}} \tag{B.2}$$

$$L = 268.63 \times 10^{-12} H \tag{B.3}$$

B.2 Capacitence (C) calculation

$$f = \frac{1}{2\pi}\sqrt{\frac{1}{LC}} \tag{B.4}$$

$$C = \frac{10^{-24} \times 10^{12}}{4\pi^2 \times 0.41^2 \times 268} \tag{B.5}$$

where single SRR resonance frequency(f) = 0.41×10^{12} Hz

$$C = 0.562 \times 10^{-15} F \tag{B.6}$$

B.3 Resistance (R) calculation

$$R = \frac{1}{Q}\sqrt{\frac{L}{C}} \tag{B.7}$$

where Q-factor of single SRR resonance frequency is 13.355

$$R = \frac{1}{13.355}\sqrt{\frac{268.63 \times 10^{-12}}{0.562 \times 10^{-15}}} \tag{B.8}$$

$$R = 51.76\Omega \tag{B.9}$$

APPENDIX C

R, L, AND C VALUES CALCULATION FOR CHAPTER 4

The length of SRR is 48 μm, width (w) of SRR is 5 μm, gap of SRR is 12 μm, gold thickness (t) is 0.2 μm, and total length (l) of SRR is $4 \times 48 \mu$m. The inductance of the SRR is determined by geometric dimensions[134]. From inductance value, we can estimate capacitence value at the resonance frequency by using $\omega = 1/\sqrt{LC}$. The resistance can be estimated from the quality factor (Q = $\frac{1}{R}\sqrt{\frac{L}{C}}$) of the resonance.

C.1 Inductance (L) calculation

$$L = \mu_0 \frac{l}{4} \ln \frac{8l}{w+t} \tag{C.1}$$

$$L = 1.26 \times 10^{-6} \times \frac{4 \times 48 \times 10^{-6}}{4} \ln \frac{8 \times 4 \times 48 \times 10^{-6}}{5 \times 10^{-6} + 0.2 \times 10^{-6}} \tag{C.2}$$

$$L = 344.027 \times 10^{-12} H \tag{C.3}$$

C.2 Capacitence (C) calculation

$$f = \frac{1}{2\pi}\sqrt{\frac{1}{LC}} \tag{C.4}$$

$$C = \frac{10^{-24} \times 10^{12}}{4\pi^2 \times 0.38^2 \times 344.027} \tag{C.5}$$

where single SRR resonance frequency(f) = 0.38×10^{12} Hz

$$C = 0.51 \times 10^{-15} F \tag{C.6}$$

C.3 Resistance (R) calculation

$$R = \frac{1}{Q}\sqrt{\frac{L}{C}} \tag{C.7}$$

where Q-factor of single SRR resonance frequency is 13.355

$$R = \frac{1}{13.355}\sqrt{\frac{344.027 \times 10^{-12}}{0.51 \times 10^{-15}}} \tag{C.8}$$

$$R = 61.49\Omega \tag{C.9}$$

APPENDIX D

MATLAB CODE FOR TL-RLC MODEL

Here we have given matlab code for Δx=0% case from Fig. 3.9(a). Other cases just change $R_1, L_1, C_1, R_2, L_2, C_2$, M values and frequency range (if required) and run the program.

```
clc;
clear all;
close all;
r1=18;
l1=348. ×10^-12;
c1=0.433.×10^-15;
r2=112;
l2=680.×10^-12;
c2=0.279.×10^-15;
z0=377;
zs=104.89; (for GaAs)
m=14.×10^-12;
f=0.2. × 10^-12:0.01. × 10^-11:0.6. × 10^-12;
w=2.×pi.×f;
z1=r1+(1j.×((w.×l1)-(1./(w.×c1))));
z2=r2+(1j.×((w.×l2)-(1./(w.×c2))));
A=(z1.×z2)+(w.^2. ×(m.^2));
```

```
B=(z1+z2)-(1j.×(2.× w. ×m));
zt=A./B;
C=(zt. × (z0+zs));
D=(zs. ×(zt+z0))+(zt. × z0);
t=C./D;
plot(f,t);
```

APPENDIX E

SOURCE OF ERROR

Chapter wise possible source of errors can be given as bellow:

Chapter 3 : In this chapter, the focus has been to study near field inductive coupling of resonances in planar terahertz metamaterials, however, we believe that there may be a weak capacitive coupling contribution to the transmission response. This can contribute to the mismatching of simulation with the RLC model, where we only consider inductive coupling effect.

Chapter 4 : In this chapter, the focus has been to study near field inductive coupling of resonances in broadside terahertz metamaterials, however, we believe that there may be a weak capacitive coupling contribution to the transmission response. This can contribute to the mismatching of simulation with the RLC model where we only consider inductive coupling effect.

Chapter 5 : In this chapter, the focus has been to study near field capacitive coupling of resonances in planar terahertz metamaterials, however, we believe that their may be a weak magnetic coupling contribution to the transmission response. The difference in the line-width of the resonance is primarily due to low spectral resolution of measurement, which is limited by the Fabry-Perot reflection pulse from the rear surface of the substrate. The reflection of terahertz pulse is bound to arise from the rear end of the wafer resulting in reduction in the line width of resonances in measurements. However the good match in position of resonances with respect to frequencies validates our study. The apparent

mismatch of resonance line widths is an universal problem in terahertz metamaterials because of measurement limitations as described above, similar results were observed in earlier works too [76, 108].

Chapter 6 : In this chapter, a little difference in the simulations and experimental line widths can be noticed, which can be contributed to the low spectral resolution of measurement and imperfection in the sample fabrication.

BIBLIOGRAPHY

[1] Xi-Cheng Zhang and Jingzhou Xu. *Introduction to THz wave photonics*, volume 29. Springer, 2010.

[2] M Nagel, P Haring Bolivar, M Brucherseifer, H Kurz, A Bosserhoff, and R Büttner. Integrated thz technology for label-free genetic diagnostics. *Applied Physics Letters*, 80(1):154–156, 2002.

[3] Masayoshi Tonouchi. Cutting-edge terahertz technology. *Nature photonics*, 1(2):97, 2007.

[4] Kiyomi Sakai et al. *Terahertz optoelectronics*, volume 6. Springer, 2005.

[5] Christopher W Berry, N Wang, Mohammad R Hashemi, M Unlu, and Mona Jarrahi. Significant performance enhancement in photoconductive terahertz optoelectronics by incorporating plasmonic contact electrodes. *Nature communications*, 4:1622, 2013.

[6] Nezih T Yardimci, Shang-Hua Yang, Christopher W Berry, and Mona Jarrahi. High-power terahertz generation using large-area plasmonic photoconductive emitters. *IEEE Transactions on Terahertz Science and Technology*, 5(2):223–229, 2015.

[7] Shang-Hua Yang, Mohammad R Hashemi, Christopher W Berry, and Mona Jarrahi. 7.5% optical-to-terahertz conversion efficiency offered by photoconductive emitters with three-dimensional plasmonic contact electrodes. *IEEE Transactions on Terahertz Science and Technology*, 4(5):575–581, 2014.

[8] G Lawrece Carr, Michael C Martin, Wayne R McKinney, K Jordan, George R Neil, and Gwyn P Williams. High-power terahertz radiation from relativistic electrons. *Nature*, 420(6912):153, 2002.

[9] Ajay Nahata, Aniruddha S Weling, and Tony F Heinz. A wideband coherent terahertz spectroscopy system using optical rectification and electro-optic sampling. *Applied physics letters*, 69(16):2321–2323, 1996.

[10] K-L Yeh, MC Hoffmann, J Hebling, and Keith A Nelson. Generation of 10 μ j ultrashort terahertz pulses by optical rectification. *Applied Physics Letters*, 90(17):171121, 2007.

[11] Shuji Matsuura, Masahiko Tani, and Kiyomi Sakai. Generation of coherent terahertz radiation by photomixing in dipole photoconductive antennas. *Applied Physics Letters*, 70(5):559–561, 1997.

[12] Hua Cao and Ajay Nahata. Resonantly enhanced transmission of terahertz radiation through a periodic array of subwavelength apertures. *Optics express*, 12(6):1004–1010, 2004.

[13] HA Hafez, X Chai, A Ibrahim, S Mondal, D Férachou, X Ropagnol, and T Ozaki. Intense terahertz radiation and their applications. *Journal of Optics*, 18(9):093004, 2016.

[14] Yao-Chun Shen. Terahertz pulsed spectroscopy and imaging for pharmaceutical applications: a review. *International journal of pharmaceutics*, 417(1-2):48–60, 2011.

[15] E Pickwell and VP Wallace. Biomedical applications of terahertz technology. *Journal of Physics D: Applied Physics*, 39(17):R301, 2006.

[16] Susan L Dexheimer. *Terahertz spectroscopy: principles and applications*. CRC press, 2007.

[17] YC Shen, PC Upadhya, HE Beere, EH Linfield, AG Davies, IS Gregory, C Baker, WR Tribe, and MJ Evans. Generation and detection of ultrabroadband terahertz radiation using photoconductive emitters and receivers. *Applied Physics Letters*, 85(2):164–166, 2004.

[18] Daniel Mittleman. *Sensing with terahertz radiation*, volume 85. Springer, 2013.

[19] T Globus, D Woolard, M Bykhovskaia, B Gelmont, L Werbos, and A Samuels. Thz-frequency spectroscopic sensing of dna and related biological materials. *International Journal of High Speed Electronics and Systems*, 13(04):903–936, 2003.

[20] Ruth M Woodward, Bryan E Cole, Vincent P Wallace, Richard J Pye, Donald D Arnone, Edmund H Linfield, and Michael Pepper. Terahertz pulse imaging in reflection geometry of human skin cancer and skin tissue. *Physics in Medicine & Biology*, 47(21):3853, 2002.

[21] SW Smye, JM Chamberlain, AJ Fitzgerald, and E Berry. The interaction between terahertz radiation and biological tissue. *Physics in Medicine & Biology*, 46(9):R101, 2001.

[22] Meihong Lu, Jinhai Sun, Sijia Chen, Ning Li, Guozhong Zhao, Jingling Shen, et al. Identification of maize seeds by terahertz scanning imaging. *Chinese Optics Letters*, 3(101):S239–S241, 2005.

[23] Chuji Wang and Peeyush Sahay. Breath analysis using laser spectroscopic techniques: breath biomarkers, spectral fingerprints, and detection limits. *Sensors*, 9(10):8230–8262, 2009.

[24] Hai-Bo Liu, Yunqing Chen, Glenn J Bastiaans, and X-C Zhang. Detection and identification of explosive rdx by thz diffuse reflection spectroscopy. *Optics Express*, 14(1):415–423, 2006.

[25] Nikolay I Zheludev and Yuri S Kivshar. From metamaterials to metadevices. *Nature materials*, 11 (11):917, 2012.

[26] Alexander Poddubny, Ivan Iorsh, Pavel Belov, and Yuri Kivshar. Hyperbolic metamaterials. *Nature photonics*, 7(12):948, 2013.

[27] Jason Valentine, Shuang Zhang, Thomas Zentgraf, Erick Ulin-Avila, Dentcho A Genov, Guy Bartal, and Xiang Zhang. Three-dimensional optical metamaterial with a negative refractive index. *nature*, 455(7211):376, 2008.

[28] Shuang Zhang, Wenjun Fan, NC Panoiu, KJ Malloy, RM Osgood, and SRJ Brueck. Experimental demonstration of near-infrared negative-index metamaterials. *Physical review letters*, 95(13):137404, 2005.

[29] Boris Luk'yanchuk, Nikolay I Zheludev, Stefan A Maier, Naomi J Halas, Peter Nordlander, Harald Giessen, and Chong Tow Chong. The fano resonance in plasmonic nanostructures and metamaterials. *Nature materials*, 9(9):707, 2010.

[30] John B Pendry, Anthony J Holden, David J Robbins, WJ Stewart, et al. Magnetism from conductors and enhanced nonlinear phenomena. *IEEE transactions on microwave theory and techniques*, 47 (11):2075–2084, 1999.

[31] Christophe Caloz and Tatsuo Itoh. *Electromagnetic metamaterials: transmission line theory and microwave applications*. John Wiley & Sons, 2005.

[32] Victor Georgievich Veselago. The electrodynamics of substances with simultaneously negative values of img align= absmiddle alt= ϵ and μ. *Physics-Uspekhi*, 10(4):509–514, 1968.

[33] David R Smith, Willie J Padilla, DC Vier, Syrus C Nemat-Nasser, and Seldon Schultz. Composite

medium with simultaneously negative permeability and permittivity. *Physical review letters*, 84(18): 4184, 2000.

[34] Richard A Shelby, David R Smith, and Seldon Schultz. Experimental verification of a negative index of refraction. *science*, 292(5514):77–79, 2001.

[35] Shuang Zhang, Wenjun Fan, BK Minhas, Andrew Frauenglass, KJ Malloy, and SRJ Brueck. Midinfrared resonant magnetic nanostructures exhibiting a negative permeability. *Physical review letters*, 94(3):037402, 2005.

[36] Shuang Zhang, Yong-Shik Park, Jensen Li, Xinchao Lu, Weili Zhang, and Xiang Zhang. Negative refractive index in chiral metamaterials. *Physical review letters*, 102(2):023901, 2009.

[37] Bingnan Wang, Jiangfeng Zhou, Thomas Koschny, Maria Kafesaki, and Costas M Soukoulis. Chiral metamaterials: simulations and experiments. *Journal of Optics A: Pure and Applied Optics*, 11(11): 114003, 2009.

[38] Tolga Ergin, Nicolas Stenger, Patrice Brenner, John B Pendry, and Martin Wegener. Three-dimensional invisibility cloak at optical wavelengths. *science*, 328(5976):337–339, 2010.

[39] John Brian Pendry. Negative refraction makes a perfect lens. *Physical review letters*, 85(18):3966, 2000.

[40] Vladimir M Shalaev. Optical negative-index metamaterials. *Nature photonics*, 1(1):41, 2007.

[41] S Anantha Ramakrishna and Tomasz M Grzegorczyk. *Physics and applications of negative refractive index materials*. CRC press, 2008.

[42] Tie Jun Cui, David R Smith, and Ruopeng Liu. *Metamaterials*. Springer, 2010.

[43] Filippo Capolino. *Applications of metamaterials*. CRC press, 2009.

[44] Ricardo Marqués, Ferran Martin, and Mario Sorolla. *Metamaterials with negative parameters: theory, design, and microwave applications*, volume 183. John Wiley & Sons, 2011.

[45] Saïd Zouhdi, Ari Sihvola, and Alexey P Vinogradov. *Metamaterials and plasmonics: fundamentals, modelling, applications*. Springer Science & Business Media, 2008.

[46] Wenshan Cai and Vladimir M Shalaev. *Optical metamaterials*, volume 10. Springer, 2010.

[47] Govind Dayal and S Anantha Ramakrishna. Design of multi-band metamaterial perfect absorbers with stacked metal–dielectric disks. *Journal of Optics*, 15(5):055106, 2013.

[48] Oguzhan Akgol, Olcay Altintas, Elif E Dalkılınc, Emin Unal, Muharrem Karaaslan, and Cumali Sabah. Metamaterial absorber-based multisensor applications using a meander-line resonator. *Optical Engineering*, 56(8):087104, 2017.

[49] Hu Tao, Logan R Chieffo, Mark A Brenckle, Sean M Siebert, Mengkun Liu, Andrew C Strikwerda, Kebin Fan, David L Kaplan, Xin Zhang, Richard D Averitt, et al. Metamaterials on paper as a sensing platform. *Advanced Materials*, 23(28):3197–3201, 2011.

[50] Christopher L Holloway, Edward F Kuester, Joshua A Gordon, John O'Hara, Jim Booth, and David R Smith. An overview of the theory and applications of metasurfaces: The two-dimensional equivalents of metamaterials. *IEEE Antennas and Propagation Magazine*, 54(2):10–35, 2012.

[51] Stefan Linden, Christian Enkrich, Martin Wegener, Jiangfeng Zhou, Thomas Koschny, and Costas M Soukoulis. Magnetic response of metamaterials at 100 terahertz. *Science*, 306(5700):1351–1353, 2004.

[52] Hu Tao, AC Strikwerda, K Fan, WJ Padilla, X Zhang, and RD Averitt. Reconfigurable terahertz metamaterials. *Physical review letters*, 103(14):147401, 2009.

[53] Muhan Choi, Seung Hoon Lee, Yushin Kim, Seung Beom Kang, Jonghwa Shin, Min Hwan Kwak, Kwang-Young Kang, Yong-Hee Lee, Namkyoo Park, and Bumki Min. A terahertz metamaterial with unnaturally high refractive index. *Nature*, 470(7334):369, 2011.

[54] WJ Padilla, MT Aronsson, C Highstrete, Mark Lee, AJ Taylor, and RD Averitt. Electrically resonant terahertz metamaterials: Theoretical and experimental investigations. *Physical Review B*, 75(4): 041102, 2007.

[55] Jining Li, Charan M Shah, Withawat Withayachumnankul, Benjamin S-Y Ung, Arnan Mitchell, Sharath Sriram, Madhu Bhaskaran, Shengjiang Chang, and Derek Abbott. Mechanically tunable terahertz metamaterials. *Applied Physics Letters*, 102(12):121101, 2013.

[56] Ranjan Singh, Evgenya Smirnova, Antoinette J Taylor, John F O'Hara, and Weili Zhang. Optically thin terahertz metamaterials. *Optics Express*, 16(9):6537–6543, 2008.

[57] Hou-Tong Chen, Willie J Padilla, Joshua MO Zide, Arthur C Gossard, Antoinette J Taylor, and Richard D Averitt. Active terahertz metamaterial devices. *Nature*, 444(7119):597, 2006.

[58] Hu Tao, Andrew C Strikwerda, Mengkun Liu, Jessica P Mondia, Evren Ekmekci, Kebin Fan, David L Kaplan, Willie J Padilla, Xin Zhang, Richard D Averitt, et al. Performance enhancement of terahertz metamaterials on ultrathin substrates for sensing applications. *Applied Physics Letters*, 97(26): 261909, 2010.

[59] Hou-Tong Chen, John F O'hara, Abul K Azad, Antoinette J Taylor, Richard D Averitt, David B Shrekenhamer, and Willie J Padilla. Experimental demonstration of frequency-agile terahertz metamaterials. *Nature Photonics*, 2(5):295, 2008.

[60] Ta-Jen Yen, WJ Padilla, Nicholas Fang, DC Vier, DR Smith, JB Pendry, DN Basov, and Xiang Zhang. Terahertz magnetic response from artificial materials. *Science*, 303(5663):1494–1496, 2004.

[61] Dibakar Roy Chowdhury, Ranjan Singh, John F O'Hara, Hou-Tong Chen, Antoinette J Taylor, and Abul K Azad. Dynamically reconfigurable terahertz metamaterial through photo-doped semiconductor. *Applied Physics Letters*, 99(23):231101, 2011.

[62] Shuang Zhang, Jiangfeng Zhou, Yong-Shik Park, Junsuk Rho, Ranjan Singh, Sunghyun Nam, Abul K Azad, Hou-Tong Chen, Xiaobo Yin, Antoinette J Taylor, et al. Photoinduced handedness switching in terahertz chiral metamolecules. *Nature communications*, 3:942, 2012.

[63] Fusheng Ma, Yu-Sheng Lin, Xinhai Zhang, and Chengkuo Lee. Tunable multiband terahertz metamaterials using a reconfigurable electric split-ring resonator array. *Light: Science & Applications*, 3 (5):e171, 2014.

[64] Hou-Tong Chen, Willie J Padilla, Michael J Cich, Abul K Azad, Richard D Averitt, and Antoinette J Taylor. A metamaterial solid-state terahertz phase modulator. *Nature photonics*, 3(3):148, 2009.

[65] Hou-Tong Chen, Hao Yang, Ranjan Singh, John F O'Hara, Abul K Azad, Stuart A Trugman, QX Jia, and Antoinette J Taylor. Tuning the resonance in high-temperature superconducting terahertz metamaterials. *Physical review letters*, 105(24):247402, 2010.

[66] Zhongyang Li, Yingfang Ma, Ran Huang, Ranjan Singh, Jianqiang Gu, Zhen Tian, Jiaguang Han, and Weili Zhang. Manipulating the plasmon-induced transparency in terahertz metamaterials.

Optics express, 19(9):8912–8919, 2011.

[67] N Katsarakis, Th Koschny, M Kafesaki, EN Economou, and CM Soukoulis. Electric coupling to the magnetic resonance of split ring resonators. *Applied Physics Letters*, 84(15):2943–2945, 2004.

[68] N Katsarakis, G Konstantinidis, A Kostopoulos, RS Penciu, TF Gundogdu, M Kafesaki, EN Economou, Th Koschny, and CM Soukoulis. Magnetic response of split-ring resonators in the far-infrared frequency regime. *Optics letters*, 30(11):1348–1350, 2005.

[69] Willie J Padilla, Antoinette J Taylor, Clark Highstrete, Mark Lee, and Richard D Averitt. Dynamical electric and magnetic metamaterial response at terahertz frequencies. *Physical review letters*, 96 (10):107401, 2006.

[70] Ranjan Singh, Ibraheem AI Al-Naib, Martin Koch, and Weili Zhang. Asymmetric planar terahertz metamaterials. *Optics express*, 18(12):13044–13050, 2010.

[71] T Driscoll, GO Andreev, DN Basov, S Palit, SY Cho, NM Jokerst, and DR Smith. Tuned permeability in terahertz split-ring resonators for devices and sensors. *Applied Physics Letters*, 91(6):062511, 2007.

[72] Carsten Rockstuhl, Falk Lederer, Christoph Etrich, Thomas Zentgraf, Jürgen Kuhl, and Harald Giessen. On the reinterpretation of resonances in split-ring-resonators at normal incidence. *Optics express*, 14(19):8827–8836, 2006.

[73] Dibakar Roy Chowdhury, Ranjan Singh, Antoinette J Taylor, Hou-Tong Chen, and Abul K Azad. Ultrafast manipulation of near field coupling between bright and dark modes in terahertz metamaterial. *Applied Physics Letters*, 102(1):011122, 2013.

[74] Ranjan Singh, Ibraheem Al-Naib, Dibakar Roy Chowdhury, Longqing Cong, Carsten Rockstuhl, and Weili Zhang. Probing the transition from an uncoupled to a strong near-field coupled regime between bright and dark mode resonators in metasurfaces. *Applied Physics Letters*, 105(8):081108, 2014.

[75] Dibakar Roy Chowdhury, Ranjan Singh, Matthew Reiten, Hou-Tong Chen, Antoinette J Taylor, John F O'Hara, and Abul K Azad. A broadband planar terahertz metamaterial with nested structure. *Optics express*, 19(17):15817–15823, 2011.

[76] MT Reiten, D Roy Chowdhury, J Zhou, AJ Taylor, JF O'Hara, and AK Azad. Resonance tuning behavior in closely spaced inhomogeneous bilayer metamaterials. *Applied Physics Letters*, 98(13): 131105, 2011.

[77] Ricardo Marqués, Francisco Mesa, Jesus Martel, and Francisco Medina. Comparative analysis of edge-and broadside-coupled split ring resonators for metamaterial design-theory and experiments. *IEEE Transactions on antennas and propagation*, 51(10):2572–2581, 2003.

[78] Tingting Liu, Zao Yi, and Shuyuan Xiao. Active control of near-field coupling in a terahertz metal-graphene metamaterial. *IEEE Photonics Technology Letters*, 29(22):1998–2001, 2017.

[79] Dibakar Roy Chowdhury, Ranjan Singh, Matthew Reiten, Jiangfeng Zhou, Antoinette J Taylor, and John F O'Hara. Tailored resonator coupling for modifying the terahertz metamaterial response. *Optics express*, 19(11):10679–10685, 2011.

[80] Ranjan Singh, Carsten Rockstuhl, Falk Lederer, and Weili Zhang. Coupling between a dark and a bright eigenmode in a terahertz metamaterial. *Physical Review B*, 79(8):085111, 2009.

[81] Chenyu Li, Chun-Chieh Chang, Qingli Zhou, Cunlin Zhang, and Hou-Tong Chen. Resonance coupling and polarization conversion in terahertz metasurfaces with twisted split-ring resonator pairs. *Optics express*, 25(21):25842–25852, 2017.

[82] Hou-Tong Chen, Willie J Padilla, Joshua MO Zide, Seth R Bank, Arthur C Gossard, Antoinette J Taylor, and Richard D Averitt. Ultrafast optical switching of terahertz metamaterials fabricated on eras/gaas nanoisland superlattices. *Optics letters*, 32(12):1620–1622, 2007.

[83] SS Prabhu, SE Ralph, MR Melloch, and ES Harmon. Carrier dynamics of low-temperature-grown gaas observed via thz spectroscopy. *Applied physics letters*, 70(18):2419–2421, 1997.

[84] Hou-Tong Chen, John F O'Hara, Abul K Azad, Willie J Padilla, Richard D Averitt, and Antoinette J Taylor. Terahertz metamaterials. In *Ultrafast Phenomena in Semiconductors and Nanostructure Materials XIII*, volume 7214, page 721417. International Society for Optics and Photonics, 2009.

[85] Longqing Cong, Yogesh Kumar Srivastava, Huifang Zhang, Xueqian Zhang, Jiaguang Han, and Ranjan Singh. All-optical active thz metasurfaces for ultrafast polarization switching and dynamic beam splitting. *Light: Science & Applications*, 7(1):28, 2018.

[86] Wen Xiang Lim, Manukumara Manjappa, Yogesh Kumar Srivastava, Longqing Cong, Abhishek Kumar, Kevin F MacDonald, and Ranjan Singh. Ultrafast all-optical switching of germanium-based flexible metaphotonic devices. *Advanced Materials*, 30(9):1705331, 2018.

[87] Yogesh Kumar Srivastava, Apoorva Chaturvedi, Manukumara Manjappa, Abhishek Kumar, Govind Dayal, Christian Kloc, and Ranjan Singh. Mos2 for ultrafast all-optical switching and modulation of thz fano metaphotonic devices. *Advanced Optical Materials*, 5(23):1700762, 2017.

[88] Germany. Darmstadt. Cst microw wave studio (cst).

[89] D Grischkowsky, Søren Keiding, Martin Van Exter, and Ch Fattinger. Far-infrared time-domain spectroscopy with terahertz beams of dielectrics and semiconductors. *JOSA B*, 7(10):2006–2015, 1990.

[90] John F O'Hara, Evgenya Smirnova, Abul K Azad, Hou-Tong Chen, and Antoinette J Taylor. Effects of microstructure variations on macroscopic terahertz metafilm properties. *Active and Passive Electronic Components*, 2007, 2007.

[91] Dibakar Roy Chowdhury, John F O'Hara, Antoinette J Taylor, and Abul K Azad. Orthogonally twisted planar concentric split ring resonators towards strong near field coupled terahertz metamaterials. *Applied Physics Letters*, 104(10):101105, 2014.

[92] Abul K Azad, Antoinette J Taylor, Evgenya Smirnova, and John F O'Hara. Characterization and analysis of terahertz metamaterials based on rectangular split-ring resonators. *Applied Physics Letters*, 92(1):011119, 2008.

[93] David M Pozar. *Microwave engineering; 3rd ed.* Wiley, Hoboken, NJ, 2005. URL `https://cds.cern.ch/record/882338`.

[94] Dibakar Roy Chowdhury, Ranjan Singh, Antoinette J Taylor, Hou-Tong Chen, Weili Zhang, and Abul K Azad. Coupling schemes in terahertz planar metamaterials. *International Journal of Optics*, 2012, 2012.

[95] Dibakar Roy Chowdhury, Abul K Azad, Weili Zhang, and Ranjan Singh. Near field coupling in passive and active terahertz metamaterial devices. *IEEE Transactions on Terahertz Science and*

Technology, 3(6):783–790, 2013.

[96] Shuang Zhang, Dentcho A Genov, Yuan Wang, Ming Liu, and Xiang Zhang. Plasmon-induced transparency in metamaterials. *Physical review letters*, 101(4):047401, 2008.

[97] Longqing Cong, Yogesh Kumar Srivastava, and Ranjan Singh. Inter and intra-metamolecular interaction enabled broadband high-efficiency polarization control in metasurfaces. *Applied Physics Letters*, 108(1):011110, 2016.

[98] Longqing Cong, Yogesh Kumar Srivastava, and Ranjan Singh. Near-field inductive coupling induced polarization control in metasurfaces. *Advanced Optical Materials*, 4(6):848–852, 2016.

[99] Xiaojun Liu, Jianqiang Gu, Ranjan Singh, Yingfang Ma, Jun Zhu, Zhen Tian, Mingxia He, Jiaguang Han, and Weili Zhang. Electromagnetically induced transparency in terahertz plasmonic metamaterials via dual excitation pathways of the dark mode. *Applied Physics Letters*, 100(13):131101, 2012.

[100] Wei Cao, Ranjan Singh, Caihong Zhang, Jiaguang Han, Masayoshi Tonouchi, and Weili Zhang. Plasmon-induced transparency in metamaterials: Active near field coupling between bright superconducting and dark metallic mode resonators. *Applied Physics Letters*, 103(10):101106, 2013.

[101] Na Liu, Hui Liu, Shining Zhu, and Harald Giessen. Stereometamaterials. *Nature Photonics*, 3(3): 157, 2009.

[102] Ilya V Shadrivov, David A Powell, Steven K Morrison, Yuri S Kivshar, and Gregory N Milford. Scattering of electromagnetic waves in metamaterial superlattices. *Applied Physics Letters*, 90(20): 201919, 2007.

[103] Mikhail Lapine, David Powell, Maxim Gorkunov, Ilya Shadrivov, Ricardo Marqués, and Yuri Kivshar. Structural tunability in metamaterials. *Applied Physics Letters*, 95(8):084105, 2009.

[104] David A Powell, Mikhail Lapine, Maxim V Gorkunov, Ilya V Shadrivov, and Yuri S Kivshar. Metamaterial tuning by manipulation of near-field interaction. *Physical Review B*, 82(15):155128, 2010.

[105] E Ekmekci, AC Strikwerda, K Fan, G Keiser, X Zhang, G Turhan-Sayan, and RD Averitt. Frequency tunable terahertz metamaterials using broadside coupled split-ring resonators. *Physical Review B*, 83(19):193103, 2011.

[106] Emil Prodan, Corey Radloff, Naomi J Halas, and Peter Nordlander. A hybridization model for the plasmon response of complex nanostructures. *science*, 302(5644):419–422, 2003.

[107] Shengyan Yang, Chengchun Tang, Zhe Liu, Bo Wang, Chun Wang, Junjie Li, Li Wang, and Changzhi Gu. Simultaneous excitation of extremely high-q-factor trapped and octupolar modes in terahertz metamaterials. *Optics express*, 25(14):15938–15946, 2017.

[108] Ranjan Singh, Wei Cao, Ibraheem Al-Naib, Longqing Cong, Withawat Withayachumnankul, and Weili Zhang. Ultrasensitive terahertz sensing with high-q fano resonances in metasurfaces. *Applied Physics Letters*, 105(17):171101, 2014.

[109] Jianqiang Gu, Ranjan Singh, Xiaojun Liu, Xueqian Zhang, Yingfang Ma, Shuang Zhang, Stefan A Maier, Zhen Tian, Abul K Azad, Hou-Tong Chen, et al. Active control of electromagnetically induced transparency analogue in terahertz metamaterials. *Nature communications*, 3:1151, 2012.

[110] MB Ketchen, D Grischkowsky, TC Chen, C-C Chi, IN Duling Iii, NJ Halas, J-M Halbout, JA Kash, and GP Li. Generation of subpicosecond electrical pulses on coplanar transmission lines. *Applied*

Physics Letters, 48(12):751–753, 1986.

[111] RD Averitt and AJ Taylor. Ultrafast optical and far-infrared quasiparticle dynamics in correlated electron materials. *Journal of Physics: Condensed Matter*, 14(50):R1357, 2002.

[112] FE Doany, D Grischkowsky, and C-C Chi. Carrier lifetime versus ion-implantation dose in silicon on sapphire. *Applied Physics Letters*, 50(8):460–462, 1987.

[113] Laura R Vanderhoef, Abul K Azad, Cory C Bomberger, Dibakar Roy Chowdhury, D Bruce Chase, Antoinette J Taylor, Joshua MO Zide, and Matthew F Doty. Charge carrier relaxation processes in tbas nanoinclusions in gaas measured by optical-pump thz-probe transient absorption spectroscopy. *Physical Review B*, 89(4):045418, 2014.

[114] PR Smith, DH Auston, AM Johnson, and WM Augustyniak. Picosecond photoconductivity in radiation-damaged silicon-on-sapphire films. *Applied Physics Letters*, 38(1):47–50, 1981.

[115] Stuart D Brorson, Jucheng Zhang, and So/ren R Keiding. Ultrafast carrier trapping and slow recombination in ion-bombarded silicon on sapphire measured via thz spectroscopy. *Applied physics letters*, 64(18):2385–2387, 1994.

[116] JEFFREY Bokor and NJ Halas. Time-resolved study of silicon surface recombination. *IEEE Journal of Quantum Electronics*, 25(12):2550–2555, 1989.

[117] Arash Elhami Khorasani, Dieter K Schroder, and TL Alford. Carrier recombination lifetime measurement in silicon epitaxial layers using optically excited mos capacitor technique. *IEEE Transactions on Electron Devices*, 62(5):1553–1560, 2015.

[118] Dibakar Roy Chowdhury, Ningning Xu, Weili Zhang, and Ranjan Singh. Resonance tuning due to coulomb interaction in strong near-field coupled metamaterials. *Journal of Applied Physics*, 118(2): 023104, 2015.

[119] Ranjan Singh, Jie Xiong, Abul K Azad, Hao Yang, Stuart A Trugman, QX Jia, Antoinette J Taylor, and Hou-Tong Chen. Optical tuning and ultrafast dynamics of high-temperature superconducting terahertz metamaterials. *Nanophotonics*, 1(1):117–123, 2012.

[120] Prakash Pitchappa, Manukumara Manjappa, Chong Pei Ho, Ranjan Singh, Navab Singh, and Chengkuo Lee. Active control of electromagnetically induced transparency analog in terahertz mems metamaterial. *Advanced Optical Materials*, 4(4):541–547, 2016.

[121] Yingfang Ma, Zhongyang Li, Yuanmu Yang, Ran Huang, Ranjan Singh, Shuang Zhang, Jianqiang Gu, Zhen Tian, Jiaguang Han, and Weili Zhang. Plasmon-induced transparency in twisted fano terahertz metamaterials. *Optical Materials Express*, 1(3):391–399, 2011.

[122] Jiaming Hao, Yu Yuan, Lixin Ran, Tao Jiang, Jin Au Kong, CT Chan, and Lei Zhou. Manipulating electromagnetic wave polarizations by anisotropic metamaterials. *Physical review letters*, 99(6): 063908, 2007.

[123] M Born and EMIL Wolf. Basic properties of the electromagnetic field. *Principles of optics*, 44, 1980.

[124] Jianchen Zi, Quan Xu, Qiu Wang, Chunxiu Tian, Yanfeng Li, Xixiang Zhang, Jiaguang Han, and Weili Zhang. Antireflection-assisted all-dielectric terahertz metamaterial polarization converter. *Applied Physics Letters*, 113(10):101104, 2018.

[125] Nathaniel K Grady, Jane E Heyes, Dibakar Roy Chowdhury, Yong Zeng, Matthew T Reiten, Abul K Azad, Antoinette J Taylor, Diego AR Dalvit, and Hou-Tong Chen. Terahertz metamaterials for linear

polarization conversion and anomalous refraction. *Science*, 340(6138):1304–1307, 2013.

[126] AN Grigorenko, Marco Polini, and KS Novoselov. Graphene plasmonics. *Nature photonics*, 6(11): 749, 2012.

[127] Long Ju, Baisong Geng, Jason Horng, Caglar Girit, Michael Martin, Zhao Hao, Hans A Bechtel, Xiaogan Liang, Alex Zettl, Y Ron Shen, et al. Graphene plasmonics for tunable terahertz metamaterials. *Nature nanotechnology*, 6(10):630, 2011.

[128] John F O'Hara, Ranjan Singh, Igal Brener, Evgenya Smirnova, Jiaguang Han, Antoinette J Taylor, and Weili Zhang. Thin-film sensing with planar terahertz metamaterials: sensitivity and limitations. *Optics Express*, 16(3):1786–1795, 2008.

[129] Ibraheem A Ibraheem Al-Naib, Christian Jansen, and Martin Koch. Thin-film sensing with planar asymmetric metamaterial resonators. *Applied Physics Letters*, 93(8):083507, 2008.

[130] Robert W Boyd, Daniel J Gauthier, and Alexander L Gaeta. Applications of slow light in telecommunications. *Optics and Photonics News*, 17(4):18–23, 2006.

[131] Daniel J Gauthier, Alexander L Gaeta, and Robert W Boyd. Slow light: from basics to future prospects. *Photonics Spectra*, 40(3):44, 2006.

[132] Manukumara Manjappa, Sher-Yi Chiam, Longqing Cong, Andrew A Bettiol, Weili Zhang, and Ranjan Singh. Tailoring the slow light behavior in terahertz metasurfaces. *Applied Physics Letters*, 106(18):181101, 2015.

[133] Qiang Bai, Cong Liu, Jing Chen, Chen Cheng, Ming Kang, and Hui-Tian Wang. Tunable slow light in semiconductor metamaterial in a broad terahertz regime. *Journal of Applied Physics*, 107(9): 093104, 2010.

[134] Sergei Tretyakov. On geometrical scaling of split-ring and double-bar resonators at optical frequencies. *Metamaterials*, 1(1):40–43, 2007.

CONFERENCES/SCHOOLS ATTENDED

1. **Attended**, DST-SERB school on Modern Optics and Its Applications, Dec. 01st -20th, 2015. IIT Patna, India.

2. **Poster presentation**, International Conference on Fiber Optics and Photonics – PHOTONICS, Dec. 04-08, 2016. IIT Kanpur, India. Topic: Modulating the Fundamental Resonances in Near Field Coupled Planar Terahertz Metamaterials.

3. **Oral presentation**, International Conference on Advances in Optics and Photonics (XLI Conference of Optical Society of India), November 23rd -26th , 2017, Guru Jambheshwar University of Science and Technology Hisar, Haryana (India). Topic: Exploring the near field inductive coupling in broadside coupled terahertz metamaterials.

4. **Poster presentation**, IEEE WRAP-2017, Dec. 18-19, 2017, MEC Hyderabad, India. Topic:Studying the near field capacitive coupling in planar terahertz metamaterial).

5. **Oral presentation**, SPIE Photonic West, Moscone Center, San Francisco, California, United States, 27th January – 1st February, 2019. Topic: Tuning near field capacitive coupling in planar terahertz metamaterials.

6. **Oral presentation**, SPIE Photonic West, Moscone Center, San Francisco, California, United States, 27th January – 1st February, 2019. Topic: Single split gap resonator based terahertz metamaterials for refractive index sensing.

7. **Poster presentation**, Research Conclave, held annually at IIT Guwahati, during the years 2017 and 2018. Topic: Exploring the near field coupling in THz metamaterials.

8. **Oral presentation**, XLII annual meeting of the optical society of India OSI - International Symposium on Optics (OSI-ISO 2018), 19 - 22 September, 2018. Indian institute of technology Kanpur. Topic: Ultrafast Switching in Single Resonator Based THz Metamaterials.

9. **Poster presentation**, Global Nanophotonics, 9 -12 December 2018. TIFR, India. Topic: Ultrafast Relaxation of Charge Carriers Induced Switching in Terahertz Metamaterials.

BIODATA

Education

2014 - present	Ph.D in Physics, IIT Guwahati, Guwahati.
2010 - 2012	M.Sc in Physics, Osmania University, Hyderabad.
	Percentage: 73.4%
2007 - 2010	B.Sc in Science, SR&BGNR Govt. College, Khammam.
	Percentage: 68.6%
2005 - 2007	11th and 12th classes, Govt. Junior College, Madhira.
	Percentage: 69.4%
2004 - 2005	10th class, ZPS School,Dendukur, Madhira.
	Percentage: 79.8%

Teaching involvement

Teaching assistant for General Physics, Advanced Physics, and Analog electronics laboratories for B.Tech and M.Sc. students in IIT Guwahati. (2015-2018)

Assisted B. Tech. and M. Sc. students at various level of their major, minor and summer projects. IIT Guwahati. (2015-2018).

Professional Memberships

Student member of OSA, SPIE, IEEE, and OSI.

Personal details

The author was born on June 1, 1990 at Doddadevarapadu village of Krishna district (Andhra Pradesh) in India.